POLITECNICO
MILANO 1863

SCUOLA DI INGEGNERIA INDUSTRIALE
E DELL'INFORMAZIONE

DLPF-MILP Based Optimal Reactive Power Flow and Voltage Control for Transmission Networks Applications

Tesi di Laurea Magistrale in
Electrical Engineering - Ingegneria Elettrica

Author: **Wanshan WU**

Student ID: 10855681
Advisor: Prof. Valentin Ilea
Co-advisors: Riccardo Nebuloni
Academic Year: 2024-2025

Abstract

With the rapid integration of renewable energy sources in large-scale power systems, system operational characteristics have changed significantly, creating substantial challenges for voltage stability and reactive power management. Although the conventional AC Optimal Reactive Power Flow (AC ORPF) method can accurately represent system behavior, its non-linearity and non-convexity result in extremely high computational complexity, and its solution efficiency is often insufficient for real-time operation and dispatch. In particular, when discrete control devices such as shunt capacitor banks and reactors are considered for voltage regulation, binary variables are introduced to represent their switching states which transforms the problem into a large scale Mixed-Integer Nonlinear Programming (MINLP) model. This increases computational complexity and makes it harder to obtain feasible solutions within a reasonable time. This study employs a Decoupled Linearized Power Flow-based Mixed-Integer Linear Programming model (DLPF-MILP) method to address reactive power optimization and voltage control problems. By decoupling and linearizing the power flow equations, the approach significantly reduces computational complexity while maintaining adequate accuracy. Based on this model, a voltage optimization framework is developed, incorporating various approximation and linearization techniques to achieve fast and stable voltage regulation under component outages or operational disturbances. Simulation results demonstrate that the proposed method maintains high solution accuracy while significantly reducing computation time, providing an effective solution for voltage control under $N-1$ security constraints. It offers an efficient, reliable, and real-time applicable approach for voltage optimization and regulation in large scale power systems.

Keywords: Voltage linearization optimization model, Decoupled Linearized Power Flow (DLPF), Mixed-Integer Linear Programming(MILP), Voltage control, N-1 security constraints

Abstract in lingua italiana

Con l'integrazione rapida delle fonti di energia rinnovabile nei sistemi elettrici su larga scala, le caratteristiche operative del sistema sono cambiate significativamente, creando sfide importanti per la stabilità della tensione e la gestione della potenza reattiva. Sebbene il metodo convenzionale di Flusso di Potenza Ottimale in Corrente Alternata per la Potenza Reattiva (AC ORPF) possa rappresentare accuratamente il comportamento del sistema, la sua non linearità e non convessità comportano una complessità computazionale elevata, e l'efficienza della soluzione è spesso insufficiente per operazioni e dispatch in tempo reale. In particolare, quando si considerano dispositivi di controllo discreti come banche di condensatori shunt e reattori per la regolazione della tensione, si introducono variabili binarie per rappresentarne gli stati di commutazione, trasformando il problema in un modello di Programmazione Non Lineare Mista Intera (MINLP) su larga scala. Questo aumenta la complessità computazionale e rende più difficile ottenere soluzioni fattibili entro tempi ragionevoli. Questo studio impiega un modello basato su Flusso di Potenza Linearizzato e Decoupled combinato con Programmazione Lineare Mista Intera (DLPF-MILP) per affrontare problemi di ottimizzazione della potenza reattiva e controllo della tensione. Attraverso il decoupling e la linearizzazione delle equazioni di flusso di potenza, l'approccio riduce significativamente la complessità computazionale mantenendo adeguata accuratezza. Basandosi su questo modello, viene sviluppato un framework di ottimizzazione della tensione che incorpora varie tecniche di approssimazione e linearizzazione per ottenere una regolazione rapida e stabile in caso di guasti ai componenti o disturbi operativi. I risultati delle simulazioni dimostrano che il metodo proposto mantiene elevata accuratezza della soluzione riducendo significativamente il tempo di calcolo, fornendo una soluzione efficace per il controllo della tensione sotto i vincoli di sicurezza $N-1$. Offre un approccio efficiente, affidabile e applicabile in tempo reale per l'ottimizzazione e la regolazione della tensione nei sistemi elettrici su larga scala.

Parole chiave: Modello di ottimizzazione linearizzata della tensione, Flusso di potenza linearizzato disaccoppiato (DLPF), Programmazione lineare intera mista (MILP), Controllo della tensione, Vincoli di sicurezza N-1

Contents

Introduction

In recent years, multiple large scale blackouts have demonstrated that insufficient voltage regulation is a severe threat to the secure operation of power systems. For example, the 2003 North American blackout and the 2012 Indian grid collapse were both triggered by failures related to inadequate voltage and load control [1] [2]. The 2003 Italian blackout was initiated by overloads on interconnected transmission lines, resulting in significant power imbalances and voltage instability. The system's insufficient reactive power compensation and lack of coordinated voltage control led to a rapid voltage decline, which subsequently triggered cascading failures and widespread system separation [3]. A more typical case is the 2025 blackout in Spain and Portugal, which affected more than 60 million people. Investigations revealed that the root cause was a sudden voltage surge followed by a lack of effective dynamic voltage control, as the system operator and several power plants failed to provide the necessary absorption and support under high-voltage conditions, ultimately leading to system collapse. These events clearly illustrate that insufficient voltage stability can undermine the secure operation of power systems and may eventually result in voltage collapse or large scale blackouts.

At present, the energy transition is accelerating, progressing toward a sustainable electricity system dominated by renewable energy, with numerous countries committing to achieving this objective over the coming decades [4]. The ongoing energy transition is progressively substituting large-scale conventional coal and gas power plants with substantial amounts of distributed renewable energy sources (RES) within medium- and low-voltage (MV/LV) networks. With the large-scale integration of wind, photovoltaic, and other renewable energy sources, the traditional active/reactive power support paradigm dominated by thermal power units is gradually losing its effectiveness. In conventional power systems, thermal generators play a dominant role, and their strong active and reactive power support capabilities help maintain voltage stability, with grid operation primarily relying on centralized regulation and economic dispatch of active power. However, high levels of renewable energy penetration have altered this paradigm. On one hand, the output of renewable sources is variable and intermittent, causing frequent voltage fluctuations and increasing the risk of undervoltage, overvoltage, and voltage instability. On

the other hand, RES are often connected in a distributed manner to medium and low voltage networks, leading to highly localized and multi layered grid operations, which traditional centralized control methods cannot effectively manage. In addition, renewable energy sources are more sensitive to abnormal operating conditions than conventional generators and may disconnect during system disturbances, leading to a failure to supply the required active or reactive power, thereby further exacerbating grid instability [5].
This uncertainty may lead to extreme conditions in certain areas where reactive power is either severely insufficient or excessive, thereby putting pressure on voltage stability and the reliable operation of the system. As the energy transition progresses, reactive power reserves become highly unstable in both time and space, and their distribution and demand are difficult to predict, making voltage regulation not only more frequent but also more uncertain and complex, which places higher demands on reactive power optimization [6]. In the context of renewable energy, local voltage regulation, reactive power management, and system stability have thus become critical scientific and engineering challenges that must be addressed in the energy transition.
Voltage regulation and reactive power optimization have always been core problems in power system operation and dispatching. The security and stability of a power system depend not only on the economic dispatch of active power but also on the proper distribution of reactive power and the effective control of voltage levels. From the perspective of optimization modeling, the AC Optimal Power Flow (AC OPF) provides the basic framework for operational optimization. The reactive power optimization and voltage control problem, known as AC Optimal Reactive Power Flow (AC ORPF), can directly address issues of voltage stability and system security. The classical AC ORPF model can accurately capture the electrical characteristics of the grid and its voltage behavior [7]. However, this problem is inherently strongly nonlinear and nonconvex, leading to high computational complexity. In large-scale power systems, the solution efficiency often cannot meet practical operational requirements. The problem becomes significantly more complex when N-1 security constraints are imposed, requiring the system to remain secure and operational under the contingency of any single component, such as a transmission line, transformer, or generator [8]. In particular, when voltage regulation involves discrete control devices such as shunt capacitor banks and reactors, binary or integer variables must be introduced in the model to represent their switching states. This inclusion significantly increases the problem's complexity and size, as it transforms the optimization into a mixed-integer problem with combinatorial characteristics. In such cases, the problem size increases exponentially, further limiting the applicability of traditional AC ORPF methods.
To address this challenge, various improvement methods have been proposed. Some stud-

ies focus on numerical iterative and heuristic algorithms, such as genetic algorithms [9], and particle swarm optimization [10]. Although these methods can obtain feasible solutions to some extent, they often suffer from low computational efficiency or poor convergence. Another category is based on convex relaxation approaches, such as semidefinite programming (SDP) [11]and second-order cone programming (SOCP) [12]. These methods can achieve global or near-optimal solutions under certain conditions, but they are computationally intensive and difficult to scale to large systems or multiple contingency scenarios. More recently, distributed and decomposition-based methods [13] have shown some progress, partially alleviating scalability issues, though they still impose high requirements on model simplification and algorithm design.

Against this background, linearized power flow models have attracted significant attention. By appropriately linearizing the power flow equations, the computational complexity of optimization can be greatly reduced while maintaining a certain level of accuracy. Among these models, the conventional DC Power Flow is widely used due to its simplicity; however, it neglects voltage magnitudes and reactive power, making it unsuitable for voltage regulation problems [14]. To address this limitation, this study adopts the Decoupled Linearized Power Flow (DLPF) model. By linearizing the power flow relationships, the model transforms the nonlinear mapping between node voltages and power system states into a tractable linear problem. This approach retains the advantages of linearization while accounting for voltage magnitude regulation, providing a more accurate representation of the fundamental relationship between voltage and reactive power.

This study develops a voltage optimization and control model based on DLPF approach, incorporating N-1 security constraints to form a comprehensive voltage optimization and control framework. The proposed model explicitly considers linearized transformer models and linearized discrete control devices such as shunt elements, accurately reflecting their impact on voltage regulation. Simulation results on large-scale power systems demonstrate that the model offers excellent voltage regulation capability, rapid response performance, and high computational efficiency, effectively meeting the requirements of real-time operation.

The rest of the thesis is organized as follows:

- Chapter 1 presents various voltage regulation strategies, including theoretical foundations, practical applications, and key advantages and limitations.
- Chapter 2 introduces the theoretical foundation and computational characteristics of the linearized power flow method, providing methodological support for the development of the voltage optimization and control model.
- Chapter 3 demonstrates system modeling and simulation using the linearized power

flow approach, including the power flow calculation process and analysis of computational errors and efficiency.

- Chapter 1 presents various voltage regulation strategies, including theoretical foundations, practical applications, and key advantages and limitations.
- Chapter 4 develops a voltage optimization and control model, including linearized modeling of key components, objective function, and constraints.
- Chapter 5 Validate the proposed model through case studies and fault scenarios, demonstrating voltage regulation performance and applicability.
- Chapter 6 Assesses the feasibility, accuracy, and computational efficiency of the linearized optimization model by comparing its results with full AC power flow calculations, verifying the model's capability to represent real system behavior while significantly reducing computation time.
- Chapter 7 Summarizes the overall research, highlights key contributions and limitations, and discusses potential future work directions.

1 | Voltage Regulation Methods in Power System

The stability and regulation of voltage in power systems are fundamental to secure, reliable, and efficient operation. Voltage regulation maintains voltage levels within specified limits to prevent voltage collapse, equipment damage, and outages caused by changes in load, generation, and network conditions.

1.1. Voltage Stability and Control Objectives

Voltage stability, as defined by the IEEE/CIGRE task force [15], is the capability of a power system to sustain steady voltages at all buses following a disturbance from a given initial operating condition. Extensive research and operational experience have shown that voltage levels directly affect power transfer capability, network losses, and the lifetime of electrical equipment. For instance, undervoltage can result in increased motor current, reduced efficiency, and even loss of synchronism, while overvoltage may cause insulation breakdown and premature aging of components. More critically, under high loading conditions or insufficient reactive power support, voltage deviations may trigger voltage collapse, potentially leading to large-scale blackouts. Therefore, voltage regulation and reactive power management have become key topics in system operation and dispatch.
The primary objectives of voltage control are:

- to maintain bus voltages within an allowable range;
- to adjust reactive power distribution in order to reduce network losses and enhance transmission capacity;
- to prevent voltage instability or collapse.

With the continuous expansion of modern power systems and the increasing complexity of load structures, the challenges of voltage regulation have become more severe. Dy-

namic load changes, the integration of distributed generation, faults in transmission lines, and the uncertainty of renewable energy generation can cause voltage fluctuations. Consequently, precise and flexible control of both voltage and reactive power is required to maintain voltages within acceptable limits, thus preventing adverse impacts on equipment and power quality due to voltage sags or surges. To achieve effective voltage control, multiple voltage regulation methods are typically used in combination. These methods include adjusting substation bus voltages via transformers to control voltage, rapidly modulating local reactive power with shunt compensation devices to improve voltage response and stability, and tuning generator reactive power to coordinate voltages between generation and load nodes.

The following sections provide a detailed discussion of three typical voltage regulation methods: generator reactive power control, shunt reactive power compensation, and transformer voltage adjustment.

1.2. Generator Reactive Power Control

Reactive power control of synchronous generators is a key mechanism for maintaining voltage stability and ensuring reliable operation of power systems. By adjusting the generator excitation, operators can regulate the reactive power output to satisfy local voltage requirements or provide support under varying load conditions. This approach contributes to minimizing voltage deviations, reducing transmission losses, and preventing overloading of transmission lines. In practical applications, generator reactive power control is typically implemented via an Automatic Voltage Regulator (AVR), which continuously monitors the generator terminal voltage and modulates the excitation accordingly. To optimize overall system performance and prevent adverse interactions, it is essential to coordinate generator operation with other voltage regulation devices, including shunt capacitors and tap-changing transformers. In addition, the ability of generators to adjust reactive power is limited by the unit's capacity, excitation system constraints, and stability requirements. Therefore, effective reactive power control requires a comprehensive consideration of generator characteristics, system requirements, and operational constraints to achieve both reliable and economically efficient voltage regulation.

1.3. Shunt Reactive Power Compensation

Shunt reactive power elements are commonly used in power systems for voltage control and reactive power regulation, improving bus voltage profiles and enhancing system stability and reliability. Common devices include shunt capacitor banks, shunt reactors, and

synchronous condensers.

1.3.1. Traditional Shunt Elements

Traditional shunt reactive power devices primarily include shunt capacitor banks and shunt reactors.

Shunt capacitor banks inject reactive power into the system, which can be expressed as

$$Q = +BV^2 \tag{1.1}$$

where B is the susceptance and V is the bus voltage magnitude. Under high load conditions, injecting reactive power can effectively raise local bus voltages, mitigating voltage drops and supporting power factor improvement and power flow optimization. In contrast, shunt reactors absorb reactive power, with the reactive power output given by

$$Q = -BV^2 \tag{1.2}$$

By absorbing excess reactive power, shunt reactors contribute to the reduction of bus voltage levels, particularly under light-load or high-generation conditions. This reactive power control mitigates the risk of overvoltage and enhances the operational efficiency of system equipment by minimizing unnecessary losses. Taken together, these traditional shunt elements constitute a fundamental and cost-effective mechanism for reliable voltage regulation within power systems.
Traditional shunt elements, including capacitor banks and reactors, are simple to operate and cost-effective, offering significant and reliable contributions to voltage regulation. Their main advantage lies in their ability to inject or absorb reactive power at local buses, thereby maintaining bus voltages within acceptable limits under varying load or generation conditions. However, due to their relatively fixed control mode, these devices often need to be coordinated with other voltage control measures to ensure the overall stability of the power system.

1.3.2. Controllable Shunt Elements

With the development of Flexible AC Transmission Systems (FACTS), more advanced controllable shunt devices have been introduced [16]. Static VAR Compensators (SVCs), which comprise thyristor-controlled reactors (TCR) and thyristor-switched capacitors (TSC), allow dynamic adjustment of reactive power in response to system requirements.

Similarly, Static Synchronous Compensators (STATCOMs), based on voltage-source converters (VSC), provide faster response and a wider operating range compared to conventional devices, effectively stabilizing bus voltages under rapidly changing operating conditions.

1.3.3. Role in Voltage Regulation

Proper deployment of shunt elements can help system operators maintain bus voltages within allowable limits, ensuring the safe and reliable operation of various loads. In addition, these elements contribute to improving voltage profiles across the network and enhancing the overall efficiency and stability of the power system. By providing low-cost and stable reactive power support, shunt elements form a fundamental mechanism for voltage regulation and reactive power management in both transmission and distribution networks.

In practical power system operation and optimization studies, traditional shunt elements play a critical role.Their main advantages are low cost, simplicity, and reliability. Although controllable reactive power devices such as Static Var Compensators (SVCs) and Static Synchronous Compensators (STATCOMs) offer faster and more flexible voltage support, the present study emphasizes the strategic optimization of traditional shunt elements. This includes the systematic design of their placement and capacity, as well as the implementation of appropriate switching strategies. These measures aim to enhance voltage profiles, improve reactive power management, and strengthen the operational reliability of both transmission and distribution networks.

1.4. Transformer Voltage Adjustment

Transformers are key components of the power grid and play a central role in controlling bus voltages. Various transformer-based voltage regulation techniques exist and adjusting the operating conditions of transformers can effectively control bus voltages while remaining simple and economical.

1.4.1. Tap Ratio Regulation

Tap ratio regulation is a method of controlling bus voltage magnitude by changing the transformer turns ratio, primarily used to maintain node voltages within allowable limits. The relationship between the secondary voltage of the transformer and the primary voltage and tap ratio can be expressed as:

$$V_{\text{secondary}} = t \cdot V_{\text{primary}} \tag{1.3}$$

where $V_{\text{secondary}}$ is the secondary bus voltage, V_{primary} is the primary bus voltage, and t is the tap ratio determined by the tap position. By adjusting the tap ratio t, the secondary voltage magnitude can be effectively controlled, achieving bus voltage regulation. Tap ratio regulation primarily affects voltage magnitude rather than phase angle and can be operated mechanically or electrically. It is suitable for long-term or mid-term voltage control, with significant impact on neighboring buses, but limited effect on distant buses.

1.4.2. Tap Staggering

Tap Staggering is a novel voltage and reactive power control strategy. The key principle is to exploit tap differences among parallel transformers to absorb reactive power, thereby mitigating overvoltage issues in the grid. In contrast to conventional methods that depend on shunt elements or static var compensators, Tap Staggering does not require additional equipment investment. Instead, it utilizes existing on-load tap-changing transformers, where staggered tap positions generate circulating currents between parallel units that absorb reactive power from the network and support voltage regulation [17]. The construction of two parallel transformers with staggered taps in Figure 1.1 is demonstrated.

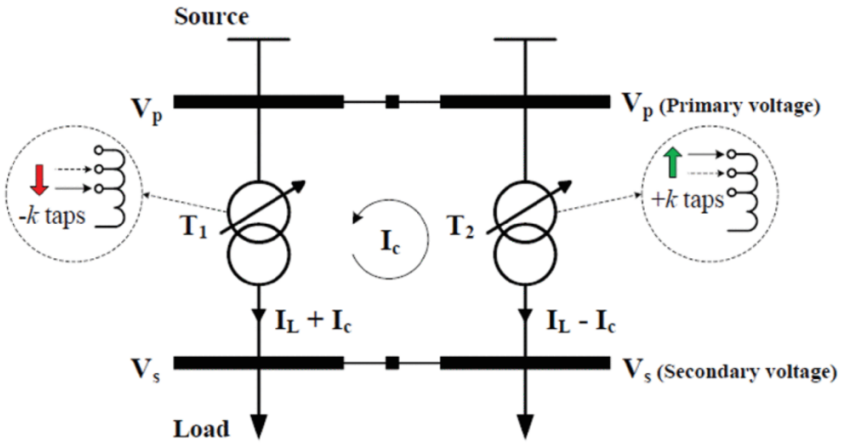

Figure 1.1: Construction of Parallel Transformers Using Tap Staggering [18].

The fundamental concept of Tap Staggering is to treat parallel transformers as an integrated system and implement staggered tap operations to regulate voltage and reactive power. Specifically, consider two parallel transformers, T1 and T2, whose on-load tap changers (OLTCs) are initially set to the same tap position. In a Tap Staggering oper-

ation, the tap position of T1 is decreased by k steps, while that of T2 is increased by k steps, forming a staggered tap pattern. Due to the tap differences, circulating currents I_c are generated between the transformers. These circulating currents flow through the transformers' leakage reactances and consume reactive power [19]. From the perspective of the upstream network, this process effectively absorbs excess reactive power, thereby achieving effective bus voltage regulation. Consequently, Tap Staggering can mitigate overvoltage issues during low-load or high renewable generation periods without the need for additional shunt reactors or reactive power compensation devices.

1.4.3. Phase Shifter Control

Phase Shifter Transformer introduces a controllable phase shift between its primary and secondary sides to regulate branch power flow, thereby enabling line power redistribution and load optimization. The related derivations can be referred to Section 2.2.3. Unlike tap ratio regulation, PST has limited direct impact on voltage magnitude but can indirectly influence bus voltages and reactive power distribution. By altering the direction of active power flow, PST adjusts the voltage profile along the line and induces local changes in reactive power, thereby contributing to voltage and reactive power balance in the system. With its fast response, PST is suitable for addressing short-term load fluctuations and transmission congestion. In modern power systems, PST is typically used in conjunction with tap ratio regulation and reactive power compensation devices, enabling coordinated control of both active power flow and reactive power support for bus voltages, thus enhancing system stability and operational flexibility.

1.5. Voltage Regulation Strategies and Comparative Control Performance

Voltage regulation is a critical measure for ensuring the safe and stable operation of power systems. With the rapid development of large-scale power systems and the increasing penetration of renewable energy sources, voltage fluctuations and rapid load variations place higher demands on system stability. Therefore, evaluating the performance of various voltage regulation methods under real-time operation provides theoretical support and engineering guidance for system optimization and control. The specific characteristics and performance of these methods are summarized in Table 1.1 below.

Regulation Method	Response Speed	Applicable Scenario	Limitations
Generator Qg Control	Medium-fast	Dynamic system-wide voltage coordination	Constrained by generator reactive power capability; high operational cost; requires coordination with other devices
Shunt Element	Fast	Rapid voltage support during load or generation fluctuations	Limited regulation range; overall effectiveness depends on layout and capacity
Tap Ratio	Medium	System-wide voltage adjustment	Limited continuous adjustment capability; difficult to handle rapid load fluctuations [20]
Tap Straggling	Medium	Voltage control of local nodes and substations	Discrete step operation; frequent use may cause mechanical wear
Phase Shifter	Medium	Power flow control and coordinated flow optimization	Limited direct impact on node voltage; cannot independently regulate system voltage

Table 1.1: Voltage Regulation Methods and Control Characteristics

2 | Decoupled Linearized Power Flow Method

This chapter first provides a brief introduction to common power flow analysis methods, including the AC Power Flow (ACPF) and DC Power Flow (DCPF) along with their modeling characteristics. Subsequently, based on the ACPF equations, the Decoupled Linearized Power Flow (DLPF) model is derived, including the expressions for bus voltage magnitudes, phase angles, and branch active power flows, followed by a step-by-step implementation procedure of the model.

2.1. Common Power Flow Methods

ACPF is the fundamental method for power flow analysis in power systems. This model captures the system's operating conditions by formulating nonlinear coupling equations among bus voltage magnitudes, phase angles, and active and reactive power. It is widely used in steady-state analysis, voltage control, reactive-power optimization, and voltage-stability studies.

The power flow problem involves solving a set of nonlinear equations. The Newton-Raphson solution method is a recursive iterative method that solves the power flow equations until the active and reactive mismatch tolerance is met. This mismatch tolerance is the stopping criterion and signifies that the solution has converged [21].

$$S_i = V_i \sum_j Y_{ij}^* V_j^* \tag{2.1}$$

The ACPF problem is formulated via the nodal complex-power injection balance and solved as a system of nonlinear equations. In practice, the Newton–Raphson method iteratively updates bus voltage magnitudes and phase angles until both real and reactive power mismatches fall below a specified convergence tolerance. Despite its high accuracy, the nonlinear characteristics, convergence challenges, and relatively low computational efficiency of these methods constrain their application in the power-systems industry,

particularly for large-scale systems [22].
The DCPF model is a linearization approach widely used in power-system analysis and optimization. Due to its linear, non-iterative model and reasonable accuracy in active power flow calculation, it has considerable analytical and computational appeal compared with the ACPF model [23]. The DCPF model employs three key linearizing assumptions: bus voltage magnitudes are fixed at 1.0 p.u.; line resistances and reactive power flows are neglected; and the small angle approximation $\sin(\delta_i - \delta_j) \approx \delta_i - \delta_j$. This reduces the full ACPF problem to a single sparse linear system. Under these assumptions the real power flow on branch $i-j$ reduces to

$$\begin{aligned} P_{ij} &= -\, b_{ij}\,(\theta_i - \theta_j), \\ b_{ij} &= \frac{1}{x_{ij}}\,, \end{aligned} \tag{2.2}$$

The resulting linear system is trivial to solve and extremely fast, but it does not capture variations in bus voltage magnitudes or reactive-power distribution, limiting its accuracy and making it unsuitable for voltage sensitive analyses [24].

Therefore, this study adopts DLPF model—a compromise approach built upon the DCPF that further accounts for bus voltage magnitudes and reactive-power effects through linearization and decoupling techniques. Compared to the conventional DCPF model, DLPF model delivers similar active power accuracy while more accurately representing voltage magnitude variations. It also requires only the solution of a linear system, it significantly lowers computational complexity and making it well suited for large-scale networks or batch power flow simulations [25].

2.2. Formulation and Derivation of the DLPF

The DLPF model linearizes and decouples the nonlinear coupling terms between bus voltage magnitudes V and voltage angles θ in the ACPF equations. By separately evaluating the influence of active power on phase angles and of reactive power on voltage magnitudes, it converts the original coupled nonlinear problem into two sparse linear subproblems. The DLPF model was originally introduced in [25], which provides the foundation for the formulation and derivation presented in following section.

2.2.1. Decoupling of Voltage Magnitude and Phase Angle

The power flow equations are used to describe the relationship between the voltage at each node and the power in the electrical grid, typically using Kirchhoff's current law and voltage law. The voltage–power formulation of the polar AC power flow equations for an n-bus network is a classic and widely adopted approach in power system analysis. The specific equations are as follows:

$$\begin{cases} P_i = \sum_{j=1}^{n} V_i V_j \left(G_{ij} \cos\theta_{ij} + B_{ij} \sin\theta_{ij} \right), \\ Q_i = \sum_{j=1}^{n} V_i V_j \left(-B_{ij} \cos\theta_{ij} + G_{ij} \sin\theta_{ij} \right) \end{cases} \tag{2.3}$$

where:

- $i = 1, 2, \ldots, n$ is the bus index;
- P_i, Q_i are the active and reactive power injections at bus i;
- V_i, V_j are the voltage magnitudes at buses i and j, in per unit (p.u.);
- $\theta_{ij} = \theta_i - \theta_j$ is the voltage angle difference between buses i and j;
- G_{ij}, B_{ij} are the real and imaginary parts of the bus admittance matrix Y_{bus}, representing conductance and susceptance, respectively.

Moreover, the power system admittance matrix is characterized by a special structure, in which the diagonal elements are the sum of the off-diagonal elements in the corresponding rows, including the contributions from shunt elements.

$$Y_{ij} = \begin{cases} -y_{ij} & \text{if } j \neq i \\ y_{ii} + \sum_{\substack{k=1 \\ k \neq i}}^{n} y_{ik} & \text{if } j = i \end{cases} \tag{2.4}$$

where:

- y_{ij} is the admittance of the branch directly connecting bus i and bus j;
- y_{ii} is the shunt admittance at bus i;
- n is the total number of buses in the system;

- k is the index of buses connected to bus i, excluding i itself (i.e., $k \neq i$).

In this thesis, the diagonal "shunt" admittances y_{ii} include not only the effects of shunt capacitors but also the line-charging susceptance and the equivalent admittances of transformers and phase shifters.
For most practical power system scenarios, bus voltage magnitudes are close to 1 p.u., and the absolute values of phase angle differences across transmission lines rarely exceed 30° [26], with the majority falling within 10° [24]. Based on these empirical observations, it is reasonable to approximate the sine and cosine functions by their first-order Taylor expansions around zero, i.e., $\sin\theta \approx \theta$ and $\cos\theta \approx 1$. This approximation simplifies the trigonometric expressions in the power flow equations, thereby supporting the widely used linearized and simplified modeling approaches in power system analysis.
Based on these considerations, (2.3) is linearized using the following approximations to separate (decouple) voltage magnitudes from phase angles:

$$
\begin{aligned}
P_i =& \sum_{j=1}^{n} V_i V_j (G_{ij}\cos\theta_{ij} + B_{ij}\sin\theta_{ij}) \\
=& g_{ii}V_i^2 + \sum_{j=1, j\neq i}^{n} \left(g_{ij}V_i\left(V_i - V_j\cos\theta_{ij}\right) - b_{ij}V_iV_j\sin\theta_{ij}\right) \\
\approx& g_{ii}V_i + \sum_{j=1, j\neq i}^{n} g_{ij}\left(V_i - V_j\right) - \sum_{j=1, j\neq i}^{n} b_{ij}\left(\theta_i - \theta_j\right) \\
=& \left(V_i\sum_{j=1}^{n} g_{ij} + \sum_{j=1, j\neq i}^{n}\left(-g_{ij}\right)V_j\right) - \left(\theta_i\sum_{j=1, j\neq i}^{n} b_{ij} + \sum_{j=1, j\neq i}^{n}\left(-b_{ij}\right)\theta_j\right) \\
=& \sum_{j=1}^{n} G_{ij}V_j - \sum_{j=1}^{n} B'_{ij}\theta_j
\end{aligned}
\tag{2.5}
$$

$$
\begin{aligned}
Q_i &= \sum_{j=1}^{n} V_i V_j (-B_{ij} \cos\theta_{ij} + G_{ij} \sin\theta_{ij}) \\
&= -\left(b_{ii} V_i^2 + \sum_{j=1, j\neq i}^{n} \left(b_{ij} V_i \left(V_i - V_j \cos\theta_{ij}\right) + g_{ij} V_i V_j \sin\theta_{ij}\right)\right) \\
&\approx -\left(b_{ii} V_i + \sum_{j=1, j\neq i}^{n} b_{ij} \left(V_i - V_j\right) + \sum_{j=1, j\neq i}^{n} g_{ij} \left(\theta_i - \theta_j\right)\right) \\
&= -\left(V_i \sum_{j=1}^{n} b_{ij} + \sum_{j=1, j\neq i}^{n} \left(-b_{ij}\right) V_j\right) - \left(\theta_i \sum_{j=1, j\neq i}^{n} g_{ij} + \sum_{j=1, j\neq i}^{n} \left(-g_{ij}\right) \theta_j\right) \\
&= -\sum_{j=1}^{n} B_{ij} V_j - \sum_{j=1}^{n} G'_{ij} \theta_j
\end{aligned}
\tag{2.6}
$$

where:

- g_{ij} is the conductance of the branch between buses i and j;
- b_{ij} is the susceptance of the branch between buses i and j (typically accounting for line-charging and shunt capacitors).
- G'_{ij}, B'_{ij} are the real and imaginary parts of the bus admittance matrix Y'_{bus} without shunt elements, representing conductance and susceptance excluding shunt components, respectively.

In (2.6), it is assumed that $G'_{ij} \approx G_{ij}$, since shunt conductance is generally negligible relative to shunt susceptance.
The power flows on branch (i, j) are expressed as follows:

$$P_{ij} = g_{ij}\left(V_i^2 - V_i V_j \cos\theta_{ij}\right) - b_{ij} V_i V_j \sin\theta_{ij}, \tag{2.7}$$

$$Q_{ij} = -b_{ij}\left(V_i^2 - V_i V_j \cos\theta_{ij}\right) - g_{ij} V_i V_j \sin\theta_{ij}. \tag{2.8}$$

where:

- P_{ij}/Q_{ij} Active/reactive power flow from bus i to bus j.

A theoretical mechanism underlies the approximation method, as they follow the proposed approximation [25], in the expression of branch MW flow.

$$
\begin{aligned}
g_{ij}V_i\left(V_i - V_j\cos\theta_{ij}\right) &\approx g_{ij}V_i\left(V_i - V_j\right) \\
&= g_{ij}\left(1+\Delta V_i\right)\left(\Delta V_i - \Delta V_j\right) \\
&= g_{ij}\left(\Delta V_i - \Delta V_j + \Delta V_i^2 - \Delta V_i\Delta V_j\right) \\
&\approx g_{ij}\left(\Delta V_i - \Delta V_j\right) \\
&= g_{ij}\left(1+\Delta V_i - 1 - \Delta V_j\right) \\
&= g_{ij}\left(V_i - V_j\right)
\end{aligned}
\tag{2.9}
$$

Note that V_i is decomposed as $1+\Delta V_i$, with $|\Delta V_i| \ll 1$. In this formulation, the quadratic terms ΔV_i^2 and $\Delta V_i \Delta V_j$ are negligible compared to the linear terms in V_i and V_j, without leading to an appreciable loss of accuracy.
By applying the aforementioned approximation, the branch active/reactive power flow can be easily obtained from the equation (2.5) and (2.6) , yielding a linearized expression of the branch MW flow.

$$
\begin{aligned}
P_{ij}^A &= g_{ij}\left(V_i - V_j\right) - b_{ij}\left(\theta_i - \theta_j\right), \\
Q_{ij}^A &= -b_{ij}\left(V_i - V_j\right) - g_{ij}\left(\theta_i - \theta_j\right)
\end{aligned}
\tag{2.10}
$$

where:

- P_{ij}^A/Q_{ij}^A Linear approximation of active/reactive power flow.

In power flow modeling, multiple approximation methods are available for the decoupling process. Most of these methods rely on a common assumption, namely $\cos\theta_{ij} \approx 1$. These methods differ primarily in the approach of modeling voltage magnitudes. In the conventional DC power flow model, voltage differences across branches and the terms associated with ΔV are neglected. This simplification transforms the original coupled nonlinear magnitude–angle equations into linear equations that only involve phase angle differences.
In contrast, the approximation adopted in (2.9) accounts for voltage differences, which is a key step in the derivation of the DLPF model. As demonstrated in [25], under two typical operating conditions(a high R/X ratio and a low R/X ratio, approximation in (2.9) outperforms other linear power flow models in terms of branch MW power flow accuracy.

2.2.2. Matrix Formulation of the DLPF Model

Building on (2.5) and (2.6), the DLPF model can be compactly written in matrix form as follows:

$$\begin{bmatrix} \boldsymbol{P} \\ \boldsymbol{Q} \end{bmatrix} = - \begin{bmatrix} \boldsymbol{B'} & -\boldsymbol{G} \\ \boldsymbol{G} & \boldsymbol{B} \end{bmatrix} \begin{bmatrix} \boldsymbol{\theta} \\ \boldsymbol{V} \end{bmatrix} \tag{2.11}$$

where:

- $\boldsymbol{P}$ and $\boldsymbol{Q}$ are vectors of nodal active and reactive power injections, respectively;
- $\boldsymbol{\theta}$ is the vector of voltage phase angles (in radians);
- $\boldsymbol{V}$ is the vector of voltage magnitudes (in per unit);
- $\boldsymbol{G}$ and $\boldsymbol{B}$ are the real and imaginary parts of the admittance matrix, respectively;
- $\boldsymbol{B'}$ is the imaginary part of the admittance matrix excluding shunt elements.

Both $\boldsymbol{\theta}$ and $\boldsymbol{V}$ are partitioned into three subvectors—one for the $V\theta$ buses, one for the PV buses, and one for the PQ buses. For notational convenience, these groups are ordered as $V\theta$, PV, PQ.

$$\begin{aligned} \boldsymbol{\theta} &= \begin{bmatrix} \boldsymbol{\theta}_{\mathcal{R}}^T, & \boldsymbol{\theta}_{\mathcal{S}}^T, & \boldsymbol{\theta}_{\mathcal{L}}^T \end{bmatrix}^T \\ \boldsymbol{V} &= \begin{bmatrix} \boldsymbol{V}_{\mathcal{R}}^T, & \boldsymbol{V}_{\mathcal{S}}^T, & \boldsymbol{V}_{\mathcal{L}}^T \end{bmatrix}^T \end{aligned} \tag{2.12}$$

where:

- $\boldsymbol{\theta}_{\mathcal{R}}$ is the subvector of angles at reference (slack) buses;
- $\boldsymbol{\theta}_{\mathcal{S}}$ is the subvector of angles at PV buses;
- $\boldsymbol{\theta}_{\mathcal{L}}$ is the subvector of angles at PQ buses;
- $\boldsymbol{V}_{\mathcal{R}}$ is the subvector of voltage magnitudes at reference (slack) buses;
- $\boldsymbol{V}_{\mathcal{S}}$ is the subvector of voltage magnitudes at PV buses;
- $\boldsymbol{V}_{\mathcal{L}}$ is the subvector of voltage magnitudes at PQ buses;
- The superscript $\mathbf{T}$ denotes the transpose operation, which converts a row vector into a column vector or vice versa.

Similarly, the admittance matrix $\boldsymbol{Y}$ is divided into corresponding block submatrices as follows:

$$\boldsymbol{Y} = \begin{bmatrix} \boldsymbol{Y}_{\mathcal{RR}} & \boldsymbol{Y}_{\mathcal{RS}} & \boldsymbol{Y}_{\mathcal{RL}} \\ \boldsymbol{Y}_{\mathcal{SR}} & \boldsymbol{Y}_{\mathcal{SS}} & \boldsymbol{Y}_{\mathcal{SL}} \\ \boldsymbol{Y}_{\mathcal{LR}} & \boldsymbol{Y}_{\mathcal{LS}} & \boldsymbol{Y}_{\mathcal{LL}} \end{bmatrix} \tag{2.13}$$

Using the known subvectors $\boldsymbol{\theta}_{\mathcal{R}}$, $\boldsymbol{V}_{\mathcal{R}}$, and $\boldsymbol{V}_{\mathcal{S}}$, equation (2.11) can be expressed in the following form:

$$\begin{bmatrix} \tilde{\boldsymbol{P}} \\ \tilde{\boldsymbol{Q}} \end{bmatrix} = \begin{bmatrix} \boldsymbol{H} & \boldsymbol{N} \\ \boldsymbol{M} & \boldsymbol{L} \end{bmatrix} \begin{bmatrix} \tilde{\boldsymbol{\theta}} \\ \tilde{\boldsymbol{V}} \end{bmatrix} \tag{2.14}$$

The following presents the derivation of the block matrix $\boldsymbol{H}$, $\boldsymbol{N}$, $\boldsymbol{M}$, $\boldsymbol{L}$.

$$\begin{bmatrix} \boldsymbol{P}_{\mathcal{R}} \\ \boldsymbol{P}_{\mathcal{S}} \\ \boldsymbol{P}_{\mathcal{L}} \\ \boldsymbol{Q}_{\mathcal{R}} \\ \boldsymbol{Q}_{\mathcal{S}} \\ \boldsymbol{Q}_{\mathcal{L}} \end{bmatrix} = - \begin{bmatrix} \boldsymbol{B}'_{\mathcal{RR}} & \boldsymbol{B}'_{\mathcal{RS}} & \boldsymbol{B}'_{\mathcal{RL}} & -\boldsymbol{G}_{\mathcal{RR}} & -\boldsymbol{G}_{\mathcal{RS}} & -\boldsymbol{G}_{\mathcal{RL}} \\ \boldsymbol{B}'_{\mathcal{SR}} & \boldsymbol{B}'_{\mathcal{SS}} & \boldsymbol{B}'_{\mathcal{SL}} & -\boldsymbol{G}_{\mathcal{SR}} & -\boldsymbol{G}_{\mathcal{SS}} & -\boldsymbol{G}_{\mathcal{SL}} \\ \boldsymbol{B}'_{\mathcal{LR}} & \boldsymbol{B}'_{\mathcal{LS}} & \boldsymbol{B}'_{\mathcal{LL}} & -\boldsymbol{G}_{\mathcal{LR}} & -\boldsymbol{G}_{\mathcal{LS}} & -\boldsymbol{G}_{\mathcal{LL}} \\ \boldsymbol{G}_{\mathcal{RR}} & \boldsymbol{G}_{\mathcal{RS}} & \boldsymbol{G}_{\mathcal{RL}} & \boldsymbol{B}_{\mathcal{RR}} & \boldsymbol{B}_{\mathcal{RS}} & \boldsymbol{B}_{\mathcal{RL}} \\ \boldsymbol{G}_{\mathcal{SR}} & \boldsymbol{G}_{\mathcal{SS}} & \boldsymbol{G}_{\mathcal{SL}} & \boldsymbol{B}_{\mathcal{SR}} & \boldsymbol{B}_{\mathcal{SS}} & \boldsymbol{B}_{\mathcal{SL}} \\ \boldsymbol{G}_{\mathcal{LR}} & \boldsymbol{G}_{\mathcal{LS}} & \boldsymbol{G}_{\mathcal{LL}} & \boldsymbol{B}_{\mathcal{LR}} & \boldsymbol{B}_{\mathcal{LS}} & \boldsymbol{B}_{\mathcal{LL}} \end{bmatrix} \begin{bmatrix} \boldsymbol{\theta}_{\mathcal{R}} \\ \boldsymbol{\theta}_{\mathcal{S}} \\ \boldsymbol{\theta}_{\mathcal{L}} \\ \boldsymbol{V}_{\mathcal{R}} \\ \boldsymbol{V}_{\mathcal{S}} \\ \boldsymbol{V}_{\mathcal{L}} \end{bmatrix} \tag{2.15}$$

$$\begin{bmatrix} \boldsymbol{P}_{\mathcal{S}} \\ \boldsymbol{P}_{\mathcal{L}} \\ \boldsymbol{Q}_{\mathcal{L}} \end{bmatrix} = - \begin{bmatrix} \boldsymbol{B}'_{\mathcal{SR}} & -\boldsymbol{G}_{\mathcal{SR}} & -\boldsymbol{G}_{\mathcal{SS}} & \boldsymbol{B}'_{\mathcal{SS}} & \boldsymbol{B}'_{\mathcal{SL}} & -\boldsymbol{G}_{\mathcal{SL}} \\ \boldsymbol{B}'_{\mathcal{LR}} & -\boldsymbol{G}_{\mathcal{LR}} & -\boldsymbol{G}_{\mathcal{RS}} & \boldsymbol{B}'_{\mathcal{LS}} & \boldsymbol{B}'_{\mathcal{LL}} & -\boldsymbol{G}_{\mathcal{LL}} \\ \boldsymbol{G}_{\mathcal{LR}} & \boldsymbol{B}_{\mathcal{LR}} & \boldsymbol{B}_{\mathcal{LS}} & \boldsymbol{G}_{\mathcal{LS}} & \boldsymbol{G}_{\mathcal{LL}} & \boldsymbol{B}_{\mathcal{LL}} \end{bmatrix} \begin{bmatrix} \boldsymbol{\theta}_{\mathcal{R}} \\ \boldsymbol{V}_{\mathcal{R}} \\ \boldsymbol{V}_{\mathcal{S}} \\ \boldsymbol{\theta}_{\mathcal{S}} \\ \boldsymbol{\theta}_{\mathcal{L}} \\ \boldsymbol{V}_{\mathcal{L}} \end{bmatrix} \tag{2.16}$$

$$\begin{bmatrix} \tilde{\boldsymbol{P}} \\ \tilde{\boldsymbol{Q}} \end{bmatrix} = \begin{bmatrix} \boldsymbol{P}_{\mathcal{S}} \\ \boldsymbol{P}_{\mathcal{L}} \\ \boldsymbol{Q}_{\mathcal{L}} \end{bmatrix} + \begin{bmatrix} \boldsymbol{B}'_{\mathcal{SR}} & -\boldsymbol{G}_{\mathcal{SR}} & -\boldsymbol{G}_{\mathcal{SS}} \\ \boldsymbol{B}'_{\mathcal{LR}} & -\boldsymbol{G}_{\mathcal{LR}} & -\boldsymbol{G}_{\mathcal{LS}} \\ \boldsymbol{G}_{\mathcal{LR}} & \boldsymbol{B}_{\mathcal{LR}} & \boldsymbol{B}_{\mathcal{LS}} \end{bmatrix} \begin{bmatrix} \boldsymbol{\theta}_{\mathcal{R}} \\ \boldsymbol{V}_{\mathcal{R}} \\ \boldsymbol{V}_{\mathcal{S}} \end{bmatrix} \tag{2.17}$$

Therefore, the $\boldsymbol{H}$, $\boldsymbol{N}$, $\boldsymbol{M}$, $\boldsymbol{L}$ block matrix , together with the state variables $\tilde{\boldsymbol{\theta}}$ and $\tilde{\boldsymbol{V}}$, can be expressed as follows.

$$\begin{bmatrix} \boldsymbol{H} & \boldsymbol{N} \\ \boldsymbol{M} & \boldsymbol{L} \end{bmatrix} = - \left[\begin{array}{cc|c} \boldsymbol{B}'_{\mathcal{SS}} & \boldsymbol{B}'_{\mathcal{SL}} & -\boldsymbol{G}_{\mathcal{SL}} \\ \boldsymbol{B}'_{\mathcal{LS}} & \boldsymbol{B}'_{\mathcal{LL}} & -\boldsymbol{G}_{\mathcal{LL}} \\ \hline \boldsymbol{G}_{\mathcal{LS}} & \boldsymbol{G}_{\mathcal{LL}} & \boldsymbol{B}_{\mathcal{LL}} \end{array}\right] \tag{2.18}$$

$$\begin{aligned} \tilde{\boldsymbol{\theta}} &= \begin{bmatrix} \boldsymbol{\theta}_{\mathcal{S}}^T, & \boldsymbol{\theta}_{\mathcal{L}}^T \end{bmatrix}^T \\ \tilde{\boldsymbol{V}} &= \boldsymbol{V}_{\mathcal{L}} \end{aligned} \tag{2.19}$$

Equation (2.14) can be transformed via elementary row operations into the following form:

$$\begin{bmatrix} \tilde{\boldsymbol{P}} - \boldsymbol{N}\boldsymbol{L}^{-1}\tilde{\boldsymbol{Q}} \\ \tilde{\boldsymbol{Q}} \end{bmatrix} = \begin{bmatrix} \boldsymbol{H} - \boldsymbol{N}\boldsymbol{L}^{-1}\boldsymbol{M} & \boldsymbol{0} \\ \boldsymbol{M} & \boldsymbol{L} \end{bmatrix} \begin{bmatrix} \tilde{\boldsymbol{\theta}} \\ \tilde{\boldsymbol{V}} \end{bmatrix} \tag{2.20}$$

$$\begin{bmatrix} \tilde{\boldsymbol{P}} \\ \tilde{\boldsymbol{Q}} - \boldsymbol{M}\boldsymbol{H}^{-1}\tilde{\boldsymbol{P}} \end{bmatrix} = \begin{bmatrix} \boldsymbol{H} & \boldsymbol{N} \\ \boldsymbol{0} & \boldsymbol{L} - \boldsymbol{M}\boldsymbol{H}^{-1}\boldsymbol{N} \end{bmatrix} \begin{bmatrix} \tilde{\boldsymbol{\theta}} \\ \tilde{\boldsymbol{V}} \end{bmatrix} \tag{2.21}$$

Combining the first part of (2.20) and the second part of (2.21) into one equation leads to the decoupling of voltage magnitudes and phase angles:

$$\begin{bmatrix} \tilde{\boldsymbol{P}} - \boldsymbol{N}\boldsymbol{L}^{-1}\tilde{\boldsymbol{Q}} \\ \tilde{\boldsymbol{Q}} - \boldsymbol{M}\boldsymbol{H}^{-1}\tilde{\boldsymbol{P}} \end{bmatrix} = \begin{bmatrix} \tilde{\boldsymbol{H}} & \boldsymbol{0} \\ \boldsymbol{0} & \tilde{\boldsymbol{L}} \end{bmatrix} \begin{bmatrix} \tilde{\boldsymbol{\theta}} \\ \tilde{\boldsymbol{V}} \end{bmatrix} \tag{2.22}$$

where

$$\tilde{\boldsymbol{H}} = \boldsymbol{H} - \boldsymbol{N}\boldsymbol{L}^{-1}\boldsymbol{M} \tag{2.23}$$

$$\tilde{\boldsymbol{L}} = \boldsymbol{L} - \boldsymbol{M}\boldsymbol{H}^{-1}\boldsymbol{N} \tag{2.24}$$

From (2.22), the following expressions are obtained for determining $\tilde{\boldsymbol{V}}$ and $\tilde{\boldsymbol{\theta}}$ in terms of the known quantities $\tilde{\boldsymbol{P}}$ and $\tilde{\boldsymbol{Q}}$.

$$\tilde{\boldsymbol{\theta}} = \tilde{\boldsymbol{H}}^{-1}\tilde{\boldsymbol{P}} - \tilde{\boldsymbol{H}}^{-1}\boldsymbol{N}\boldsymbol{L}^{-1}\tilde{\boldsymbol{Q}} \tag{2.25}$$

$$\tilde{\boldsymbol{V}} = \tilde{\boldsymbol{L}}^{-1}\tilde{\boldsymbol{Q}} - \tilde{\boldsymbol{L}}^{-1}\boldsymbol{M}\boldsymbol{H}^{-1}\tilde{\boldsymbol{P}} \tag{2.26}$$

Decoupling does not imply a complete neglect of the coupling between active and reactive power. Instead, this coupling is simplified through matrix operations, while their mutual influence is still preserved. The corresponding equations (2.25) and (2.26) provide a structured approach to separately compute the voltage magnitudes and phase angles. Although the coupling relationship is simplified in the process, it is still embedded in the expressions in a structured form, thereby ensuring the accuracy of the computation.

2.2.3. Transformers and Phase Shifters

This section addresses the modeling adjustments required when transformers or phase shifters are present in the system(see Figure 2.1, where t denotes the tap ratio and θ_s the phase-shifting angle). The discussion is divided into two parts:

- Contributions to the Admittance Matrix;
- Influence on the Branch MW Flow.

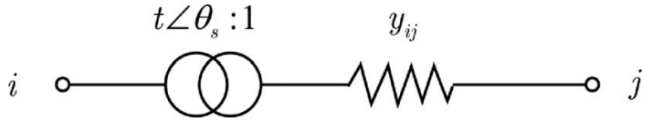

Figure 2.1: Transmission Line Model with Phase-Shifting Transformer.

Contributions to the Admittance Matrix

Figure 2.2 illustrates a simple transmission line model. Based on this model, the basic form of the nodal admittance matrix can be derived by applying Kirchhoff's Current Law (KCL) at each bus and using the admittance values between nodes. This approach can further be extended to accommodate more complex components such as phase-shifting transformers and tap-changing devices. The effects of these components are reflected in the admittance matrix through modified admittance values and the introduction of additional phase angles.

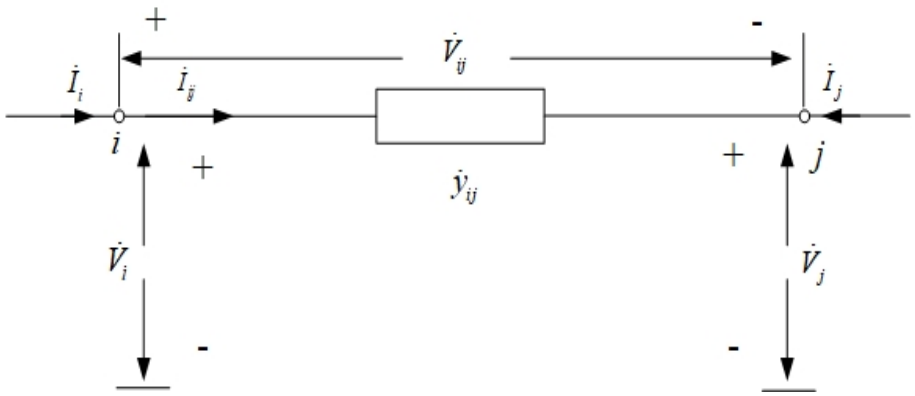

Figure 2.2: Simple two-bus system used for deriving the nodal admittance matrix.

The current and voltage are represented by

$$\begin{bmatrix} I_i \\ I_j \end{bmatrix} = \begin{bmatrix} 1 \\ -1 \end{bmatrix} I_{ij}$$
$$\begin{bmatrix} 1 & -1 \end{bmatrix} \begin{bmatrix} V_i \\ V_j \end{bmatrix} = V_{ij} \tag{2.27}$$

It is known that $y_{ij}V_{ij} = I_{ij}$, thus the above expression can be reformulated in matrix notation as follows:

$$\begin{bmatrix} 1 \\ -1 \end{bmatrix} y_{ij} \begin{bmatrix} 1 & -1 \end{bmatrix} \begin{bmatrix} V_i \\ V_j \end{bmatrix} = \begin{bmatrix} I_i \\ I_j \end{bmatrix}$$
$$\boldsymbol{Y}_{\text{bus}} = \begin{bmatrix} 1 \\ -1 \end{bmatrix} y_{ij} \begin{bmatrix} 1 & -1 \end{bmatrix} \tag{2.28}$$

According to the formation of nodal admittance matrix, the impact of a branch equipped with a phase-shifting transformer (see Figure 2.3) is reflected in the matrix through the following contributions.

$$\Delta \boldsymbol{Y} = \boldsymbol{C} y_{ij} \overline{\boldsymbol{C}}^{T} \tag{2.29}$$

Here, $\boldsymbol{C}$ is a column vector consisting of zeros except at two positions: the i_{th} element is $\boldsymbol{C_i} = \frac{1}{te^{-j\theta_s}}$ and $\boldsymbol{C_j} = -1$. $\overline{\boldsymbol{C}}$ is the conjugate of $\boldsymbol{C}$.

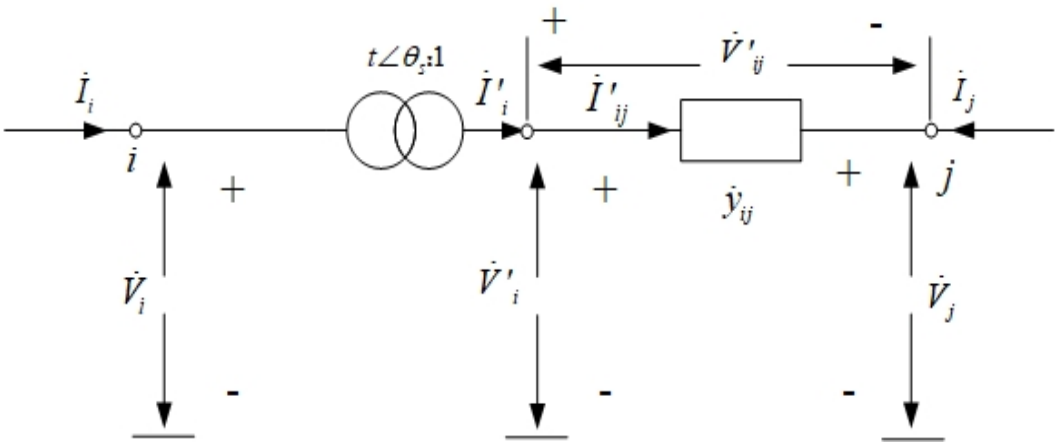

Figure 2.3: Two-bus System equipped with Phase Shifting Transformer

Based on the transformer's turns ratio and the principle of power conservation in an ideal transformer, the transformer admittance matrix can be derived as follows.

$$\begin{aligned}
&\frac{\dot{V}_i}{\dot{V}'_i} = t\angle\theta_s \\
&\dot{V}_i = t\angle\theta_s \cdot \dot{V}'_i \\
&\dot{V}_i \tilde{I}_i = \dot{V}'_i \tilde{I}'_i \\
&\dot{I}'_i = t\angle(-\theta_s) \cdot \dot{I}_i
\end{aligned} \tag{2.30}$$

Thus, the expressions for the voltage and current are given by:

$$\begin{aligned}\begin{bmatrix} I_i \\ I_j \end{bmatrix} &= \begin{bmatrix} \frac{1}{t\angle -\theta_s} \\ -1 \end{bmatrix} I'_{ij} \\ \begin{bmatrix} \frac{1}{t\angle \theta_s} & -1 \end{bmatrix} \begin{bmatrix} V_i \\ V_j \end{bmatrix} &= V'_{ij}\end{aligned} \tag{2.31}$$

It is known that $y_{ij}V'_{ij} = I'_{ij}$, then formulations can be derived that

$$\begin{bmatrix} \frac{1}{t\angle -\theta_s} \\ -1 \end{bmatrix} y_{ij} \begin{bmatrix} \frac{1}{t\angle \theta_s} & -1 \end{bmatrix} \begin{bmatrix} V_i \\ V_j \end{bmatrix} = \begin{bmatrix} I_i \\ I_j \end{bmatrix} \tag{2.32}$$

Therefore, $\Delta \boldsymbol{Y}$ can be split into two parts, as illustrated by the following expression:

$$\Delta \boldsymbol{Y} = \Delta \boldsymbol{Y}_1 + \Delta \boldsymbol{Y}_2 = \begin{bmatrix} \frac{y_{ij}}{t^2} & \frac{-1}{t\angle -\theta_s} y_{ij} \\ \frac{-1}{t\angle \theta_s} y_{ij} & y_{ij} \end{bmatrix} \tag{2.33}$$

where $\Delta \boldsymbol{Y_1}$ are non-zero elements, and let $\dot{k}$ denote $\frac{1}{t\angle \theta_s}$, and $\tilde{k}$ denote $\frac{1}{t\angle -\theta_s}$.

$$\begin{aligned}\Delta \boldsymbol{Y}_{1,ii} &= -\Delta \boldsymbol{Y}_{1,ij} = \tilde{k} y_{ij} = \frac{y_{ij}}{te^{-j\theta_s}} \\ \Delta \boldsymbol{Y}_{1,jj} &= -\Delta \boldsymbol{Y}_{1,ji} = \dot{k} y_{ij} = \frac{y_{ij}}{te^{j\theta_s}}\end{aligned} \tag{2.34}$$

while $\Delta \boldsymbol{Y_2}$ is a diagonal matrix with only two non-zero elements:

$$\begin{aligned}\Delta \boldsymbol{Y}_{2,ii} &= k^2 y_{ij} - \tilde{k} y_{ij} = \frac{y_{ij}}{t^2} - \frac{y_{ij}}{te^{-j\theta_s}} \\ \Delta \boldsymbol{Y}_{2,jj} &= y_{ij} - \dot{k} y_{ij} = y_{ij} - \frac{y_{ij}}{te^{j\theta_s}}\end{aligned} \tag{2.35}$$

In fact, $\Delta \boldsymbol{Y_1}$ represents the contribution of the equivalent line admittance to $\boldsymbol{Y}$, and $\Delta \boldsymbol{Y_2}$ can be interpreted as the equivalent shunt elements associated with phase-shifting transformers.

Contributions to the Branch MW Flow

In the branch shown in Figure 2.3, the relationship between complex power and the

associated bus voltage magnitudes and angles is given by:

$$\begin{aligned}\begin{bmatrix}\tilde{S}_{ij}\\ \tilde{S}_{ji}\end{bmatrix} &= \begin{bmatrix}\tilde{V}_i\dot{I}_i^*\\ \tilde{V}_j\dot{I}_j^*\end{bmatrix}\\ &= \begin{bmatrix}V_i e^{-j\theta_i} & 0\\ 0 & V_j e^{-j\theta_j}\end{bmatrix}\begin{bmatrix}\frac{y_{ij}}{t^2} & -\frac{y_{ij}}{te^{-j\theta_s}}\\ -\frac{y_{ij}}{te^{j\theta_s}} & y_{ij}\end{bmatrix}\begin{bmatrix}V_i e^{j\theta_i}\\ V_j e^{j\theta_j}\end{bmatrix}\end{aligned} \tag{2.36}$$

The branch power flow can be expressed in terms of the real and imaginary parts of the complex power $\tilde{S}_{ij}$. Given that the branch admittance is defined as $y_{ij} = g_{ij} + jb_{ij}$, and by applying Euler's formula,

$$e^{-j\Delta\theta} = \cos(\Delta\theta) - j\sin(\Delta\theta),$$

where $\Delta\theta = \theta_i - \theta_j - \theta_s$, the exponential terms in the complex power expression can be decomposed into their trigonometric components. This enables the separation of the real and imaginary parts of the power flow, leading to the analytical expressions for the active and reactive power:

$$P_{ij} = \mathrm{Re}(\tilde{S}_{ij}), \quad Q_{ij} = \mathrm{Im}(\tilde{S}_{ij}).$$

$$\begin{aligned}P_{ij} &= \mathrm{Re}\left(V_i e^{-j\theta_i}\left(\frac{y_{ij}}{t^2}V_i e^{j\theta_i} - \frac{y_{ij}}{te^{-j\theta_s}}V_j e^{j\theta_j}\right)\right)\\ &= \mathrm{Re}\left(\frac{y_{ij}}{t^2}V_i^2 - \frac{y_{ij}}{t}V_iV_j e^{-j(\theta_i-\theta_j-\theta_s)}\right)\\ &= \frac{g_{ij}}{t}V_i\left(\frac{V_i}{t} - V_j\cos(\theta_i-\theta_j-\theta_s)\right) - \frac{b_{ij}}{t}V_iV_j\sin(\theta_i-\theta_j-\theta_s)\\ &\approx \frac{g_{ij}}{t}\left(\frac{V_i}{t} - V_j\right) - \frac{b_{ij}}{t}(\theta_i-\theta_j-\theta_s)\end{aligned} \tag{2.37}$$

$$
\begin{aligned}
Q_{ij} &= \mathrm{Im}\left(V_i e^{-j\theta_i}\left(\frac{y_{ij}}{t^2}V_i e^{j\theta_i} - \frac{y_{ij}}{te^{-j\theta_s}}V_j e^{j\theta_j}\right)\right) \\
&= \mathrm{Im}\left(\frac{y_{ij}}{t^2}V_i^2 - \frac{y_{ij}}{t}V_i V_j e^{-j(\theta_i-\theta_j-\theta_s)}\right) \\
&= \frac{b_{ij}}{t}V_i\left(\frac{V_i}{t} - V_j\cos(\theta_i-\theta_j-\theta_s)\right) + \frac{g_{ij}}{t}V_i V_j \sin(\theta_i-\theta_j-\theta_s) \\
&\approx \frac{b_{ij}}{t}\left(\frac{V_i}{t} - V_j\right) + \frac{g_{ij}}{t}\left(\theta_i-\theta_j-\theta_s\right)
\end{aligned}
\tag{2.38}
$$

The final step in (2.37) and (2.38) adopts an approximation similar to that in (2.5) and (2.6), respectively, which leads to linear expressions for both active and reactive power flows in branches with transformers or phase shifters.

3 | Power System Simulation with DLPF Method

This chapter demonstrates the theoretical derivations with numerical examples and assesses the *DLPF* model's accuracy and computational efficiency through case studies on distribution networks and large-scale meshed grids.

3.1. Numerical Study

To demonstrate the applicability and effectiveness of the proposed model, a numerical case study is conducted. The following subsection presents the results for a small power system power flow, which serves as a simplified example to illustrate the key concepts and computational procedures.

3.1.1. Case for a small power system

The one-line diagram of a four-bus transmission system is shown in Figure 3.1 below. Two generators are connected at buses 1 (slack) and 4 (voltage-controlled), while buses 2 and 3 serve as load buses. The line data give per-unit series impedance and line-charging susceptances for the nominal-π equivalents of the four lines identified by the buses at which they terminate. And the bus data list active power$P$, reactive power Q, and V at each bus. The slack bus voltage magnitude $|V_1|$ and angle δ_1, as well as the PV bus voltage $|V_4|$ are held at their specified values throughout the analysis.

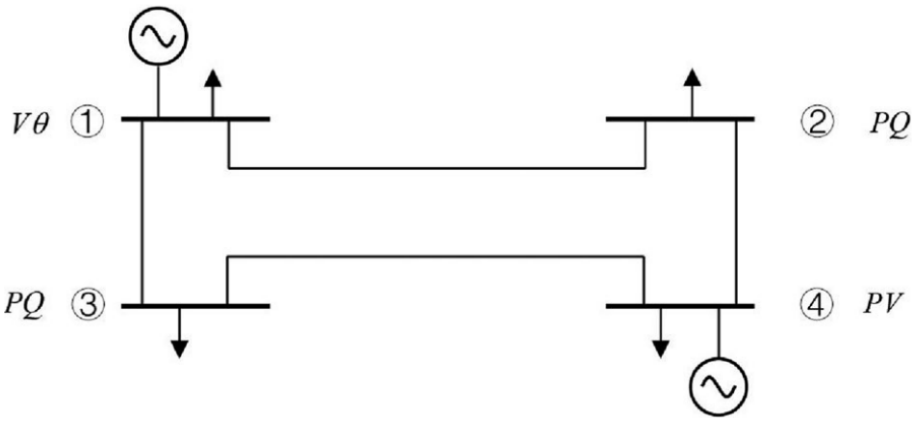

Figure 3.1: Four-bus Transmission System.

The following tables present the steady-state input data for the four-bus test system in the load-flow study. Table 3.1 provides bus data including generation, loads and prescribed voltage magnitudes and angles. Table 3.2 details the π-model line parameters and each line's shunt charging values.

Bus	$\boldsymbol{P}_{\text{gen}}$ (MW)	$\boldsymbol{Q}_{\text{gen}}$ (Mvar)	$\boldsymbol{P}_{\text{load}}$ (MW)	$\boldsymbol{Q}_{\text{load}}$ (Mvar)	$\boldsymbol{V}$ (pu)	**Remarks**
1	—	—	50	30.99	1.00	Slack bus
2	0	0	170	105.35	1.00	PQ bus
3	0	0	200	123.94	1.00	PQ bus
4	318	197.08	80	49.58	1.02	PV bus

Table 3.1: Bus Data for the Four-Bus System: Generation, Load and Voltage[27].

Line	**R(pu)**	**X (pu)**	**G (pu)**	**B (pu)**	$Y/2$ **(pu)**
1–2	0.01008	0.05040	3.815629	-19.078144	0.05125
1–3	0.00744	0.03720	5.169561	-25.847809	0.03875
2–4	0.00744	0.03720	5.169561	-25.847809	0.03875
3–4	0.01272	0.06360	3.023705	-15.118528	0.06375

Table 3.2: Line data for the Four-Bus System[27].

3.1.2. Power System Load Flow Analysis and Solution Procedure

1. **Calculation of the Admittance Matrix** The Bus Admittance Matrix is

$$\boldsymbol{Y}_{\text{bus}} = \boldsymbol{A}^T \boldsymbol{Y}_{\text{branch}} \boldsymbol{A}$$

$$= \begin{bmatrix} 8.98519 - \text{j}44.925953 & -3.815629 + \text{j}19.078144 & -5.169561 + \text{j}25.847809 & 0 \\ -3.815629 + \text{j}19.078144 & 8.98519 - \text{j}44.925953 & 0 & -5.169561 + \text{j}25.847809 \\ -5.169561 + \text{j}25.847809 & 0 & 8.193266 - \text{j}40.966337 & -3.023705 + \text{j}15.118528 \\ 0 & -5.169561 + \text{j}25.847809 & -3.023705 + \text{j}15.118528 & 8.193266 - \text{j}40.966337 \end{bmatrix}$$

$$\boldsymbol{Y}_{\text{bus}} \in \mathbb{C}^{n_{\text{bus}} \times n_{\text{bus}}}$$

The shunt admittance matrix $\boldsymbol{Y}_{\text{sh}}$ is

$$\boldsymbol{Y}_{\text{sh}} = \begin{bmatrix} \text{j}0.09 & 0 & 0 & 0 \\ 0 & \text{j}0.09 & 0 & 0 \\ 0 & 0 & \text{j}0.1025 & 0 \\ 0 & 0 & 0 & \text{j}0.1025 \end{bmatrix} \in \mathbb{C}^{n_{\text{bus}} \times n_{\text{bus}}}$$

Total Admittance Matrix (Including Shunt Admittances) is

$$\boldsymbol{Y} = \boldsymbol{Y}_{\text{bus}} + \boldsymbol{Y}_{\text{sh}}$$

$$= \begin{bmatrix} 8.98519 - \text{j}44.835953 & -3.815629 + \text{j}19.078144 & -5.169561 + \text{j}25.847809 & 0 \\ -3.815629 + \text{j}19.078144 & 8.98519 - \text{j}44.835953 & 0 & -5.169561 + \text{j}25.847809 \\ -5.169561 + \text{j}25.847809 & 0 & 8.193266 - \text{j}40.863837 & -3.023705 + \text{j}15.118528 \\ 0 & -5.169561 + \text{j}25.847809 & -3.023705 + \text{j}15.118528 & 8.193266 - \text{j}40.863837 \end{bmatrix}$$

$$\boldsymbol{Y} \in \mathbb{C}^{4 \times 4}.$$

2. **Matrices Required for the Decoupled Linearized Power Flow (*DLPF*) Model** In the *DLPF* algorithm, the bus admittance matrix is partitioned into its real and imaginary sub-matrices, which are then used in the $\Delta\delta$ and ΔV update equations.

$$\boldsymbol{Y} = \boldsymbol{Y}_{\text{bus}} + \boldsymbol{Y}_{\text{sh}} \tag{3.1}$$

$$\boldsymbol{Y}' = \boldsymbol{Y}_{\text{bus}} \tag{3.2}$$

$$\boldsymbol{G} = \text{Re}\big(\boldsymbol{Y}\big) = \begin{bmatrix} 8.98519 & -3.815629 & -5.169561 & 0 \\ -3.815629 & 8.98519 & 0 & -5.169561 \\ -5.169561 & 0 & 8.193266 & -3.023705 \\ 0 & -5.169561 & -3.023705 & 8.193266 \end{bmatrix}$$

$$\boldsymbol{B} = \text{Im}\big(\boldsymbol{Y}\big) = \begin{bmatrix} -44.835953 & 19.078144 & 25.847809 & 0 \\ 19.078144 & -44.835953 & 0 & 25.847809 \\ 25.847809 & 0 & -40.863837 & 15.118528 \\ 0 & 25.847809 & 15.118528 & -40.863837 \end{bmatrix}$$

$$\boldsymbol{B}' = \text{Im}\big(\boldsymbol{Y}_{\text{bus}}\big) = \begin{bmatrix} -44.925953 & 19.078144 & 25.847809 & 0 \\ 19.078144 & -44.925953 & 0 & 25.847809 \\ 25.847809 & 0 & -40.966337 & 15.118528 \\ 0 & 25.847809 & 15.118528 & -40.966337 \end{bmatrix}$$

Based on the bus admittance matrix, the following sub-matrices are defined:

$$\boldsymbol{H} = \begin{bmatrix} 40.966337 & -25.847809 & -15.118528 \\ -25.847809 & 44.925953 & 0 \\ -15.118528 & 0 & 40.966337 \end{bmatrix}$$

$$\boldsymbol{N} = \begin{bmatrix} -5.169561 & -3.023705 \\ 8.985190 & 0 \\ 0 & 8.193266 \end{bmatrix}$$

$$\boldsymbol{M} = \begin{bmatrix} 5.169561 & -8.985190 & 0 \\ 3.023705 & 0 & -8.193266 \end{bmatrix}$$

$$\boldsymbol{L} = \begin{bmatrix} 44.835953 & 0 \\ 0 & 40.863837 \end{bmatrix}$$

3. **Computation for Power Mismatch Vector and Constant Terms**

The net scheduled real and reactive power injections at each bus together with the prescribed reference voltage angles and magnitudes can be written as

$$\begin{bmatrix} \boldsymbol{P_S} \\ \boldsymbol{P_L} \\ \boldsymbol{Q_L} \end{bmatrix} = \begin{bmatrix} 3.18 - 0.80 \\ 0 - 1.70 \\ 0 - 2.00 \\ 0 - 1.0535 \\ 0 - 1.2394 \end{bmatrix}, \quad \begin{bmatrix} \boldsymbol{\theta_R} \\ \boldsymbol{V_R} \\ \boldsymbol{V_S} \end{bmatrix} = \begin{bmatrix} 0 \\ 1.00 \\ 1.02 \end{bmatrix}$$

$$\begin{bmatrix} \boldsymbol{B}'_{SR} & -\boldsymbol{G}_{SR} & -\boldsymbol{G}_{SS} \\ \boldsymbol{B}'_{LR} & -\boldsymbol{G}_{LR} & -\boldsymbol{G}_{LS} \\ \boldsymbol{G}_{CR} & \boldsymbol{B}_{CR} & \boldsymbol{B}_{CS} \end{bmatrix} = \begin{bmatrix} 0 & 0 & -8.193267 \\ 19.078144 & 3.815629 & 5.169561 \\ 25.847809 & 5.169561 & 3.023705 \\ -3.815629 & 19.078144 & 25.847809 \\ -5.169561 & 25.847809 & 15.118528 \end{bmatrix}$$

$$\tilde{\boldsymbol{P}} = \begin{bmatrix} -5.977133 \\ 7.388582 \\ 6.253742 \end{bmatrix}, \quad \tilde{\boldsymbol{Q}} = \begin{bmatrix} 44.389408 \\ 40.029308 \end{bmatrix}$$

4. **Computed Load-Flow Results**

$$\tilde{\boldsymbol{\theta}} = \tilde{\boldsymbol{H}}^{-1}\,\tilde{\boldsymbol{P}} - \tilde{\boldsymbol{H}}^{-1}\,\boldsymbol{N}\,\boldsymbol{L}^{-1}\,\tilde{\boldsymbol{Q}} = \begin{bmatrix} 0.028357 \\ -0.015939 \\ -0.031126 \end{bmatrix}$$

$$\tilde{\boldsymbol{V}} = \tilde{\boldsymbol{L}}^{-1}\,\tilde{\boldsymbol{Q}} - \tilde{\boldsymbol{L}}^{-1}\,\boldsymbol{M}\,\boldsymbol{H}^{-1}\,\tilde{\boldsymbol{P}} = \begin{bmatrix} 0.983577 \\ 0.971239 \end{bmatrix}$$

3.2. Model Performance Comparison and Analysis

To evaluate the accuracy and computational performance of the proposed DLPF method, its results are compared with those obtained from the ACPF and DCPF models. The following sections present the main metrics used to assess model error and accuracy, followed by comparative tests on two representative classes of power networks to systematically evaluate the overall performance of the DLPF model in terms of accuracy and computational efficiency. The results demonstrate that the DLPF method achieves a close approximation to the ACPF solution while significantly reducing computational effort, thus offering both high precision and efficiency suitable for large-scale power system applications.

All simulations were carried out in MATLAB/MATPOWER Version 8.0.1 on a workstation equipped with an Intel i9 2.20 GHz CPU and 32 GB RAM. The evaluation metrics

include bus voltage magnitudes, branch real-power flows, and computation times, with errors of *DLPF* model measured relative to the benchmark power-flow solution.

3.2.1. Error Evaluation Indicators and Definition

Mean Absolute Error (MAE) is a commonly used evaluation metric that reflects the overall deviation between the model's results and the reference solution. The mean absolute error of voltage magnitudes between the reference solution and the model's results is defined as

$$\mathrm{MAE}_{\mathrm{vm}} = \frac{1}{N}\sum_{i=1}^{N}\left|V_i^{\mathrm{model}} - V_i^{\mathrm{ref}}\right| \tag{3.3}$$

where:

- V_i^{ref} is the reference voltage magnitude at bus i (e.g., from AC power-flow, in p.u.).
- V_i^{model} is the voltage magnitude at bus i calculated by the test model (in p.u.).
- N is the total number of buses in the network.

The mean absolute error of branch active-power flows is defined as

$$\mathrm{MAE}_P = \frac{1}{M}\sum_{k=1}^{M}\left|P_k^{\mathrm{model}} - P_k^{\mathrm{ref}}\right| \tag{3.4}$$

where:

- P_k^{ref} is the reference active-power flow on branch k (e.g., from AC power-flow, in MW).
- P_k^{model} is the active-power flow on branch k calculated by the test model (in MW).
- M is the total number of branches in the network.

The Key Characteristics of MAE is

- It directly reports the average per-unit voltage error, allowing comparison with operational limits.
- It uses absolute differences so that positive and negative deviations do not cancel out, accurately reflecting the overall error.

- It does not disproportionately weight infrequent large deviations, providing a balanced measure of typical performance.
- It is widely used to compare linearized or reduced-order models against AC solutions for prediction accuracy.

Therefore, the error analysis below uses these metrics to quantify the deviations in voltage magnitude and active-power flow predicted by each model. In the subsequent analysis, the error analysis use the following metrics, defined as:

$$\varepsilon_V^{\mathrm{DCPF}} = \mathrm{MAE}_{v_m}^{\mathrm{DCPF}} = \frac{1}{N_{\mathrm{bus}}} \sum_{i=1}^{N_{\mathrm{bus}}} \left| V_i^{\mathrm{DCPF}} - V_i^{\mathrm{ref}} \right| \tag{3.5}$$

$$\varepsilon_V^{\mathrm{DLPF}} = \mathrm{MAE}_{v_m}^{\mathrm{DLPF}} = \frac{1}{N_{\mathrm{bus}}} \sum_{i=1}^{N_{\mathrm{bus}}} \left| V_i^{\mathrm{DLPF}} - V_i^{\mathrm{ref}} \right| \tag{3.6}$$

$$\varepsilon_P^{\mathrm{DCPF}} = \mathrm{MAE}_P^{\mathrm{DCPF}} = \frac{1}{M} \sum_{k=1}^{M} \left| P_k^{\mathrm{DCPF}} - P_k^{\mathrm{ref}} \right| \tag{3.7}$$

$$\varepsilon_P^{\mathrm{DLPF}} = \mathrm{MAE}_P^{\mathrm{DLPF}} = \frac{1}{M} \sum_{k=1}^{M} \left| P_k^{\mathrm{DLPF}} - P_k^{\mathrm{ref}} \right| \tag{3.8}$$

3.2.2. Balanced Radial Distribution Systems Simulation

Radial distribution networks have a tree-like structure, with each load node connected to the substation by a single path. In general, the radial distribution network has a high R/X ratio,which leads to more power losses and voltage drop [28].It should be noted that an average error of 0.05 p.u. in voltage magnitude is beyond tolerance, given that the operational voltage limit is typically between 0.95 p.u. and 1.05 p.u. [25].
To address these challenges, this thesis systematically compares the traditional ACPF with DCPF models and the proposed DLPF model across multiple distribution network test systems, evaluating each model's performance in both power flow calculations and voltage profiles.
Table 3.3 compares the error metrics of the DLPF and DCPF models against those obtained from the reference ACPF for nodal voltage and branch active power calculations.

While Figure 3.2 and Figure 3.3 offers a visual comparison of each model's voltage magnitude distribution and branch power flow distribution in the 69-node system. The bus voltage profile is assumed to be flat at 1.0 p.u. in the DCPF model.

Test Case	$\varepsilon_V^{\text{DCPF}}$	$\varepsilon_V^{\text{DLPF}}$	$\varepsilon_P^{\text{DCPF}}$	$\varepsilon_P^{\text{DLPF}}$
Case 33-bus	0.054	0.004	0.042	0.030
Case 69-bus	0.027	0.002	0.049	0.004
Case 94-bus	0.097	0.012	0.469	0.033
Case 118-bus	0.044	0.003	0.095	0.005
Case 533-bus	0.005	0.001	0.003	0.001

Table 3.3: Errors of Different Power Flow Models Compared to ACPF in Selected Test Distribution Systems

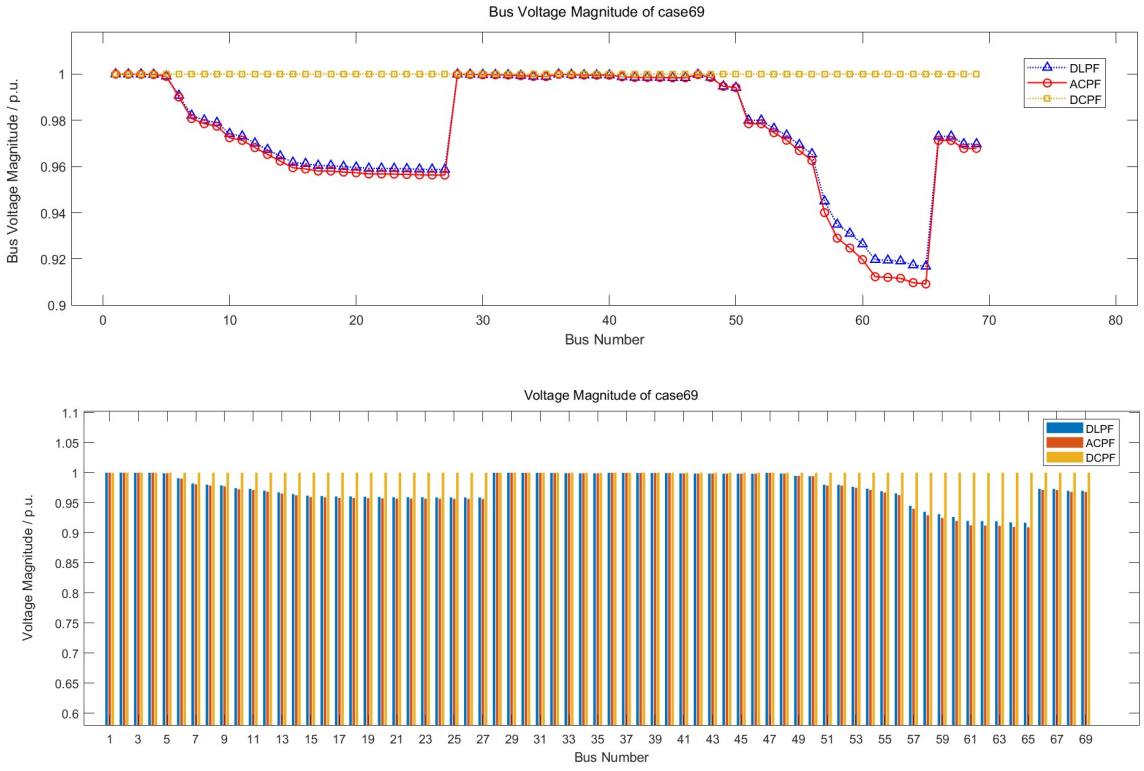

Figure 3.2: Comparison of Bus Voltage Magnitudes for Case 69 using DLPF, ACPF and DCPF methods.

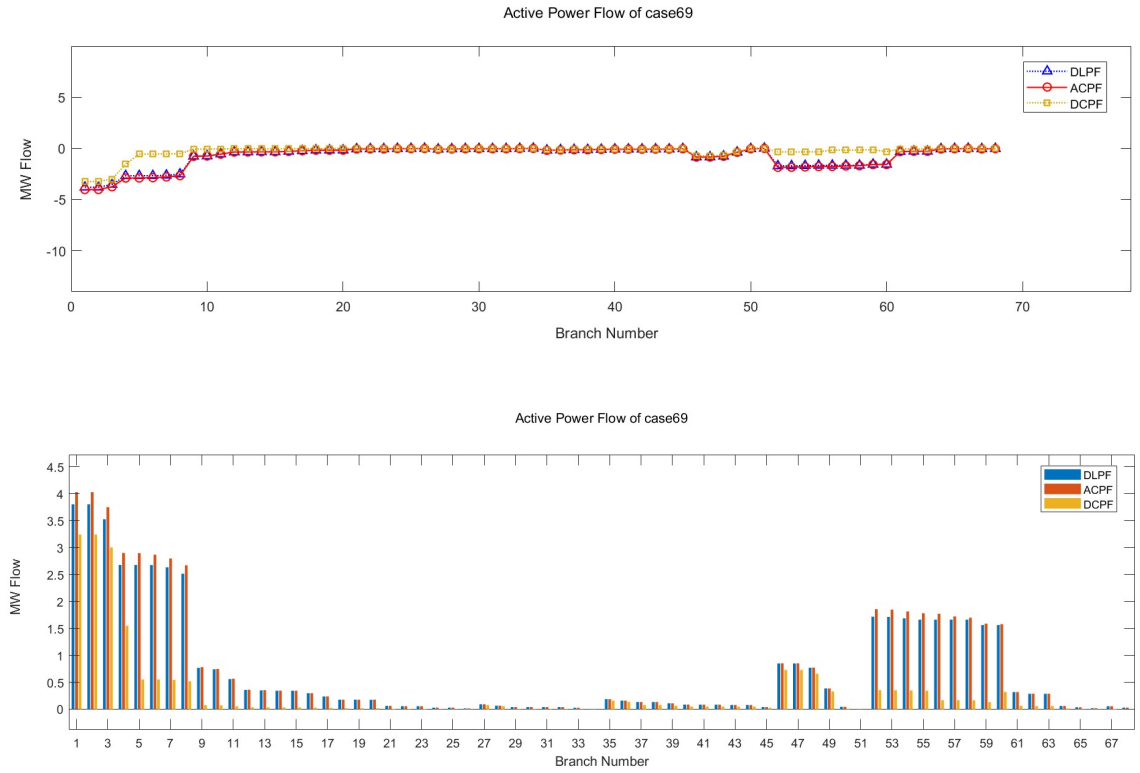

Figure 3.3: Comparison of Active Power Flow for Case 69 Using DLPF, ACPF and DCPF Methods.

In distribution networks, to ensure that bus voltages remain within the operational range, it is typically required that the mean absolute error of voltage magnitude MAE_{v_m} be kept at a lower level to guarantee the reliability and accuracy of voltage regulation.

Based on the results presented in the above tables and figures, the following main conclusions can be drawn:

1. **Voltage error comparison**
   DLPF method is able to keep the mean absolute bus voltage error ε_V within 0.01 p.u. in most test cases, whereas the classic DCPF method shows noticeably larger deviations. In distribution networks with high R/X ratios that are prone to voltage drops, DLPF more accurately captures the bus-voltage profile (see Case 69).

2. **Active power flow error comparison**
   For the mean absolute error of active power ε_P, DLPF again performs excellently, with errors remaining at acceptable levels across most systems. By contrast, DCPF's errors in complex or large-scale networks can reach 0.4–0.5 p.u., far exceeding those of DLPF. This is higher than the errors produced by DLPF and does not satisfy

practical dispatch and loss estimation requirements.

Therefore, for radial distribution networks with high R/X ratios, the DLPF method ensures voltage accuracy requirements. It can serves as a reliable benchmark for real-time power flow analysis in distribution network.

3.2.3. Meshed Transmission Systems

Meshed transmission systems feature looped topologies with multiple parallel paths between generation and load nodes, providing enhanced supply reliability by allowing power to be rerouted if a path becomes unavailable. Unlike radial distribution networks, meshed transmission network generally have lower R/X ratios and consequently smaller per-unit voltage drops, which improves overall voltage stability [29]. For these reasons, meshed transmission is the preferred means of high-voltage and ultra-high-voltage long-distance, large-capacity power transfer; however, its control and protection schemes are more complex, placing greater demands on system analysis, real-time dispatch, and fault management.

In this thesis, both the DCPF and DLPF models are evaluated against the ACPF solution across multiple meshed transmission test systems to assess the accuracy of each method in terms of power flow calculation and voltage profile.

Table 3.4 summarizes the error metrics for the meshed transmission systems against full ACPF reference solutions, while Figure 3.4 and Figure 3.5 illustrate the voltage magnitude and branch active power distributions for the IEEE 118-bus case.

Test Case	$\varepsilon_V^{\text{DCPF}}$	$\varepsilon_V^{\text{DLPF}}$	$\varepsilon_P^{\text{DCPF}}$	$\varepsilon_P^{\text{DLPF}}$
IEEE 30-bus	0.018	0.001	0.01	0.002
IEEE 57-bus	0.023	0.013	0.03	0.010
IEEE 118-bus	0.023	0.001	0.051	0.033
IEEE 300-bus	0.025	0.014	0.113	0.092
Pegase 1354-bus	0.033	0.009	0.150	0.125
Pegase 2869-bus	0.030	0.008	0.174	0.154
Pegase 8387-bus	0.048	0.003	0.220	0.158

Table 3.4: Errors of Different Power Flow Models Compared to ACPF in Selected Test Transmission Systems.

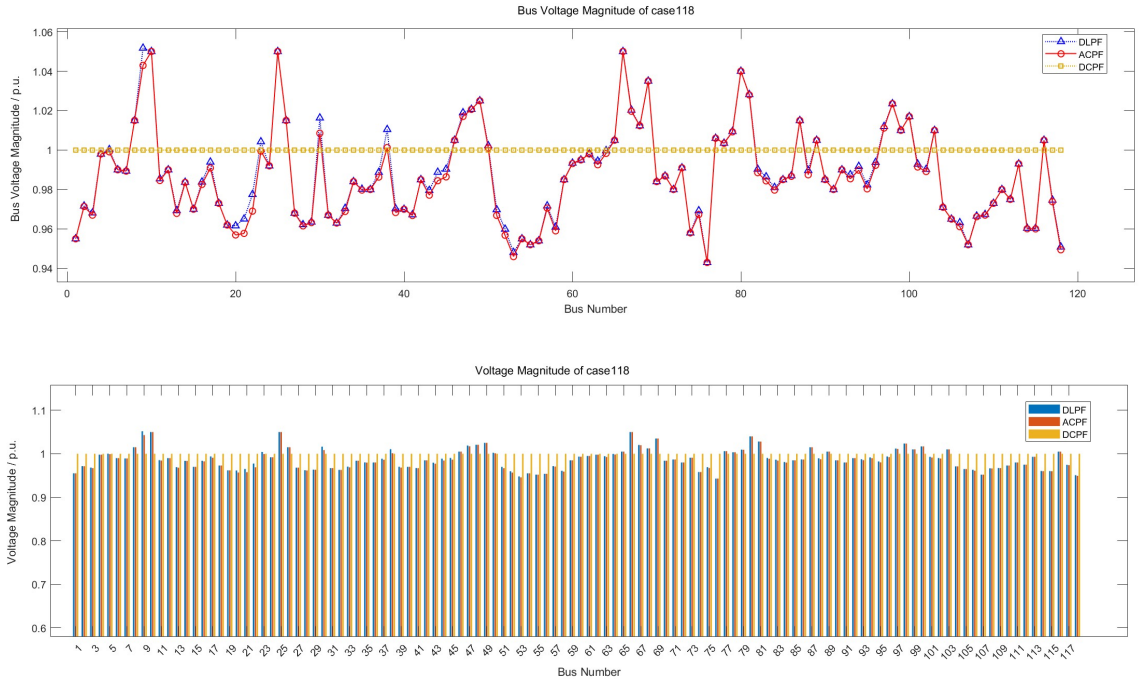

Figure 3.4: Comparison of Bus Voltage Magnitudes for Case 118 using DLPF, ACPF and DCPF methods.

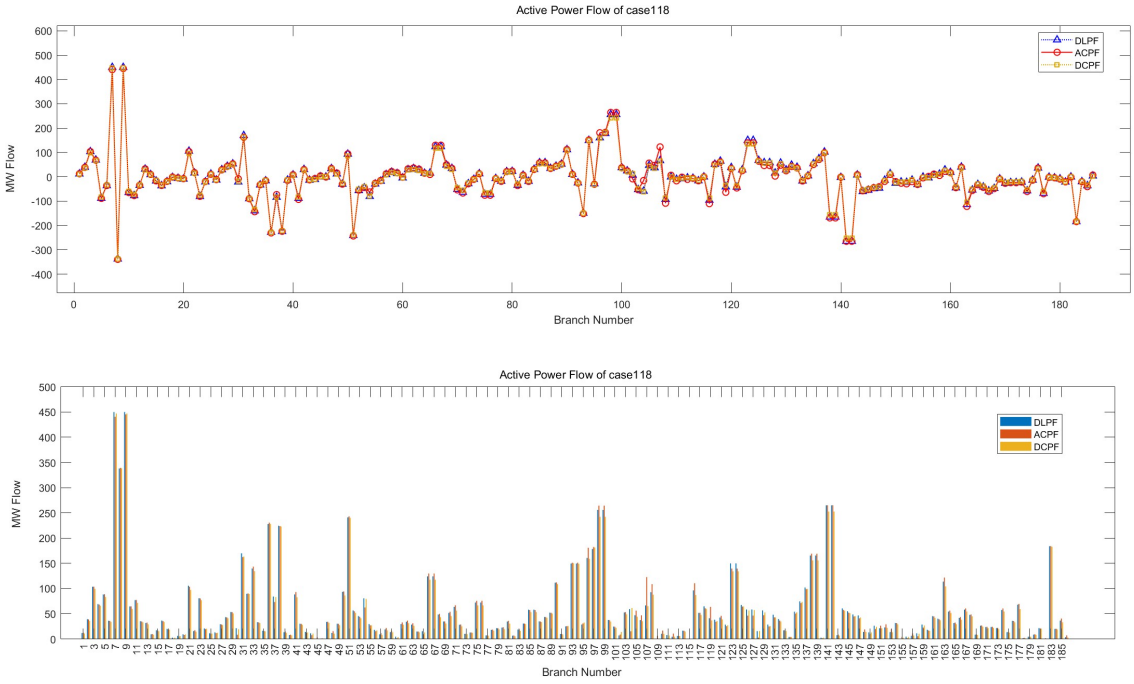

Figure 3.5: Comparison of Bus Voltage Magnitudes for Case 118 using DLPF, ACPF and DCPF methods.

In meshed transmission networks, to ensure voltage stability and the accuracy of power calculations, the MAE of voltage magnitude ε_V and MAE of branch active power ε_P must be kept very low. With regard to transmission systems of varying scale, the comparative analysis reveals the following conclusions:

1. **Voltage error comparison**
   Using the DLPF model, ε_V remains in a very low range across all test cases, which means that the voltage profile it predicts almost exactly matches the ACPF solution, accurately reflecting nodal voltages. By contrast, the classic DCPF model's ε_V grows with network size, and in large, high R/X systems it can even cause voltage regulation strategies to fail.

2. **Active power flow error comparison**
   In terms of the mean absolute branch active-power error, DLPF also consistently outperforms DCPF. In networks up to 300 buses DLPF keeps ε_P under 0.10 p.u. and even in larger systems its ε_P remains lower than that of DCPF, meeting the accuracy demands of standard stability and load flow analyses. On the other hand, DCPF shows much larger ε_P in these same networks, potentially resulting in branch overload misjudgments or misleading economic dispatch decisions.

Overall, DLPF shows high consistency on both voltage and power metrics across a wide range of meshed transmission systems. Although DCPF requires less computation, it suffers an obvious deficit in voltage accuracy prediction for large-scale networks. Therefore, for engineering applications that require extensive, high-precision iterative analyses, such as planning optimization and real-time load flow monitoring, it is recommended to employ the DLPF model to achieve more reliable and efficient operation.

3.3. Computational Efficiency for Large Scale Systems

In the context of computational efficiency for large-scale power systems, the three power-flow algorithms ACPF, DCPF and DLPF are commonly applied. Each of these algorithms has its own strengths and weaknesses, and thus a compromise must be made between numerical accuracy and solution speed. Some of these algorithms achieve high precision but require substantial computation time and therefore run relatively slowly, while others prioritize rapid execution at the expense of accuracy.
ACPF is capable of achieving the highest accuracy in voltage magnitude and phase angle profiles. However, each iteration requires reconstruction and factorization of the sparse

Jacobian matrix, making it unsuitable for real-time simulation when faced with large-scale networks.
DCPF is based on linear approximations of reactive power and line resistance to express the active power flow equations. This method produces a sparse linear system that can be solved with a single matrix factorization. As a result, it achieves extremely high computational speed in large-scale systems, enabling power flow analysis for a large number of buses in a very short time. However, it neglects the modeling of reactive power flows and voltage magnitude variations.
In DLPF, all coefficient matrices are generated directly from the network topology and match the structure of the admittance matrix, allowing for rapid updates whenever the topology changes. Most of the matrices are highly sparse, so the factorization and solution are efficient. Furthermore, the computation involves only sparse matrix–vector multiplications and additions, which dramatically accelerates the method's computational speed.

Table 3.5 compares the execution times of the three power flow methods on large-scale networks(in seconds):

Test Case	t^{ACPF}	t^{DCPF}	t^{DLPF}
IEEE 300-bus	0.025	0.014	0.001
Pegase 1354-bus	0.03	0.015	0.010
Pegase 2869-bus	0.087	0.020	0.040
Pegase 8387-bus	0.16	0.037	0.352

Table 3.5: Execution Time Comparison of ACPF, DCPF and DLPF Methods on Large-scale Networks.

On small-scale networks (less than 300 buses), DLPF is most effective one, and it reduces computation time to milliseconds, making it suitable for real-time applications.
On medium-scale networks (on the order of thousands buses), the computation speed of DLPF remains faster than ACPF but begins to be outpaced by DCPF. As the number of buses increases, the sparse linear system built by DCPF requires only a single matrix factorization for efficient solution, and its performance remains nearly invariant to network scale. Meanwhile, the overall execution time of the DLPF method increases as matrix dimensions grow and inversion operations accumulate.
Large networks (thousands to tens of thousands of buses): the overall execution time of the DLPF rises incrementally, but this can be mitigated through techniques such as network partitioning, preconditioning, and parallel acceleration.

4 | Linearized Optimization Model

This chapter presents the formulation and mathematical representation of a linearized optimization model for power systems. The model is designed not only for voltage regulation but also to ensure system security and operational reliability. To facilitate understanding, the fundamental components, indices, and symbols of the model are defined. The chapter then systematically introduces the model, including the voltage control–oriented objective function, various operational constraints, and security constraints, enabling a unified optimization of power flows, bus voltages, generator outputs, and contingency scenarios. The algorithm is implemented in the proprietary GAMS [30] language and solved using CPLEX. All optimization algorithms were executed in MATLAB/MATPOWER Version 8.0.1 on a workstation equipped with an Intel i9 2.20 GHz CPU and 32 GB RAM, using MATLAB and MATPOWER version 8.0.1. CPLEX demonstrates high robustness and efficiency in handling large scale Linear Programming (LP) and Mixed Integer Linear Programming (MILP) problems, employing strategies such as the primal simplex, dual simplex, and barrier methods. Its ability to automatically select the optimal strategy makes it particularly suitable for applications including power system optimization, logistics scheduling, and portfolio management.

To fully exploit the capabilities of CPLEX, nonlinear relationships and commonly used functions must be linearized. The introduction of linearized modeling allows these nonlinear relationships to be represented by equivalent linear constraints, ensuring compatibility with CPLEX while maintaining solution accuracy. This approach not only guarantees computational feasibility but also enables complex system behaviors, such as voltage limits, contingency scenarios, and discrete control actions, to be effectively incorporated within a unified optimization framework.

4.1. Optimization Model Notation

Before presenting the mathematical formulation of the models, it is important to first clarify some indices that are frequently used within the algorithm. The models operate within a market composed of the following elements:

$\mathcal{B}$ Set of buses.

$\mathcal{L}$ Set of branches (lines and transformers).

$\mathcal{G}$ Set of buses with conventional generation.

$\mathcal{K}$ Set of all single-component outage scenarios.

4.2. Basic DLPF-MINLP Model

This section introduces the basic Decoupled Linearized Power Flow Mixed-Integer Nonlinear Programming (DLPF-MINLP) model. The objective function and constraints will be detailed step by step, laying a solid foundation for the model extensions and linearization strategies presented in the subsequent chapters.

4.2.1. Objective function

To allow flexibility in satisfying multiple potentially conflicting constraints, a slack vector $\boldsymbol{\epsilon} \in \mathbb{R}^m$ is introduced, where each component $\epsilon_i \geq 0$ corresponds to the relaxation of the i-th constraint. The modified optimization problem is formulated as:

$$\min_{\mathbf{V}_i, \boldsymbol{\epsilon}} \quad \sum_{i \in B} \left| \mathbf{V}_i - \mathbf{V}_i^{\text{ref}} \right| + \lambda^\top \boldsymbol{\epsilon} \tag{4.1}$$

$$\text{s.t.} \quad g_i(x) \leq b_i, \quad i = 1, 2, \ldots, m \,(\text{hard constraint})$$

$$g_j(x) \leq b_j + \epsilon_j, \quad j = 1, 2, \ldots, n \,(\text{soft constraint})$$

$$\boldsymbol{\epsilon} \geq \mathbf{0} \quad (\text{slack variables})$$

where:

- $\mathbf{V}_i$ denotes the voltage magnitude at bus i.
- $\mathbf{V}_i^{\text{ref}}$ represents the reference or target voltage magnitude at bus i, typically corresponding to the desired operating point or nominal value.
- $g_i(x) \leq b_i$: the i-th hard constraint, which is a strict requirement that must be satisfied, for example, maximum power limits or physical system constraints.
- $g_j(x) \leq b_j + \epsilon_j$: the j-th soft constraint, where the slack variable ϵ_j represents

the violation of the constraint. The constraint can be relaxed, but the violation is penalized in the objective function.

- ϵ_j: slack variable for the j-th constraint, indicating the level of violation of the soft constraint.
- $\boldsymbol{\epsilon}$: vector of all slack variables for the soft constraints.
- $\lambda \in \mathbb{R}^n$: penalty weight vector, assigning a cost to the violation of each soft constraint. A higher value of λ_j results in a higher penalty for violating the corresponding soft constraint.

This formulation enables selective relaxation of constraints with a tunable penalty for each individual slack variable. This formulation provides a trade-off between optimizing the original objective and maintaining constraint satisfaction.

4.2.2. Constraints

The Optimal Power Flow model aims to determine the best solution for a given objective, such as minimizing generation cost, while simultaneously satisfying a set of operational constraints. These constraints include transmission system security, generator output limits, voltage magnitude bounds, and power flow limits on transmission lines [31]. The formulation ensures that the optimal solution is not only cost-effective but also physically feasible and secure for reliable system operation. The constraints of the OPF model are presented as follows:

Power Flow Equations

In the context of Optimal Power Flow models, the Power Flow Equations are fundamental as they describe the relationship between the generation, load, and network conditions in an electrical power system. Based on the details introduced in the previous Section 2.2.1, the linearized expression of the branch MW flow is shown as below.

$$\begin{aligned} P_{ij}^{A} &= g_{ij}\left(V_i - V_j\right) - b_{ij}\left(\theta_i - \theta_j\right), \\ Q_{ij}^{A} &= -b_{ij}\left(V_i - V_j\right) - g_{ij}\left(\theta_i - \theta_j\right) \end{aligned} \tag{4.2}$$

In an OPF optimization problem, these equations are used to determine the optimal settings of generators, voltages, and other system parameters, such as transformer tap settings, to minimize operational costs or meet other objectives while satisfying all operational constraints.

Nodal Power Balance Equations

The Nodal Power Balance Equations describe the power balance relationship at each node in an electrical power system, specifically the interaction between generation, load, transmission power, and network constraints at each node. More specifically, the Nodal Power Balance Equations ensure the balance between the power input and power output at each node.

$$\begin{aligned} \sum_{i \in \mathcal{G}} P_i^{\mathrm{g}} - P_i^d &= P_i \\ \sum_{i \in \mathcal{G}} Q_i^{\mathrm{g}} - Q_i^d &= Q_i \end{aligned} \tag{4.3}$$

$$\begin{aligned} P_i &= \sum_{(i,j) \in \mathcal{L}} P_{ij}^A + \left(\sum_{j=1}^{\mathcal{B}} G_{ij} \right) V_i \qquad \forall i \in \mathcal{B} \\ Q_i &= \sum_{(i,j) \in \mathcal{L}} Q_{ij}^A - \left(\sum_{j=1}^{\mathcal{B}} B_{ij} \right) V_i \qquad \forall i \in \mathcal{B} \end{aligned} \tag{4.4}$$

Branch Flow Limits

Branch flow limits is a critical class of constraints in power system operation. They are imposed to ensure that the power flowing through each transmission line (or branch) does not exceed its physical capacity. The thermal capacity of a transmission line is determined by various factors, including its electrical characteristics, ambient temperature, conductor material, and environmental conditions. If the power exceeds the capacity limit, it may cause the transmission line to overheat, damage equipment, or even trigger system shutdowns, thereby posing a serious threat to the overall stability and safety of the power system.

Within the framework of Optimal Power Flow models,branch flow limits not only help optimize network operation but also play a crucial role in maintaining system reliability. These constraints are essential to ensure that the solutions obtained from the optimization process are practically feasible and do not result in unsafe operating conditions. Thus, considering the flow limits of each transmission line is essential for the safe and efficient operation of modern power systems.

Mathematically, branch flow limits are typically represented by requiring that the active power P_{ij}^A and reactive power Q_{ij}^A on each line satisfy:

$$\left(P_{ij}^{A}\right)^{2}+\left(Q_{ij}^{A}\right)^{2} \leq S_{ij,\max}^{2}, \quad (i,j) \in \mathcal{L} \tag{4.5}$$

where:

- $S_{ij,\max}$ represents the thermal rating (or apparent power capacity) of branch (i,j), i.e., the maximum allowable apparent power flow through the transmission line to ensure safe operation.

Generator Output Limits The generator output limits can be expressed as:

$$\begin{aligned} P_i^{g\,\min} \leq P_i^g \leq P_i^{g\,\max}, \quad i \in \mathcal{G} \\ Q_i^{g\,\min} \leq Q_i^g \leq Q_i^{g\,\max}, \quad i \in \mathcal{G} \end{aligned} \tag{4.6}$$

where P_i^g and Q_i^g denote the active and reactive power outputs of generator, respectively, and $\mathcal{G}$ represents the set of all generators in the system. These constraints ensure that generators operate within their design capacities while providing the necessary active and reactive power support to the system.

Bus Voltage Limits The bus voltage magnitude constraints are expressed as:

$$V_i^{\min} \leq V_i \leq V_i^{\max}, \quad i \in \mathcal{B} \tag{4.7}$$

where v_i denotes the voltage magnitude at bus i, and $\mathcal{B}$ is the set of all buses in the system. These constraints ensure that the voltages at all buses are maintained within their permissible limits, thereby preserving overall system stability and ensuring power quality.

The bus voltage angle constraints are expressed as:

$$-\frac{\pi}{2} \leq \theta_i \leq \frac{\pi}{2}, \quad i \in \mathcal{B} \tag{4.8}$$

where θ_i represents the voltage angle at bus i. These constraints are set to ensure numerical stability and physical feasibility in power flow calculations. Restricting bus voltage angles within the range of $-90°$ to $90°$ helps prevent divergence in iterative solution methods caused by excessively large angle differences, while ensuring the validity of linearized power flow approximations.

4.3. Linearization of the Absolute Value Function

In voltage regulation optimization problems, minimizing the absolute voltage deviation is crucial to maintaining voltage levels as close as possible to the reference value. However, the absolute value function is inherently nonlinear, posing challenges for direct incorporation into mixed-integer linear programming (MILP) formulations. Consequently, linearization techniques are employed to approximate the absolute value function, thereby facilitating model tractability and enhancing computational efficiency.
Suppose there is a variable x for which we want to minimize the absolute value $|x|$. Introduce a non-negative auxiliary variable $\beta \geq 0$, and add the following constraints:

$$\begin{cases} x \leq \beta, \\ -x \leq \beta, \end{cases} \tag{4.9}$$

Then β serves as a linear representation (an upper bound) of $|x|$, satisfying

$$\beta \geq |x|$$

Therefore, minimizing β in the optimization problem indirectly minimizes $|x|$.
The objective function (4.1) presented in the previous Section 4.7.1 contains absolute value terms $\left|\mathbf{V}_i - \mathbf{V}_i^{\text{ref}}\right|$. To address this issue, auxiliary variables α_i are introduced to linearize the absolute value function. Specifically, for each bus voltage variable $\mathbf{V}_i$, an auxiliary variable α_i is defined, subject to the following linear constraints:

$$\begin{cases} \mathbf{V}_i - \mathbf{V}_i^{\text{ref}} \leq \boldsymbol{\alpha}_i, \\ \mathbf{V}_i^{\text{ref}} - \mathbf{V}_i \leq \boldsymbol{\alpha}_i, \end{cases} \tag{4.10}$$

which ensure that α_i serves as an upper bound on the absolute voltage deviation $\left|\mathbf{V}_i - \mathbf{V}_i^{\text{ref}}\right|$. Consequently, the original nonlinear absolute value terms in the objective function can be equivalently replaced by the linear summation

$$\min_{\boldsymbol{\alpha},\boldsymbol{\epsilon}} \quad \sum_{i\in\mathcal{B}} \boldsymbol{\alpha}_i + \lambda^\top \boldsymbol{\epsilon} \tag{4.11}$$

This linearization approach preserves the linear structure of the model, thus enhancing solvability and computational efficiency.

4.4. Transformer Linearized Model

Transformers play a key role in voltage conversion, power transmission, and phase regulation, and their performance directly affects the stability and economic efficiency of the system. In the previously established model, transformer branches are represented by nonlinear voltage relationships:

$$\tilde{V}_{Tp} = te^{j\theta_s}\,\tilde{V}_{Tq} \tag{4.12}$$

where t and θ_s denote the transformer tap ratio and phase shift angle, respectively. This representation inherently introduces nonlinearities due to the complex exponential term, which complicates the optimization process.
To incorporate transformer behavior into a linear optimization framework and enhance computational efficiency, it is necessary to linearize the transformer branch model. This section focuses on deriving an equivalent linearized transformer model and providing a rigorous proof of its validity.

4.4.1. Transformer Equivalent Model and Proof

From the modeling perspective, a transformer can be regarded as a two-port network, with the primary side as the input port and the secondary side as the output port. Between the input and output ports, not only active and reactive power can be transferred, but also amplitude changes and phase shifts may occur. These characteristics need to be captured in the model. As shown in the Figure 4.1, a local power network topology with transformer connections is illustrated, including buses, transmission lines, and the transformer.

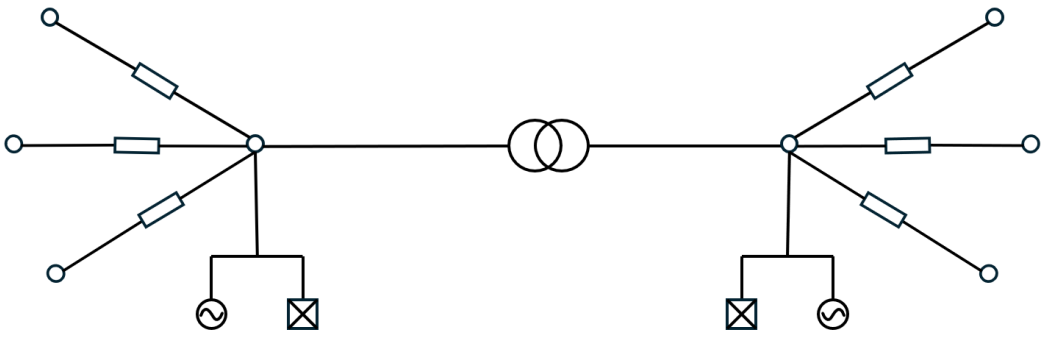

Figure 4.1: Local Power Network Topology with Transformer Connections.

To simplify the analysis, a practical transformer can be represented by an equivalent ideal transformer model with an associated impedance. The corresponding equivalent circuit is shown in Figure 4.2.

Actual Transformer $\approx Z_{T_{eq}}$ + Two-Port Model

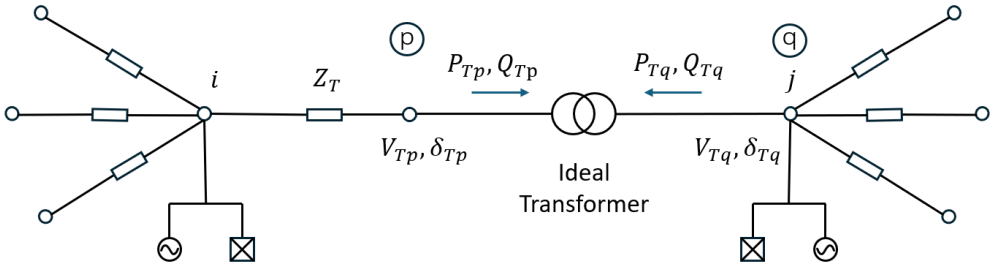

Figure 4.2: Schematic of the Transformer Equivalent Model in a Local Power Network.

where the equivalent impedance $Z_{T_{eq}}$ is used to represent the transformer's leakage impedance and winding resistance, and is expressed as:

$$Z_{T_{eq}} = R_T + jX_T \tag{4.13}$$

Here, R_T represents the winding resistance, and X_T represents the leakage reactance. In the ideal transformer model, controllable features such as a phase-shifting angle and an adjustable turns ratio are introduced to capture voltage regulation and power flow control. The voltages, currents, and power at the input and output terminals of this model must satisfy specific physical constraints. Under these constraints, the model provides an effective representation of a practical transformer with tap-changing and phase-shifting capabilities, thereby simplifying system analysis and computation. The physical constraint conditions are given as follows:

$$\begin{cases} P_{Tp} = -P_{Tq}, \\ Q_{Tp} = -Q_{Tq}, \\ V_{Tp} = t \cdot V_{Tq}, \\ \delta_{Tp} - \delta_{Tq} = \theta_s \end{cases} \tag{4.14}$$

where:

- P_{Tp}, Q_{Tp} are the active and reactive power at port p;
- P_{Tq}, Q_{Tq} are the active and reactive power at port q;
- V_{Tp}, V_{Tq} are the voltage magnitudes at port p and port q;
- δ_{Tp}, δ_{Tq} are the voltage phase angles at port p and port q;
- t is the voltage tap ratio between the two ports;
- θ_s is the transformer phase shift angle.

Although equation (4.14) models the ideal transformer(see Figure 4.2), note that the branch connecting nodes i and P is already incorporated within the admittance matrix and therefore implicitly accounted for in equations (4.3) and (4.4), avoiding redundancy in the system representation.
These physical constraints characterize the two-port relationship and ensure that the transformer can be represented by the proposed equivalent model, whose equivalence will be mathematically derived and demonstrated below.
The above physical constraints allow deriving the following relations between port p and port q:

$$\tilde{V}_{Tp} = te^{j\theta_s}\, \tilde{V}_{Tq} \tag{4.15}$$

$$\tilde{S}_{Tp} = -\tilde{S}_{Tq} \tag{4.16}$$

where the complex power is defined as

$$\tilde{S} = \tilde{V}\,\tilde{I}^{*}. \tag{4.17}$$

From the power balance constraint, it follows that:

$$\tilde{V}_{Tp}\tilde{I}^{*}_{Tp} = -\tilde{V}_{Tq}\tilde{I}^{*}_{Tq}. \tag{4.18}$$

Substituting the voltage ratio relation $\tilde{V}_{Tp} = te^{j\theta_s}\tilde{V}_{Tq}$:

$$(te^{j\theta_s}\tilde{V}_{Tq})\,\tilde{I}^{*}_{Tp} = -\tilde{V}_{Tq}\tilde{I}^{*}_{Tq}. \tag{4.19}$$

Dividing both sides by $\tilde{V}_{Tq} \neq 0$:

$$te^{j\theta_s}\tilde{I}^*_{Tp} = -\tilde{I}^*_{Tq}. \tag{4.20}$$

Thus, the voltage and current relations across the two ports of the model:

$$t\,e^{j\theta_s} = \frac{V_{Tp}}{V_{Tq}} = \frac{I_{Tq}}{I_{Tp}} \tag{4.21}$$

The voltage and current relationships of this two-port model comply with the transformer turns ratio, thereby validating the correctness of the equivalent model.

4.4.2. Linearization of Transformer Model Constraints

Equation (4.14) defines the equivalent idea transformer model constraints, including active and reactive power balances, as well as voltage and angle relationships. Specifically:

$$\begin{aligned} P_{Tp} &= -P_{Tq}, \\ Q_{Tp} &= -Q_{Tq}, \\ V_{Tp} &= t \cdot V_{Tq}, \\ \delta_{Tp} - \delta_{Tq} &= \theta_s \end{aligned}$$

- The first constraint $P_{Tp} = -P_{Tq}$ and the second constraint $Q_{Tp} = -Q_{Tq}$ represent power balance constraints. They are linear and can thus be directly used in optimization model.
- The fourth constraint $\delta_{Tp} - \delta_{Tq} = \theta_s$ is also linear, describing a angle difference between the two ports.
- The third constraint $V_{Tp} = t \cdot V_{Tq}$ is nonlinear, since both the tap ratio and the voltage are decision variables, and their product introduces nonlinearity. To ensure the model remains linear and solvable in practical optimization, this constraint must be linearized so that it can be directly handled by optimization solvers.

Accordingly, the linearization of the constraint $V_{Tp} = t \cdot V_{Tq}$ can be formulated as follows:

Note that V_{Tp} and V_{Tq} can be expressed as 1 plus a small deviation, where $|\Delta V_{Tp}| \ll 1$ and $|\Delta V_{Tq}| \ll 1$.

$$\begin{aligned} V_{Tp} &= 1 + \Delta V_{Tp} \\ V_{Tq} &= 1 + \Delta V_{Tq} \end{aligned} \tag{4.22}$$

Substituting into the original constraint $V_{Tp} = t \cdot V_{Tq}$ yields

$$1 + \Delta V_{Tp} = t\,(1 + \Delta V_{Tq}) \tag{4.23}$$

This gives

$$t = \frac{1 + \Delta V_{Tp}}{1 + \Delta V_{Tq}} \tag{4.24}$$

Multiplying the numerator and denominator by $1 - \Delta V_{Tq}$ results in

$$\begin{aligned} t &= \frac{(1 + \Delta V_{Tp})(1 - \Delta V_{Tq})}{1 - (\Delta V_{Tq})^2} \\ &= \frac{1 + \Delta V_{Tp} - \Delta V_{Tq} - \Delta V_{Tp}\Delta V_{Tq}}{1 - (\Delta V_{Tq})^2} \end{aligned} \tag{4.25}$$

Applying the same linearization approximation as in Section 2.2.1, and equation (2.9), which neglects higher-order terms, the expression can be further simplified to

$$t \approx 1 + \Delta V_{Tp} - \Delta V_{Tq}. \tag{4.26}$$

Therefore, subtracting 1 from both sides yields

$$1 + \Delta V_{Tp} - 1 - \Delta V_{Tq} \approx t - 1 \tag{4.27}$$

Finally, the result can be written as

$$V_{Tp} - V_{Tq} \approx t - 1 \tag{4.28}$$

or equivalently,

$$V_{Tp} \approx t + V_{Tq} - 1 \tag{4.29}$$

Therefore, the original constraint $V_{Tp} = t \cdot V_{Tq}$ can be linearized as

$$V_{Tp} = t + V_{Tq} - 1, \tag{4.30}$$

which provides a simple linear relationship between V_{Tp}, V_{Tq}, and t.

To assess the accuracy of the linearization approach, the operating condition with the transformer secondary voltage fixed at 0.9 pu is selected. The errors between the linearized approximation and the original nonlinear expression are then computed and compared across varying values of the transformer tap ratio t. Figure 4.3 illustrates the comparison between the linearized results and the true nonlinear values.

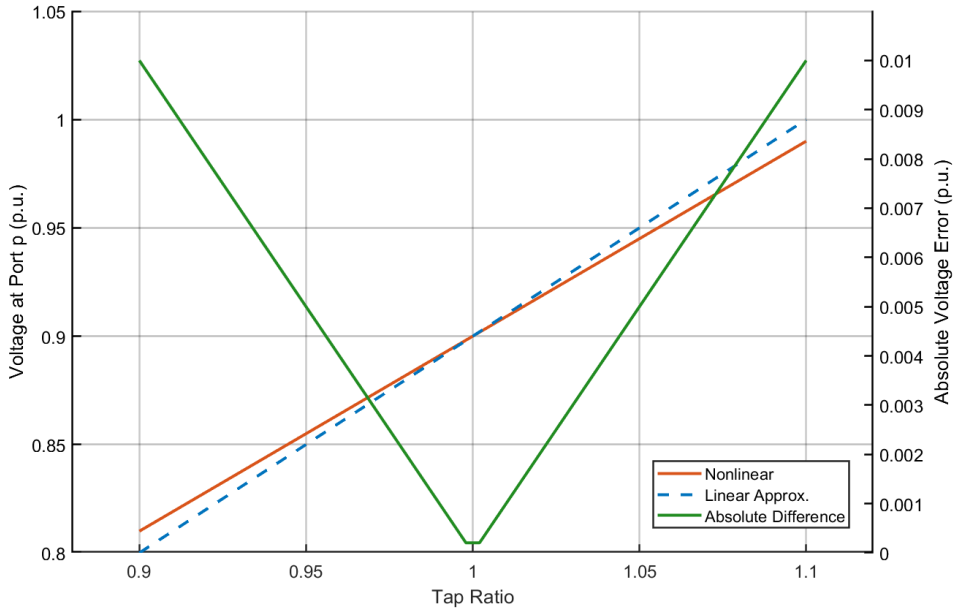

Figure 4.3: Comparison Between Linearized and Actual Nonlinear Transformer Voltage Constraint ($V_{Tq} = 0.9$ pu).

The results indicate that within the adjustable range of the transformer tap ratio t (typically $\pm 10\%$ around the nominal value), the maximum absolute error between the linearized expression and the actual value remains below 0.01 pu. This demonstrates that the proposed linearization method achieves high approximation accuracy within practical operating conditions, effectively meeting the requirements for voltage regulation and optimization control.

4.5. Linearized Modeling of Shunt Elements

In power systems, shunt elements such as capacitors or reactors can absorb or supply reactive power. The reactive power absorbed by a shunt susceptance can be expressed as:

$$Q_{sh,i} = B_i V_i^2, \quad i \in \mathcal{B}_{sh} \tag{4.31}$$

where:

- $Q_{sh,i}$ is the shunt reactive power injection at bus i;
- B_i is the shunt susceptance of the reactive power compensation device at bus i;
- $\mathcal{B}_{sh}$ is the set of buses equipped with shunt compensation devices.

The quadratic term V_i^2 introduces nonlinearity, which increases the computational difficulty in optimization problems. Therefore, it is desirable to apply a linearization approximation for efficient optimization.

4.5.1. Linearization of Shunt Branch

Assuming that the bus voltage V deviates slightly from the per-unit value of 1, it can be written as:

$$V = 1 + \Delta V \tag{4.32}$$

Then,

$$V^2 = (1 + \Delta V)^2 \tag{4.33}$$

$$= 1 + 2\Delta V + (\Delta V)^2 \tag{4.34}$$

Neglecting the higher-order term $(\Delta V)^2$, the linear approximation becomes:

$$\begin{aligned} V^2 &= (1 + \Delta V)(1 + \Delta V) \\ &= 1 + \Delta V + \Delta V + (\Delta V)^2 \\ &\approx 1 + \Delta V + \Delta V \\ &= 1 + (V - 1) + (V - 1) \\ &= 2V - 1 \end{aligned} \tag{4.35}$$

Using this approximation, the reactive power expression can be further simplified into a linear form.

To validate the accuracy of the proposed linear approximation, here compares the linearized expression of the voltage square, $2V - 1$, with its actual nonlinear value, V^2, across a range of voltage levels which is shown in the Figure 4.4.

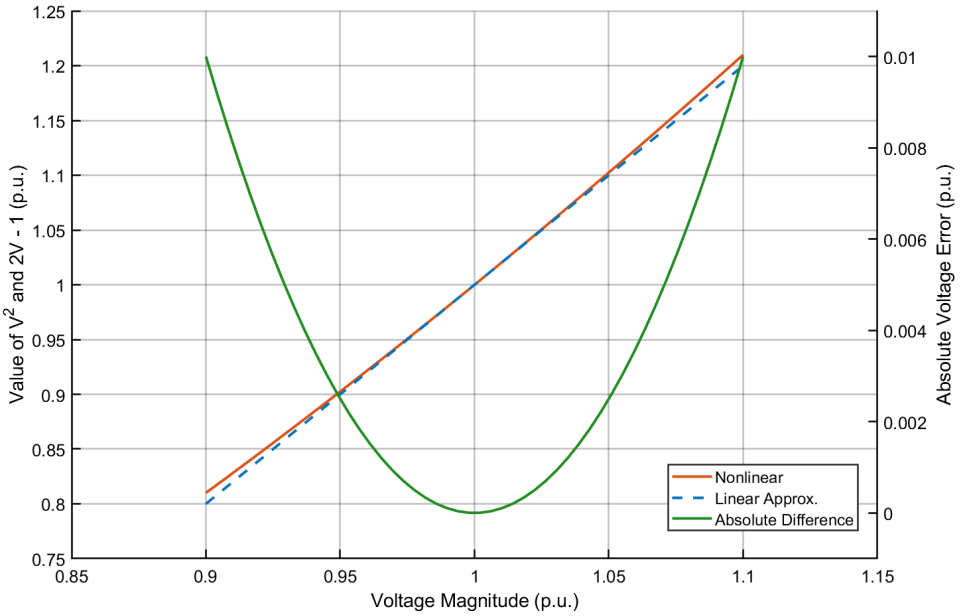

Figure 4.4: Comparison of Linearized and Nonlinear Voltage-Squared Relationships.

Within the voltage range $0.9 \leq V \leq 1.1$ pu, the maximum absolute error between the two remains below 0.01 pu. These results demonstrate that the proposed linearization method effectively approximates the nonlinear behavior of the voltage square within acceptable error margins, offering high accuracy and practical applicability for power system analysis and optimization control.

4.5.2. Binary Switching Variable

In practice, shunt devices can be switched ON or OFF. To model this discrete operation in an optimization problem, a binary variable z is introduced:

$$z_i = \begin{cases} 1, & \text{if the shunt element is connected (ON),} \\ 0, & \text{if the shunt element is disconnected (OFF).} \end{cases} \tag{4.36}$$

Then, the reactive power can be expressed as:

$$Q_{sh,i} = z_i B_i V_i^2 \tag{4.37}$$

Applying the linearization $V_i^2 \approx 2V_i - 1$, the reactive power becomes:

$$\begin{aligned} Q_{sh,i} &\approx z_i B_i (2V_i - 1) \\ &= -B_i z_i + 2B_i z_i V_i. \end{aligned} \tag{4.38}$$

The primary purpose of introducing the binary variable z_i is to accurately model the switching status of shunt devices. Without z_i, the model would implicitly assume that the branch is always connected, which could lead to unrealistic or infeasible reactive power calculations. By including z_i, the optimization can determine whether the device should be connected or disconnected, thereby capturing the discrete nature of shunt operations while maintaining a linearized formulation.

Here, z_i is a binary variable and V_i is continuous, which results in a mixed-integer linear programming (MILP) formulation that can be directly incorporated into optimization problems. In other words, z_i enables the integration of ON/OFF switching decisions into the linearized reactive power model, ensuring that the optimization outcomes are both feasible and closer to actual system operation.

4.5.3. Multiplication of Binary and Continuous Variables

In many optimization models, interactions between binary and continuous variables give rise to bilinear terms. These terms are inherently nonlinear because they involve the product of two variables. Therefore, such bilinear terms must be linearized to preserve the linearity of the model and to ensure compatibility with compatible with solvers like CPLEX. Let x_i denote a binary decision variable for each $i \in \{1, \ldots, m\}$, and let y_j represent a continuous variable bounded within the interval $0 \leq y_j \leq u_j$ for each $j \in \{1, \ldots, n\}$. The bilinear term $x_i \cdot y_j$ is linearized without approximation by introducing an auxiliary variable z_{ij} to represent the product [32]. The relationship $z_{ij} = x_i \cdot y_j$ is enforced via the following linear constraints:

$$\begin{cases} z_{ij} \leq y_j, \\ z_{ij} \leq u_j x_i, \\ z_{ij} \geq y_j + u_j(x_i - 1), \\ z_{ij} \geq 0, \end{cases} \quad \forall i = 1, \ldots, m, \quad \forall j = 1, \ldots, n. \tag{4.39a}$$

Here, u is a known upper bound on y_j. The constraints ensure that $z_{ij} = 0$ when $x_i = 0$ and $z_{ij} = y_j$ when $x_i = 1$, as shown in Table 4.1.

x	y	$x \cdot y$	**Constraints**	**Implied**
0	$t : 0 \leq t \leq u$	0	$z \leq t$ $z \leq 0$ $z \geq t - u$ $z \geq 0$	$z = 0$
1	$t : 0 \leq t \leq u$	t	$z \leq t$ $z \leq u$ $z \geq t$ $z \geq 0$	$z = t$

Table 4.1: All possible products of binary and continuous variables ($z := x \cdot y$).

4.6. Piecewise linearization of Branch Flow Limits

Constraint (4.5) is a quadratic constraint. If introduced directly, the resulting OPF model will be transformed into a convex quadratically constrained optimization problem. However, solving quadratically constrained problems is numerically less stable than solving linearly constrained ones, particularly in the case of large-scale models [33].
Constraint (4.5) can be handled using a piecewise linearization method, as illustrated in Figure 4.5. The feasible region defined by the branch flow constraint forms a circle. In this figure, the horizontal and vertical axes represent the reactive and active power flows of branch (i, j), respectively, and Constraint (4.5) corresponds to the interior of the circular region. This circular region can be approximated by a set of straight lines (shown in red), forming a polygonal region and thereby enabling a piecewise linear representation of the original quadratic constraint.

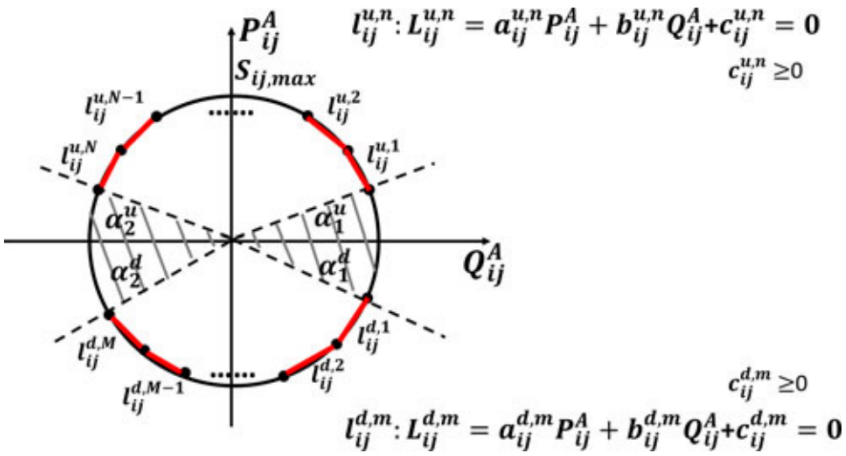

Figure 4.5: Linearization Approach for Quadratic Branch Flow Constraints [34].

The specific procedure is as follows:

1. **Parameter selection:** Set the parameters $\alpha_1^u, \alpha_2^u, \alpha_1^d, \alpha_2^d$ and the number of segments M and N. In the paper, for all branches,$\alpha_1^u = \alpha_2^u = \alpha_1^d = \alpha_2^d = \frac{\pi}{6}$, and $M = N = 20$.

2. **Arc division:** Divide the circular arc $[\alpha_1^u, \pi - \alpha_2^u]$ into N equal segments and connect the adjacent endpoints to obtain N straight lines. Similarly, divide the arc $[\pi + \alpha_1^d, 2\pi - \alpha_2^d]$ into M equal segments to obtain M straight lines.

3. **Linear constraint construction:** Use the $M + N$ straight lines to form linear constraints that approximate the original quadratic constraint (as in Constraint (4.5)), resulting in a set of linear inequalities that can be directly used in OPF solving.

The method focuses the linearization only on the arc segments where branch flows are most likely to occur, while ignoring regions of low probability (the shaded area represents regions where the system operating point rarely appears). Accordingly, the branch flow restriction in (4.5) can be expressed through the following linear constraints:

$$\begin{aligned} L_{ij}^{u,n} &\geq 0, \quad n = 1, \ldots, N, \quad (i,j) \in \mathcal{L} \\ L_{ij}^{d,m} &\geq 0, \quad m = 1, \ldots, M, \quad (i,j) \in \mathcal{L} \end{aligned} \tag{4.40}$$

This significantly reduces the number of required linear constraints. Therefore, the piecewise linearization method can reduce the number of constraints while maintaining approximation accuracy, thus improving computational efficiency.

4.7. Comprehensive DLPF-MILP Model for Voltage Regulation Optimization

Based on the linearization techniques presented earlier, the resulting Decoupled Linearized Power Flow Mixed-Integer Linear Programming (DLPF-MILP) model integrates the original nonlinear formulation with the corresponding linear approximations. The following section elaborates the mathematical expressions and constraints of the model, providing a comprehensive mathematical description of the voltage regulation optimization model.

4.7.1. Objective function

$$
\begin{aligned}
\min_{\boldsymbol{\alpha},\boldsymbol{\epsilon}} \quad & \sum_{i\in B} \boldsymbol{\alpha}_i + \lambda^\top \boldsymbol{\epsilon} \\
\text{s.t.} \quad & \mathbf{V}_i - \mathbf{V}_i^{\text{ref}} \le \boldsymbol{\alpha}_i, \\
& \mathbf{V}_i^{\text{ref}} - \mathbf{V}_i \le \boldsymbol{\alpha}_i, \\
& g_i(x) \le b_i, \quad i = 1, \ldots, m \quad \text{(hard constraints)}, \\
& g_j(x) \le b_j + \epsilon_j, \quad j = 1, \ldots, n \quad \text{(soft constraints)}, \\
& \boldsymbol{\epsilon} \ge \mathbf{0}, \quad \boldsymbol{\alpha} \ge \mathbf{0}.
\end{aligned}
\tag{4.41}
$$

where:

- $\mathbf{V}_i$ denotes the voltage magnitude at bus i.
- $\mathbf{V}_i^{\text{ref}}$ represents the reference or target voltage magnitude at bus i, typically corresponding to the desired operating point or nominal value.
- $\boldsymbol{\alpha}_i$: auxiliary variables introduced to linearize the absolute value of voltage deviation $|\mathbf{V}_i - \mathbf{V}_i^{\text{ref}}|$, ensuring $\boldsymbol{\alpha}_i \ge |\mathbf{V}_i - \mathbf{V}_i^{\text{ref}}|$.

4.7.2. Nodal Power Balance Equations

The linearized expression of the branch MW flow is shown as below.

$$
\begin{aligned}
P_{ij}^A &= g_{ij}\left(V_i - V_j\right) - b_{ij}\left(\theta_i - \theta_j\right), \\
Q_{ij}^A &= -b_{ij}\left(V_i - V_j\right) - g_{ij}\left(\theta_i - \theta_j\right)
\end{aligned}
\tag{4.42}
$$

The Nodal Power Balance Equations are

$$\begin{aligned} \sum_{i \in \mathcal{G}} P_i^{\mathrm{g}} - P_i^d &= P_i \\ \sum_{i \in \mathcal{G}} Q_i^{\mathrm{g}} - Q_i^d &= Q_i \end{aligned} \tag{4.43}$$

$$\begin{aligned} P_i &= \sum_{(i,j) \in \mathcal{L}} P_{ij}^A + \left(\sum_{j=1}^{\mathcal{B}} G_{ij} \right) V_i \qquad \forall i \in \mathcal{B} \\ Q_i &= \sum_{(i,j) \in \mathcal{L}} Q_{ij}^A - \left(\sum_{j=1}^{\mathcal{B}} B_{ij} \right) V_i \qquad \forall i \in \mathcal{B} \end{aligned} \tag{4.44}$$

4.7.3. Branch Flow Limits

The piecewise linearization of branch flow limits are

$$\begin{aligned} L_{ij}^{u,n} &= a_{ij}^{u,n} P_{ij}^A + b_{ij}^{u,n} Q_{ij}^A + c_{ij}^{u,n}, \\ L_{ij}^{d,m} &= a_{ij}^{d,m} P_{ij}^A + b_{ij}^{d,m} Q_{ij}^A + c_{ij}^{d,m} \end{aligned} \tag{4.45}$$

where $L_{ij}^{u,n}$ and $L_{ij}^{d,m}$ denote the n-th and m-th segments of the piecewise linear functions for the upper and lower limits, respectively; $a_{ij}^{\cdot}$, $b_{ij}^{\cdot}$, and $c_{ij}^{\cdot}$ are the coefficients of the linear functions.

To ensure that the branch flows remain within permissible bounds, the following inequality constraints must be satisfied:

$$\begin{aligned} L_{ij}^{u,n} &\geq 0, \quad n = 1, \ldots, N, \quad (i,j) \in \mathcal{L} \\ L_{ij}^{d,m} &\geq 0, \quad m = 1, \ldots, M, \quad (i,j) \in \mathcal{L} \end{aligned} \tag{4.46}$$

where N and M are the number of segments for the upper and lower limits, respectively.

4.7.4. Linearized Constraints of Transformers

The following equations represent the physical constraint conditions of transformer :

$$\begin{cases} P_{Tp} = -P_{Tq}, \\ Q_{Tp} = -Q_{Tq}, \\ V_{Tp} = t + V_{Tq} - 1, \\ \delta_{Tp} - \delta_{Tq} = \theta_s \end{cases} \tag{4.47}$$

The constraints of transformer tap ratio t can be expressed as:

$$t_{\min} \leq t \leq t_{\max}, \qquad t_{\min} = 0.9,\ t_{\max} = 1.1 \tag{4.48}$$

where t denotes the transformer tap ratio. This range ensures that the transformer can adjust the bus voltage within $\pm 10\%$ [35], meeting system voltage control requirements while guaranteeing safe operation of the equipment. Within this range, the relationship between bus voltage and tap ratio can be approximated as linear, facilitating fast voltage regulation optimization.

The constraints of the phase shifter angle θ_{T} can be expressed as:

$$\theta_{\min} \leq \theta_s \leq \theta_{\max}, \qquad \theta_{\min} = -0.2,\ \theta_{\max} = 0.2 \tag{4.49}$$

This range corresponds approximately to $\pm 11.5^\circ$ [36], which ensures the validity of the linear approximation $\sin(\theta_s) \approx \theta_s$, allowing the effect of the phase shifter on branch power flows to be directly incorporated into the linearized power flow model.
Applying these linearized constraints to transformers and phase shifters preserves model accuracy and computational efficiency, allowing rapid voltage regulation and reliable control in large-scale power systems.

Linearized Constraints of Tap Staggering In a Tap Staggering operation, the tap positions of a pair of parallel transformers, T_1 and T_2, are adjusted in opposite directions to form a staggered tap pattern, as illustrated in the Figure 1.1 in Section 1.4.2. Specifically, the tap of T_1 is decreased by k steps, denoted as Δt_a, while the tap of T_2 is increased by k steps, denoted as Δt_b. This operation ensures that the tap changes are equal in magnitude but opposite in direction:

$$\Delta t_a = -\Delta t_b \tag{4.50}$$

As a result, the sum of the tap positions of the two transformers remains constant:

$$t_a + t_b = t_{a,0} + t_{b,0} \equiv \text{constant} \tag{4.51}$$

where the adjusted tap positions are given by

$$t_a = t_{a,0} - \Delta t_a, \quad t_b = t_{b,0} - \Delta t_b \tag{4.52}$$

where:

- T_1, T_2: the parallel transformers involved in the Tap Staggering operation.
- t_a, t_b: adjusted tap ratios of T_1 and T_2, respectively.
- $t_{a,0}, t_{b,0}$: initial tap ratios of T_1 and T_2 (commonly set to 1 as reference).
- $\Delta t_a, \Delta t_b$: tap changes relative to the initial positions.

This linear relationship ensures a balanced staggered tap configuration for the transformer pair and can be generalized to any number of parallel transformer pairs in the system. And this formulation is compact and convenient for direct use in power flow optimization and control models.

4.7.5. Linearized Constraints of Shunt Element

Given the approximation:

$$Q_{sh,i} \approx z_i B_i (2V_i - 1) = -B_i z_i + 2B_i z_i V_i. \tag{4.53}$$

where $z_i \in \{0, 1\}$ is a binary variable representing the switch status, V_i is a continuous variable bounded by $V_i^{\min} \leq V_i \leq V_i^{\max}$, and B_i is a constant.

Introduce an auxiliary variable:

$$w_i = z_i \cdot V_i, \tag{4.54}$$

Then, $Q_{sh,i}$ can be expressed as the linear function:

$$Q_{sh,i} = -B_i z_i + 2B_i w_i. \tag{4.55}$$

The linearized constraints for the product term $w_i = z_i V_i$ are given by:

$$\begin{cases} w_i \leq V_i, \\ w_i \leq V_i^{\max} z_i, \\ w_i \geq V_i - V_i^{\max}(1 - z_i), \\ w_i \geq 0, \\ z_i \in \{0, 1\} \end{cases} \tag{4.56}$$

4.7.6. Operational Constraints

Generator Output Limits The generator output limits can be expressed as:

$$\begin{aligned} P_i^{g\,\min} \leq P_i^g \leq P_i^{g\,\max}, \quad i \in \mathcal{G} \\ Q_i^{g\,\min} \leq Q_i^g \leq Q_i^{g\,\max}, \quad i \in \mathcal{G} \end{aligned} \tag{4.57}$$

Bus Voltage Limits The bus voltage magnitude constraints are expressed as:

$$V_i^{\min} \leq V_i \leq V_i^{\max}, \quad i \in \mathcal{B} \tag{4.58}$$

The bus voltage angle constraints are expressed as:

$$-\frac{\pi}{2} \leq \theta_i \leq \frac{\pi}{2}, \quad i \in \mathcal{B} \tag{4.59}$$

where θ_i represents the voltage angle at bus i. These constraints are set to ensure numerical stability and physical feasibility in power flow calculations. Restricting bus voltage angles within the range of $-90°$ to $90°$ helps prevent divergence in iterative solution methods caused by excessively large angle differences, while ensuring the validity of linearized power flow approximations.

4.7.7. N-1 Security Constraints

The N-1 security constraint is a principal reliability requirement in power system operation and planning, ensuring that the system continues to operate safely and supply electricity without interruption under any single component failure, including the outage

of transmission lines, transformers, or generators. This constraint is critical to maintaining system-wide stability and preventing widespread disruptions or equipment damage.

Theoretically, the N-1 security constraint is typically represented as a set of additional power flow constraints. Specifically, under the condition of a single component failure in the system, the node voltages, currents, and power flows must still satisfy operational limits [37]. For instance, in voltage optimization problems, the N-1 security constraint requires that for every potential fault scenario, all node voltages remain within the allowable safe range, and all branch power flows do not exceed their rated capacities.

Let $k \in \mathcal{K}$ denote all possible single-component fault scenarios. The N-1 security constraints can be formalized as follows:

$$V_i^{\min} \leq V_i^k \leq V_i^{\max}, \quad \forall i \in \mathcal{B},\ \forall k \in \mathcal{K} \tag{4.60}$$

$$|S_{ij}^{A,k}| \leq S_{ij}^{\max}, \quad \forall (i,j) \in \mathcal{L},\ \forall k \in \mathcal{K} \tag{4.61}$$

where V_i^k and $S_{ij}^{A,k}$ represent the bus voltage and branch power flow under the k-th fault scenario, respectively. These constraints ensure that the system operates safely under any single-component failure, preventing voltage violations or branch overloads.

Similarly, other operational constraints, such as bus voltage limits, branch flow limits, and generator output limits, can also be defined under the N-1 security framework to guarantee safe and stable system operation in the presence of any single-component outage.

5 | Case Studies and Simulation Results

This chapter will first present a comparative analysis of different voltage regulation methods through representative case studies. The evaluation focuses on voltage profile optimization, reactive power allocation and illustrates the regulation capabilities of different voltage control strategies. An N-1 security analysis is then performed to evaluate the model's voltage regulation performance and system adaptability under contingencies where a single component, such as a transmission line or transformer, is out of service. This analysis provides a rigorous evaluation of the model's effectiveness and robustness under typical power system security constraints, thereby demonstrating its practical value in maintaining stable operation and ensuring voltage security in large scale systems.
Meanwhile, simulation results indicate that the proposed algorithm exhibits excellent computational efficiency. With the support of the linearized modeling framework, the solution speed and stability are greatly improved. For systems with up to approximately 1,000 buses, the total computation time is typically below 0.5 seconds. For larger networks of around one thousand buses, the solution is usually obtained within 0.5 to 2 seconds, fully verifying the efficiency and practicality of the proposed linearized optimization model.

5.1. Evaluation Metrics for Control Parameters

When analyzing the impact of controllable parameters (e.g., transformer tap ratio, phase shift angle) on bus voltages, it is necessary to define the bus voltages before and after the adjustment of these parameters.
Let $V_{i,\text{before}}$ denote the voltage at bus i before a controllable parameter is adjusted, i.e., the original voltage under the current operating condition. Similarly, $V_{i,\text{after}}$ represents the voltage at bus i after the adjustment has been applied, i.e., the resulting voltage after the parameter change. The following parameters are used for assessment:
The first metric is the voltage change at bus i, which quantifies the absolute change in voltage resulting from the adjustment of a controllable parameter. It is defined as

$$\Delta V_i = V_{i,\text{after}} - V_{i,\text{before}} \tag{5.1}$$

The second metric is the relative voltage change, which quantifies the magnitude of the voltage variation at bus i relative to its original value and provides a measure of the effectiveness of the adjustment of a controllable parameter. It is defined as

$$\Delta V_i^{\text{rate}} = \left| \frac{V_{i,\text{after}} - V_{i,\text{before}}}{V_{i,\text{before}}} \right| = \frac{|\Delta V_i|}{V_{i,\text{before}}} \tag{5.2}$$

The third index employed to evaluate voltage regulation is the voltage sensitivity to a controllable parameter, which characterizes how responsive the bus voltage at bus i is to adjustments in that parameter, i.e., the amount of voltage change per unit change of the parameter. This can refer to the transformer tap ratio or the phase shift angle. It is defined as

$$S_{V_i,p} = \left| \frac{V_{i,\text{after}} - V_{i,\text{before}}}{\Delta p} \right| = \frac{|\Delta V_i|}{\Delta p} \tag{5.3}$$

where Δp represents the change in the controllable parameter (e.g., tap ratio or phase shift angle).

5.2. Voltage Regulation Capability of Transformer Tap Ratio Adjustment

Transformer tap ratio adjustment is a fundamental voltage regulation method, and its impact differs under meshed transmission networks and radial distribution networks. In this section, simulation studies are carried out to evaluate its voltage regulation capability in both network topologies.

5.2.1. Radial Network Case of Tap Ratio Adjustment

22-bus test network is a typical distribution system with a radial topology. The case includes no additional voltage support or reactive power compensation such as capacitor banks, reactors or generator-based devices (e.g., synchronous condensers), and the generators' active and reactive power outputs are kept fixed. A transformer connects bus 13 and bus 14 along a radial branch, which can be adjusted via tap changers depending on the

simulation scenario and serves as an interface to downstream distribution feeders. This network is used to illustrate the impact of transformer tap adjustments on bus voltages in a simple radial feeder and distribution context. The corresponding bus and tap ratio data for this network are summarized in Table 5.1.

BUS	**Tap ratio t=1**	**Tap Ratio t [±5%]**			**Tap Ratio t [±10%]**		
	V_i **(p.u.)**	ΔV_i	$\Delta V_i^{\mathbf{rate}}$	$S_{V_i,t}$	ΔV_i	$\Delta V_i^{\mathbf{rate}}$	$S_{V_i,t}$
1	1.0000	0	0	0	0	0	0
2	0.9970	0	0	0	0	0	0
3	0.9970	0	0	0	0	0	0
4	0.9928	0	0	0	0	0	0
5	0.9927	0	0	0	0	0	0
6	0.9920	0	0	0	0	0	0
7	0.9920	0	0	0	0	0	0
8	0.9920	0	0	0	0	0	0
9	0.9878	0	0	0	0	0	0
10	0.9878	0	0	0	0	0	0
11	0.9835	0	0	0	0	0	0
12	0.9835	0	0	0	0	0	0
13	0.9812	0	0	0	0	0	0
14	0.9762	0.05	5.12%	100.00%	0.1	10.24%	100.00%
15	0.9762	0.05	5.12%	100.00%	0.1	10.24%	100.00%
16	0.9759	0.05	5.12%	100.00%	0.1	10.25%	100.00%
17	0.9750	0.05	5.12%	100.00%	0.1	10.26%	100.00%
18	0.9749	0.05	5.13%	100.00%	0.1	10.26%	100.00%
19	0.9739	0.05	5.13%	100.00%	0.1	10.27%	100.00%
20	0.9737	0.05	5.13%	100.00%	0.1	10.27%	100.00%
21	0.9737	0.05	5.14%	100.00%	0.1	10.27%	100.00%
22	0.9735	0.05	5.14%	100.00%	0.1	10.27%	100.00%

Table 5.1: Buss voltages and results under different phase shift angle tolerances in radial network.

The electrical distance D_i from each bus to the secondary side of the transformer at Bus 14 is calculated based on the branch impedances along the shortest path from that bus to Bus 14. For each branch $i-j$ along the path, the branch impedance is given by $r_{ij}+jx_{ij}$, where r_{ij} and x_{ij} denote the resistance and reactance of the branch, respectively. The

total electrical distance of bus i is defined as the square root of the sum of squared branch impedance along the path:

$$D_i = \sqrt{\sum_{\text{path } i \to 14} \left(r_{ij}^2 + x_{ij}^2\right)} \tag{5.4}$$

This metric reflects the relative "electrical proximity" of each bus to the secondary side of the transformer at Bus 14, which is shown in Table 5.2. Smaller values indicate a more direct or electrically closer connection. This method considers the cumulative effect of line impedances on voltage, thus providing a reasonable representation of the bus's electrical location in the network.

BUS	**Distance to Bus 14**
1	0.034984
2	0.031608
3	0.032116
4	0.026573
5	0.028366
6	0.040553
7	0.041109
8	0.043253
9	0.019665
10	0.020174
11	0.013389
12	0.013897
13	0.009724
14	0.000000
15	0.000206
16	0.000509
17	0.003494
18	0.004376
19	0.008831
20	0.010030
21	0.010841
22	0.014984

Table 5.2: Electrical distances of each bus to the transformer secondary Side at Bus 14.

As observed in the previous table, the voltage responses of individual buses along the network exhibit certain patterns under different tap ratio adjustments. To further illustrate these variations, the following figure presents the voltage responses of all buses, including the relative voltage change and the voltage sensitivity to the tap position. Buses are arranged by electrical distance from the transformer at Bus 14, illustrating the variations in voltage response and sensitivity across the network.

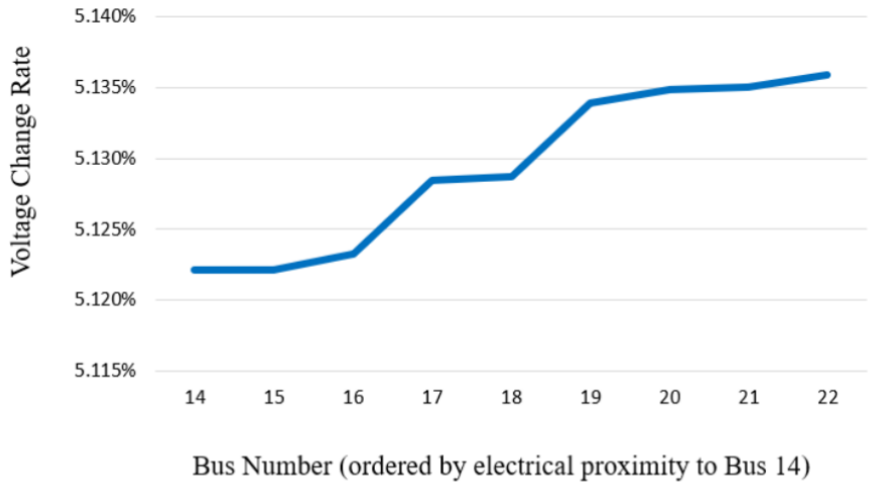

Figure 5.1: Bus Voltage Response under Tap Ratio Adjustment (t±5%)

Note: Bus numbers are ordered by electrical distance from near to far relative to the transformer secondary side (Bus 14).

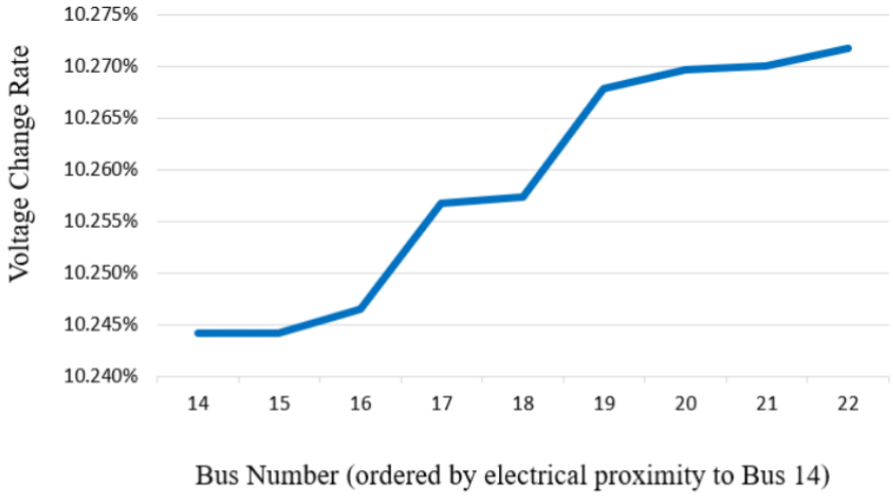

Figure 5.2: Bus Voltage Response under Tap Ratio Adjustment (t±10%)

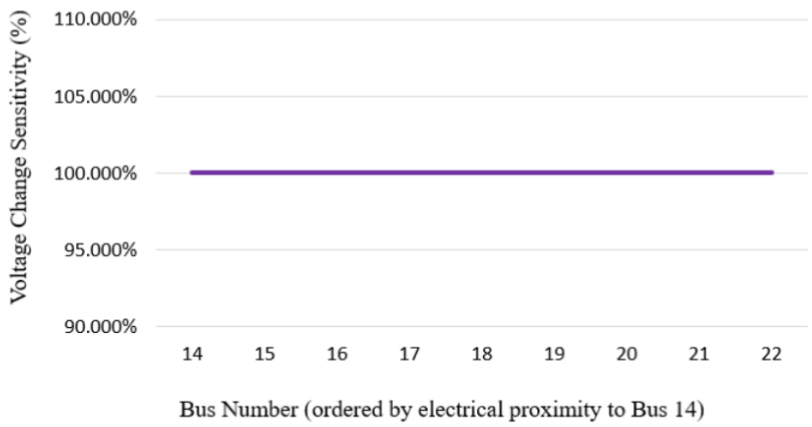

Figure 5.3: Sensitivity of Bus Voltages to Tap Ratio Adjustment (t±5%, t±10%)

Based on the bus voltage change rates and sensitivity data presented above, further analysis can be conducted to examine the impact of tap ratio adjustments on different buses, leading to the following observations:

1. Impact of Tap Changers on Distribution Network Voltage

   - Secondary Voltage Control: The secondary voltage of the transformer is controlled by the tap ratio, and its adjustment propagates along the radial network, affecting the voltage levels across the entire secondary side. While the primary voltage is determined by the upstream grid and is not influenced by tap changer adjustments.
   - Voltage Drop Characteristics: The voltage increase at buses close to the transformer is almost equal to the tap changer adjustment. However, due to the voltage drop along the radial lines caused by line impedance and load currents, the relative voltage change (ΔV_i^{rate}) at distant buses becomes larger.
   - Adjustment Limits: Excessive tap changer adjustments may lead to overvoltage at nearby buses, potentially causing voltage violations. Therefore, a balance must be maintained between overall network voltage compliance and local voltage deviations.

2. Application Value of Sensitivity Analysis

   - Bus Voltage Sensitivity: The analysis shows that all secondary buses can fully reflect the tap changer adjustments, with a sensitivity of 100%.
   - Guidance for Planning and Operation: Sensitivity analysis can provide valuable guidance for distribution network planning and operation, enabling reasonable tap changer settings and optimizing voltage levels across the network.

Through experiments and simulations on large radial distribution networks, it has been confirmed that these findings also hold. In the absence of additional voltage compensation mechanisms, as the feeder length increases and load distribution becomes more complex, voltage drop along the radial lines becomes more pronounced. Therefore, tap changer adjustments have a more significant impact on improving voltages at remote buses, with correspondingly higher sensitivity in larger networks.

5.2.2. Meshed Network Case of Tap Ratio Adjustment

The 14-bus test network is a meshed distribution system. This case does not include any additional voltage support or reactive power compensation devices, such as capacitor banks, reactors, or synchronous condensers. And the generators' active and reactive power outputs are kept constant. A transformer connects bus 4 and bus 9. This network is used to illustrate the impact of transformer tap changer adjustments on bus voltages in a meshed distribution system, and the network topology is shown in the figure 5.4.

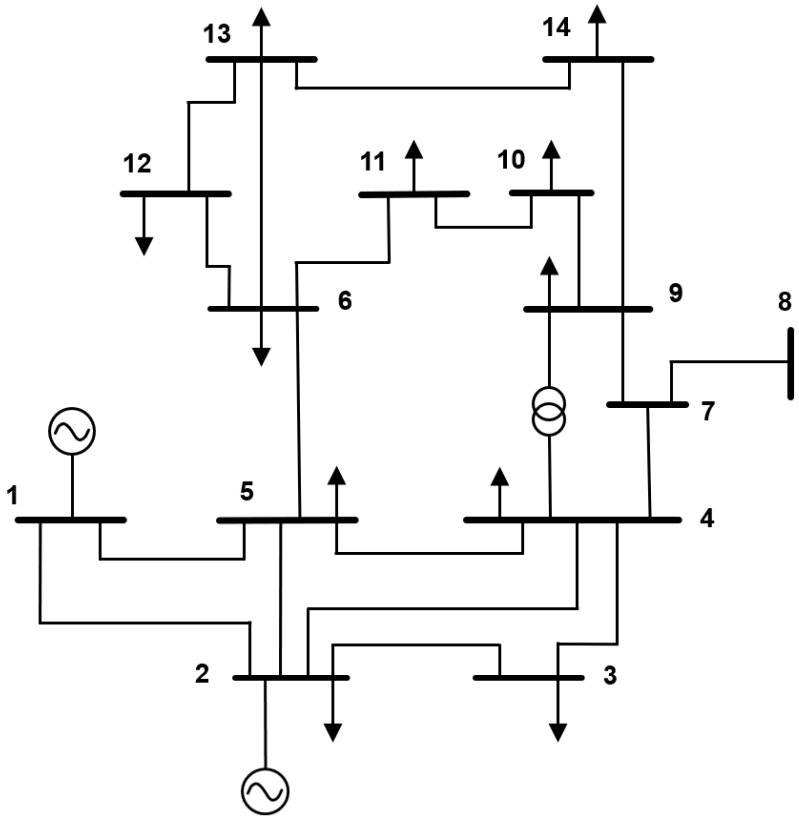

Figure 5.4: 14-Bus Meshed Distribution Test Network for Transformer Tap Ratio Studies.

The corresponding bus and tap ratio data for this meshed network are summarized in Table 5.3 .

BUS	**Tap ratio t=1**	**Tap Ratio t [±5%]**			**Tap Ratio t [±10%]**		
	V_i **(p.u.)**	ΔV_i	$\Delta V_i^{\mathbf{rate}}$	$S_{V_i,t}$	ΔV_i	$\Delta V_i^{\mathbf{rate}}$	$S_{V_i,t}$
1	1.0600	0.0000	0.00%	0.00%	0.0000	0.00%	0.00%
2	1.0450	0.0003	0.00%	0.00%	0.0000	0.00%	0.00%
3	0.9775	0.0006	0.03%	0.66%	0.0007	0.07%	0.66%
4	0.9915	0.0005	0.06%	1.24%	0.0012	0.12%	1.24%
5	1.0004	0.0081	0.05%	1.01%	0.0010	0.10%	1.01%
6	0.9466	0.0145	0.86%	16.27%	0.0163	1.72%	16.27%
7	0.9339	0.0145	1.55%	28.94%	0.0289	3.10%	28.94%
8	0.9339	0.0175	1.55%	28.94%	0.0289	3.10%	28.94%
9	0.9225	0.0158	1.89%	34.91%	0.0349	3.78%	34.91%
10	0.9188	0.0121	1.72%	31.63%	0.0316	3.44%	31.63%
11	0.9288	0.0088	1.30%	24.11%	0.0241	2.60%	24.11%
12	0.9306	0.0095	0.95%	17.65%	0.0177	1.90%	17.65%
13	0.9248	0.0140	1.02%	18.94%	0.0189	2.05%	18.94%
14	0.9050	0.0139	1.54%	27.94%	0.0279	3.09%	27.94%

Table 5.3: Bus voltages and tap ratio results under different tap tolerances in meshed network.

The electrical distance D_i from each bus to the secondary side of the transformer at Bus 9 is demonstrated in the Table 5.4.

From the Table 5.4 and the corresponding Figure 5.4, it can be observed that buses 1–6 are electrically closer to the primary side, while the remaining buses are nearer to the secondary side. To facilitate a more systematic analysis of voltage distribution characteristics, the bus data were filtered and categorized, with buses near the primary and secondary sides and their corresponding data grouped separately. This approach allows for a clear observation of voltage variation patterns across different regions, thereby providing further insight into the impact of transformer tap changes on the system voltage distribution.The simulation results are presented Figures 5.5–5.7

BUS	Distance to Bus 9
1	0.8041
2	0.7418
3	0.7399
4	0.5562
5	0.6004
6	0.5196
7	0.1100
8	0.2862
9	0.0000
10	0.0903
11	0.2992
12	0.8034
13	0.6657
14	0.2988

Table 5.4: Electrical distances of each bus to the transformer secondary side at Bus 9.

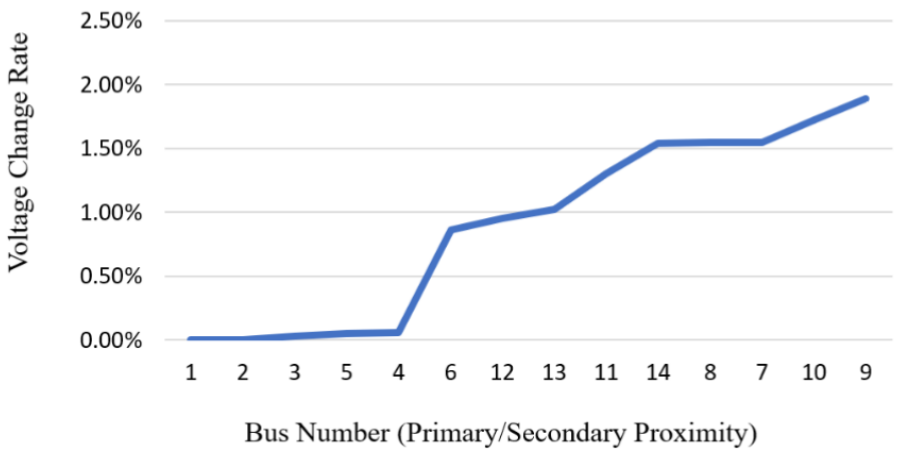

Figure 5.5: Bus Voltage Response under Tap Ratio Adjustment (t±5%)

Note: The horizontal axis represents bus numbers. The transformer primary side corresponds to bus 4, and the secondary side corresponds to bus 9. Buses 1–6, which are electrically closer to the primary side, are listed first and arranged in order of increasing electrical distance from bus 9. Buses 7–14 are electrically closer to the secondary side and are listed afterward in order of decreasing electrical distance from bus 9.

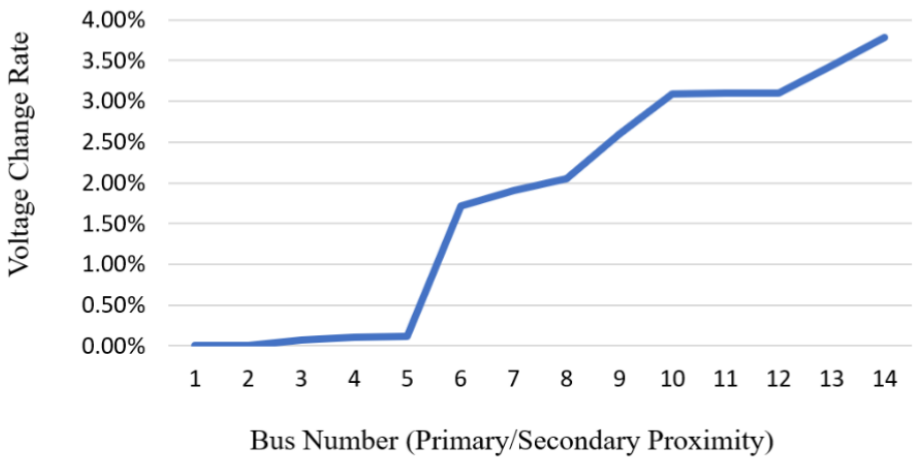

Figure 5.6: Bus Voltage Response under Tap Ratio Adjustment (t±10%)

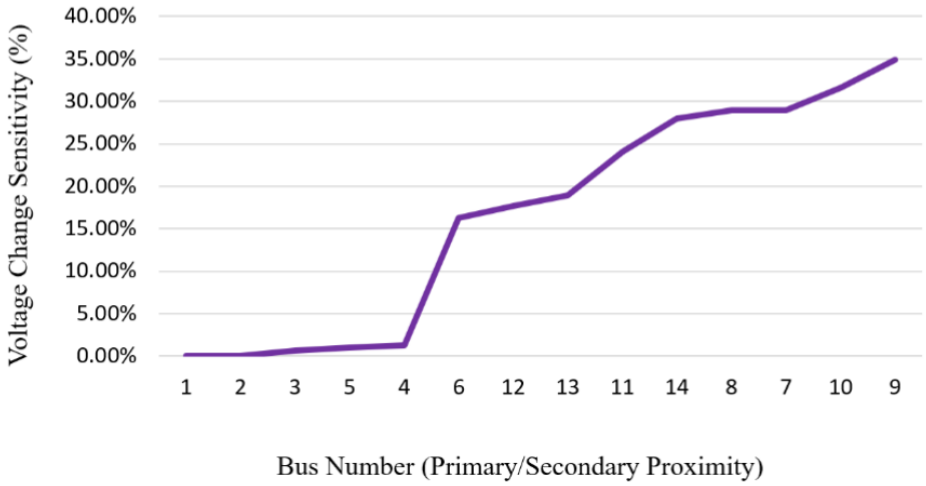

Figure 5.7: Sensitivity of Bus Voltages to Tap Ratio Adjustment (t±5%, t±10%)

In the meshed network, the voltage profile is jointly determined by the transformer tap ratio, line impedance and reactive power flow distribution. Through the analysis of the diagrams presented above, the following conclusions can be obtained:

- Voltage response at the secondary side and neighboring buses: Secondary bus voltages are highly sensitive to tap ratio changes, with voltage increases reaching 3%–4%. Neighboring buses also exhibit noticeable responses. Adjusting the tap ratio of a transformer directly affects the voltage at its secondary bus.
- Voltage variation at the primary side: The primary side, usually located near strong voltage sources or the slack bus (generator nodes), is strongly supported. Voltage

changes at the primary side are negligible after tap adjustments, typically less than 0.2%.

- Uncertain response at remote buses: IIn a meshed network, voltage distribution is influenced by line impedances, the power flow and available reactive power support. Therefore, voltage changes at remote buses are difficult to predict accurately and depend on the network topology and reactive power conditions.
- Bus voltage sensitivity to tap adjustments: Bus voltage sensitivity to tap adjustments decreases with increasing electrical distance. Secondary and load-area buses are the most sensitive and are the primary targets of tap adjustments. In contrast, upstream or generator buses are hardly affected, highlighting the strong voltage support provided by generators.

5.3. Voltage Regulation Capability of Transformer Phase Angle Adjustment

Transformer phase shift angle adjustment is a common method for voltage regulation. By changing the voltage phase angles across a transformer, it controls power flows and bus voltages to optimizes network operation, distributes loads efficiently and enhances system stability. In this section, simulation studies are conducted based on the network configurations described previously to evaluate the voltage regulation performance of phase shift adjustments in both meshed transmission and radial distribution networks.

5.3.1. Radial Network Case of Phase Shift Angle Adjustment

The radial network used in this analysis is based on the same 22-bus configuration described previously. In this study, only the transformer phase shift angles (θ_s) are adjusted, with θ_s varied within the model constraints while all other network parameters remain unchanged. The bus voltages are then calculated to evaluate the voltage response under different phase shift settings.

From the data presented in Table 5.5 as below, it can be observed that altering the transformer phase shift angle θ_s has negligible effect on the voltage magnitudes across the radial network. This behavior arises because, in a radial network, each load is connected to the source via a unique path, and power flow cannot redistribute along multiple paths. As a result, adjusting θ_s does not significantly impact the power flow or voltage magnitudes, but may cause only minor variations in voltage angles.

Overall, phase shift adjustments in a radial distribution system have an almost negligible

influence on the voltage profile. Further simulations on multiple cases as well as analyses on large-scale radial networks yield consistent results, indicating that regardless of the network size or the number of nodes, the impact of phase shift angle adjustments on voltage magnitudes can be neglected.

BUS	$\theta_s = 0$ **(rad)**	$\theta_s = \pm 0.1$ **(rad)**	$\theta_s = \pm 0.2$ **(rad)**
	V_i **(p.u.)**	ΔV_i	ΔV_i
1	1.0000	0.0000	0.0000
2	0.9970	0.0000	0.0000
3	0.9970	0.0000	0.0000
4	0.9928	0.0000	0.0000
5	0.9927	0.0000	0.0000
6	0.9920	0.0000	0.0000
7	0.9920	0.0000	0.0000
8	0.9920	0.0000	0.0000
9	0.9878	0.0000	0.0000
10	0.9878	0.0000	0.0000
11	0.9835	0.0000	0.0000
12	0.9835	0.0000	0.0000
13	0.9812	0.0000	0.0000
14	0.9762	0.0000	0.0000
15	0.9762	0.0000	0.0000
16	0.9759	0.0000	0.0000
17	0.9750	0.0000	0.0000
18	0.9749	0.0000	0.0000
19	0.9739	0.0000	0.0000
20	0.9737	0.0000	0.0000
21	0.9737	0.0000	0.0000
22	0.9735	0.0000	0.0000

Table 5.5: Bus voltage variations under different transformer phase angle settings in the radial network

5.3.2. Meshed Network Case of Phase Shift Angle Adjustment

The network used in this analysis is still based on the 14-bus configuration described previously, with the PST adjustment range maintained as in the earlier study. Building on this setup, the study further investigates the voltage response and power distribution in the meshed network as the PST phase angles are varied. The relevant data are shown

as follows.

BUS	$\theta_s = 0$ (rad)	$\theta_s = \pm 0.1$ (rad)			$\theta_s = \pm 0.2$ (rad)		
	V_i (p.u.)	ΔV_i	$\Delta V_i^{\mathbf{rate}}$	S_{V_i,θ_s}	ΔV_i	$\Delta V_i^{\mathbf{rate}}$	S_{V_i,θ_s}
1	1.0600	0.0000	0.00%	0.00%	0.0000	0.00%	0.00%
2	1.0450	0.0000	0.00%	0.00%	0.0000	0.00%	0.00%
3	0.9775	0.0001	0.06%	0.11%	0.0001	0.01%	0.06%
4	0.9915	0.0002	0.19%	0.25%	0.0004	0.04%	0.19%
5	1.0004	0.0001	0.13%	0.11%	0.0003	0.03%	0.13%
6	0.9466	0.0024	2.35%	2.39%	0.0047	0.50%	2.35%
7	0.9339	0.0023	2.30%	2.27%	0.0046	0.49%	2.30%
8	0.9339	0.0023	2.30%	2.27%	0.0046	0.49%	2.30%
9	0.9225	0.0028	2.80%	2.76%	0.0056	0.61%	2.80%
10	0.9188	0.0021	2.08%	2.04%	0.0042	0.45%	2.08%
11	0.9288	0.0001	0.08%	0.05%	0.0002	0.02%	0.08%
12	0.9306	0.0022	2.19%	2.22%	0.0044	0.47%	2.19%
13	0.9248	0.0015	1.47%	1.51%	0.0029	0.32%	1.47%
14	0.9050	0.0010	1.00%	0.97%	0.0020	0.22%	1.00%

Table 5.6: Bus voltage variations under different transformer phase angle settings in the meshed network

Based on simulations on meshed networks of various sizes and transformers at different locations, the impacts of phase shifting angle on bus voltages can be summarized as follows:

1. Limited voltage regulation capability: In most cases, the voltage variation caused by transformer phase angle adjustments remains within 1.5%, indicating that the direct effect of transformer phase angle control on voltage regulation is rather limited.

2. Influence primarily on power flow distribution: The main role of transformer phase angle adjustments lies in redistributing branch power flows. In meshed networks with more complex topologies, buses located closer to the secondary side of the transformer show relatively higher sensitivity to angle adjustments. However, because of the uneven impedance distribution in the network and the potential reactive power support at distant buses, voltage variations across the system are irregular and generally limited in magnitude.

3. Need for coordination with other control measures: Transformer phase angle ad-

justments, when applied in isolation, are typically inadequate for achieving effective voltage regulation. To enhance the overall voltage control capability of the system, such adjustments generally need to be implemented in coordination with other control mechanisms.

5.4. Case Study 1: Voltage Regulation of Parallel Transformer Tap Staggering

With the integration of intermittent renewable generation, voltage issues in transmission systems have become increasingly dynamic. Deploying and adjusting a large number of reactive power compensators at various locations may not be cost-effective. As an alternative, existing parallel transformers in distribution networks can be utilized to provide reactive power absorption for low load networks. Parallel transformers operating at slightly different tap positions, i.e., with staggered taps, can effectively absorb reactive power.

5.4.1. Network Simulation Setup and Sectioning

To investigate the impact of transformer tap staggering on voltage profiles and power flow characteristics, the IEEE 14-bus system was reconfigured. The modified system is shown in the Figure 5.8. The adapted network was divided into two zones: the upper section (Bus 1–5) represents a light night-load scenario, while the lower section (Bus 6–14) is designed for studies of reactive power support and voltage control. The overall system load was reduced, with the upper section having almost no reactive demand and the lower zones retaining part of the original reactive load, resulting in a significant reactive power imbalance. The two zones are interconnected through three pairs of parallel transformers. Each pair has identical impedance, but their taps can be independently adjusted to implement tap staggering. The line charging susceptances were kept unchanged to ensure the comparability of the power flow results. The specific modified dataset is provided in Appendix A.

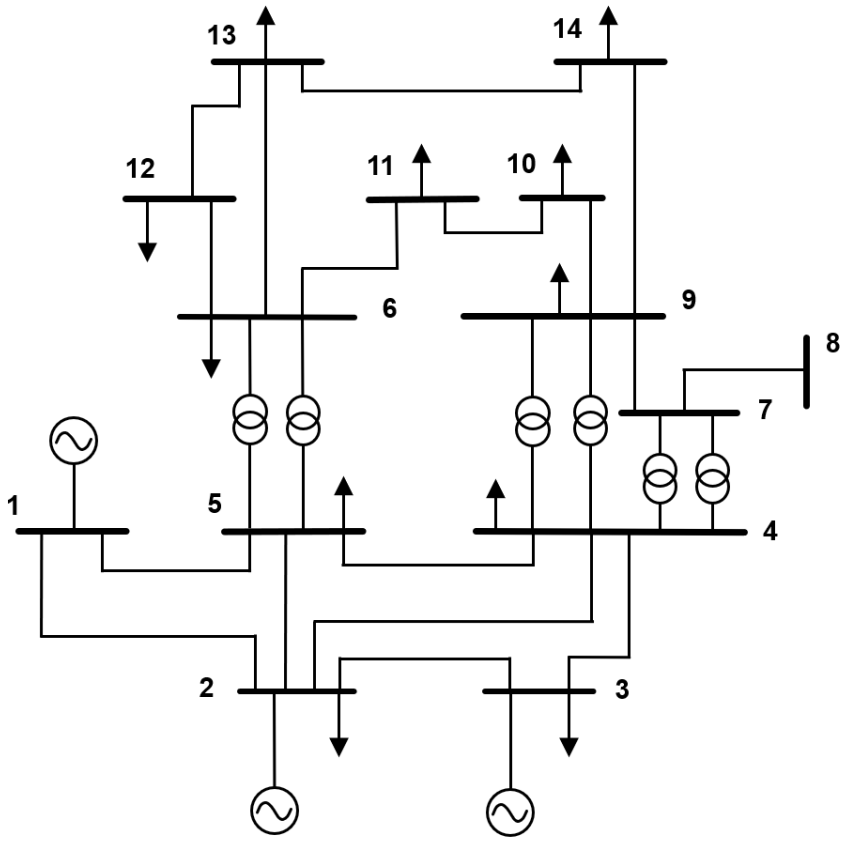

Figure 5.8: Modified IEEE 14-bus test system layout for tap-staggering analysis.

5.4.2. Tap staggering Adjustment Strategy and Procedure

In the simulation, all parallel transformers were initially set to their nominal or central tap positions. At t = 1, no tap staggering effect had been applied. The resulting voltage profile is shown below.

Under the condition without tap staggering, all transformers are set at $t = 1$. At this time, the upper-zone network operates under night load conditions, and the voltages at some buses rise above the rated level. The excessive reactive power generated in the upper zone is transmitted to the lower-zone network through the three parallel transformers, in order to support the overall voltage balance. However, the reactive power regulation capability of the distributed generators (RES) and thermal units in the lower zone has already reached its operational limit, making it impossible to provide further reactive support or to mitigate the over-voltage in the upper zone. Therefore, the imbalance between reactive power injection and consumption across the two zones results in a significant voltage imbalance: the upper-zone voltage rises excessively above the rated level, while the lower-zone voltage remains depressed. Under such conditions, additional reactive compensation

devices or voltage regulation measures are required to restore a balanced voltage profile across the system.

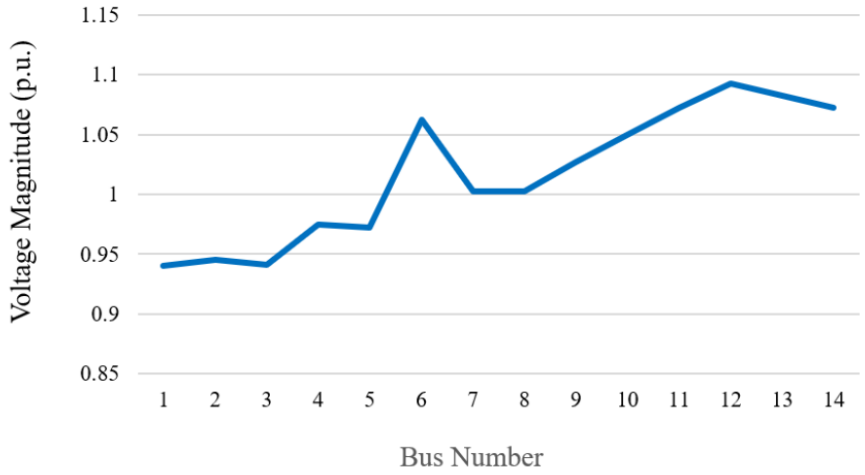

Figure 5.9: Voltage Profile without Tap Staggering Effect (at $t = 1$).

Then, a Tap Staggering operation was implemented in the network. In a set of parallel transformers, the tap position of T1 can be raised by 5%, while that of T2 is lowered by 5%(i.e., $\Delta k = \pm 5\%$); alternatively, T1 can be raised by 10% and T2 lowered by 10%. This operation is simultaneously applied to three sets of parallel transformers, and the resulting voltage variations under different tap adjustment magnitudes are demonstrated in the Table 5.7.

Based on the data in the Table 5.7, the changing trends of the voltage regulation can be more clearly illustrated in the Figure 5.10 below.

Table 5.8 summarizes the results under different tap settings, including the reactive power absorption in tap-staggered parallel transformers. It is reflected in the associated circulating current losses ($\sum \Delta Q_{c,T}$), as well as the total reactive power output ($\sum Q_g$) from generators and other power sources in the network. The corresponding trend is illustrated in Figure 5.11. The values clearly demonstrate the impact of tap staggering on both transformer circulating current losses and the distribution of reactive power within the system.

BUS	Tap ratio $t = 1$	Tap ratio $t \pm \Delta k$ (5%)	Tap ratio $t \pm \Delta k$ (10%)
1	0.9400	0.9400	0.9400
2	0.9454	0.9438	0.9402
3	0.9412	0.9400	0.9400
4	0.9747	0.9702	0.9591
5	0.9720	0.9682	0.9584
6	1.0627	1.0523	1.0236
7	1.0026	0.9928	0.9660
8	1.0026	0.9928	0.9660
9	1.0274	1.0173	0.9896
10	1.0499	1.0396	1.0113
11	1.0722	1.0617	1.0327
12	1.0926	1.0818	1.0521
13	1.0826	1.0719	1.0425
14	1.0722	1.0615	1.0322

Table 5.7: Bus voltages with tap staggering effect in modified 14-bus network.

Note: Δk represents the tap adjustment magnitude in the Tap Staggering operation. In a set of parallel transformers, one transformer is increased by Δk while the other is decreased by Δk, e.g., $\Delta k = 5\%$ or 10%.

Parameter	Tap ratio $t = 1$	Tap ratio $t \pm \Delta k$ (5%)	Tap ratio $t \pm \Delta k$ (10%)
$\sum \Delta Q_{c,T}$	7.9250	12.4588	25.5572
$\sum Q_g$	-84.6929	-78.5797	-61.0486

Table 5.8: Circulating current losses and total reactive power under Tap Staggering operation

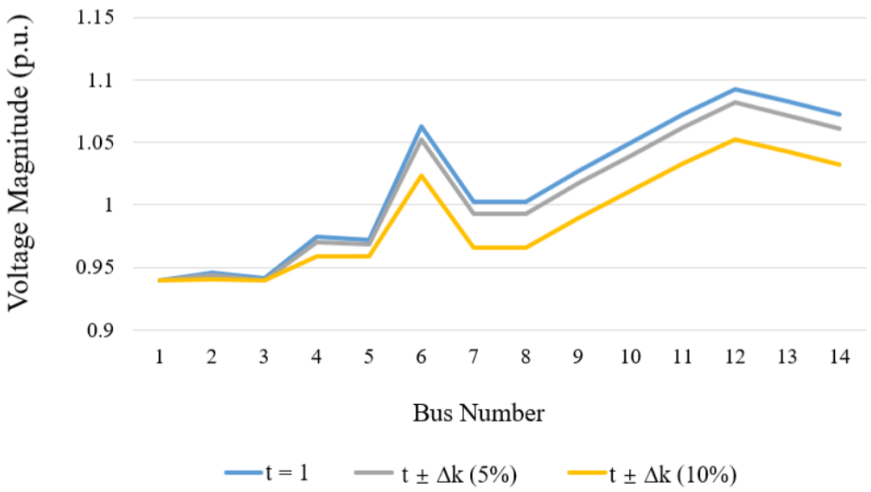

Figure 5.10: Voltage Profile with Tap Staggering Effect.

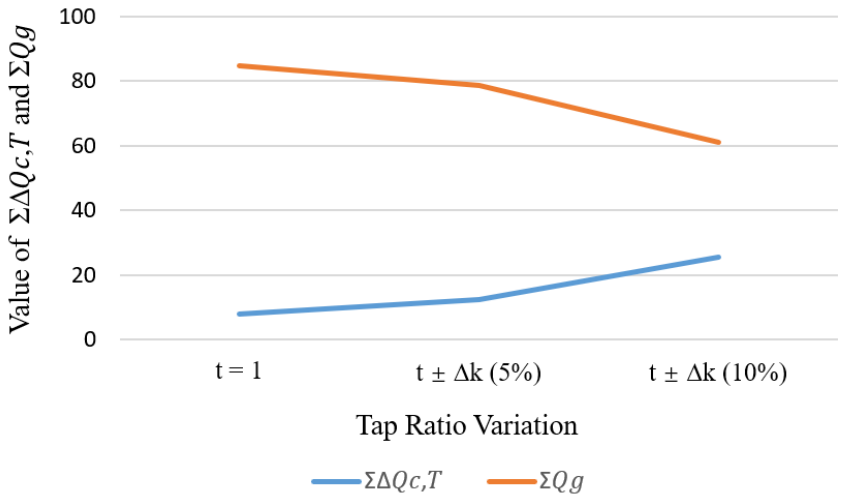

Figure 5.11: Effect of Tap Ratio Variation on Circulating Current Losses and Total Reactive Power Output in Tap Staggering Operation.

5.4.3. Evaluation of Tap Staggering Adjustments Performance

Based on the data presented in the previous tables and figures, the Tap Staggering regulation capability can be analyzed to systematically evaluate the performance of the Tap Staggering adjustment strategy under tap-changing operations, providing a quantitative basis for optimizing the regulation scheme. The data are presented in the Table 5.9.

BUS	Tap ratio t=1	Tap ratio $t \pm \Delta k$ (5%)			Tap ratio $t \pm \Delta k$ (10%)		
	V_i (p.u.)	ΔV_i	$\Delta V_i^{\mathbf{rate}}$	$S_{V_i,t}$	ΔV_i	$\Delta V_i^{\mathbf{rate}}$	$S_{V_i,t}$
1	0.9400	0.0000	0.00%	0.00%	0.0000	0.00%	0.00%
2	0.9400	0.0038	0.41%	7.64%	0.0002	0.03%	0.25%
3	0.9400	0.0000	0.00%	0.00%	0.0000	0.00%	0.00%
4	0.9749	0.0046	0.47%	9.25%	0.0158	1.62%	15.77%
5	0.9724	0.0042	0.43%	8.41%	0.0139	1.43%	13.93%
6	1.0645	0.0123	1.15%	24.56%	0.0409	3.84%	40.90%
7	1.0033	0.0105	1.05%	21.03%	0.0373	3.72%	37.33%
8	1.0033	0.0105	1.05%	21.03%	0.0373	3.72%	37.33%
9	1.0284	0.0111	1.08%	22.25%	0.0388	3.77%	38.76%
10	1.0512	0.0116	1.10%	23.19%	0.0399	3.80%	39.92%
11	1.0738	0.0121	1.13%	24.25%	0.0411	3.82%	41.07%
12	1.0944	0.0126	1.16%	25.29%	0.0423	3.87%	42.31%
13	1.0844	0.0124	1.15%	24.89%	0.0419	3.86%	41.88%
14	1.0737	0.0122	1.13%	24.33%	0.0415	3.86%	41.45%

Table 5.9: Voltage Profile and Tap Staggering Regulation Capability Data.

The network can be divided into two sections based on the location of generation resources and network topology:

1. **Lower Section:** Buses in the lower section (e.g., buses 1–5) are connected to generation resources. Therefore, voltage deviations induced by the Tap Staggering adjustment strategy remain small. The generation nodes provide voltage support, effectively buffering the bus voltages against the impact of tap changes, ensuring stable voltage for loads and system demand.

2. **Upper Section:** Buses in the upper section are located further away from generation nodes. Voltages in this section are more sensitive to Tap Staggering adjustments. Properly staggered Tap positions enable the reduction of upper section voltages, helping to prevent overvoltage in the system.

This characteristic indicates that Tap Staggering adjustments can stabilize lower section voltages while providing an effective means for upper section voltage management and local reactive power control. When the tap offset range is relatively small (e.g., ±4 steps), the magnitude of voltage variation on one side of the transformer remains minimal [38]. This allows Tap Staggering to achieve voltage optimization at the distribution station interface without significantly disturbing the load side voltage, making it an effective

method that balances system stability with local voltage regulation capability.

As shown in Figure 5.11 and Table 5.8, the reactive power absorption of the paralleled transformers caused by circulating currents $\sum \Delta Q_{c,T}$ increases whereas the total reactive power output of generators in the system $\sum Q_g$ decreases with increasing deviation in tap staggering.

In paralleled transformers, tap staggering operations generate circulating currents between the windings. These currents flow through the transformer leakage reactances, leading to additional reactive power consumption denoted as $\Delta Q_{c,T}$. This portion of reactive power is locally absorbed, thereby reducing the system's demand for reactive power generation (as shown in the table, $\sum Q_g$ decreases from –84.6929 MVAr to –61.0486 MVAr). In other words, the circulating currents in the transformers absorb part of the system reactive power, mitigating the reactive burden on the generators, thereby releasing the reactive capacity of the generators.

The released generator reactive capacity can then be utilized to actively regulate system voltage, for example, to further decrease or increase voltage at critical nodes as required. This capability enhances the flexibility of voltage control and improves the system's ability to maintain voltage within desired limits. The effect of this additional reactive capacity on voltage regulation is illustrated in Fig. ××, which shows how the generator resources saved by circulating current absorption can be redistributed to optimize voltage profiles across the network.

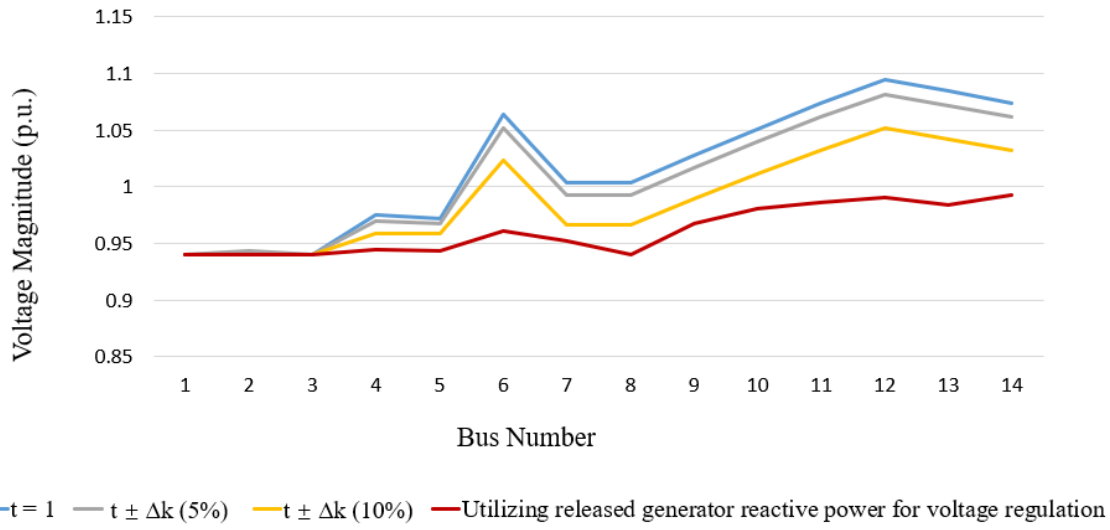

Figure 5.12: Effect of Generator Reactive Power Released by Circulating Current Absorption on System Voltage Regulation.

In summary, Tap Staggering achieves coordinated voltage regulation and optimized local reactive power control by introducing different tap positions on the various sides of parallel transformer groups. In complex or large-scale power networks, tap staggering serves as an auxiliary voltage regulation method and its regulating effect is influenced by factors such as network topology and the coordination among multiple transformers. Therefore, its performance should be comprehensively evaluated through power flow analysis, and it should be applied in coordination with other voltage control devices (such as reactive power compensation equipment and on-load tap changing transformers) to achieve overall system voltage stability and optimized operation.

5.5. Case Study 2: Voltage Regulation of Using Shunt Elements under N-1 Contingency

When the system is operating under extreme conditions (such as N-1 contingencies), and conventional voltage regulation resources (e.g., generator excitation control or tap-changing transformers) are approaching their operational limits, the system becomes more vulnerable to disturbances. Under such circumstances, contingencies can lead to increased voltage instability, potentially resulting in significant voltage drops or overvoltages. And shunt compensation devices including shunt capacitors and shunt reactors can serve as critical auxiliary resources. By rapidly injecting or absorbing reactive power, these devices provide essential voltage support and help mitigate the impact of the contingency on system voltage stability.

5.5.1. N-1 Contingencies and Identification of Critical Buses

In this study, the IEEE 14-bus system (as shown in the Figure 5.13) is used to analyze the system response under N-1 contingencies affecting critical transmission lines. Under high load operating conditions, some conventional voltage regulation methods, such as generator excitation and transformer tap changing, approach their operational limits.

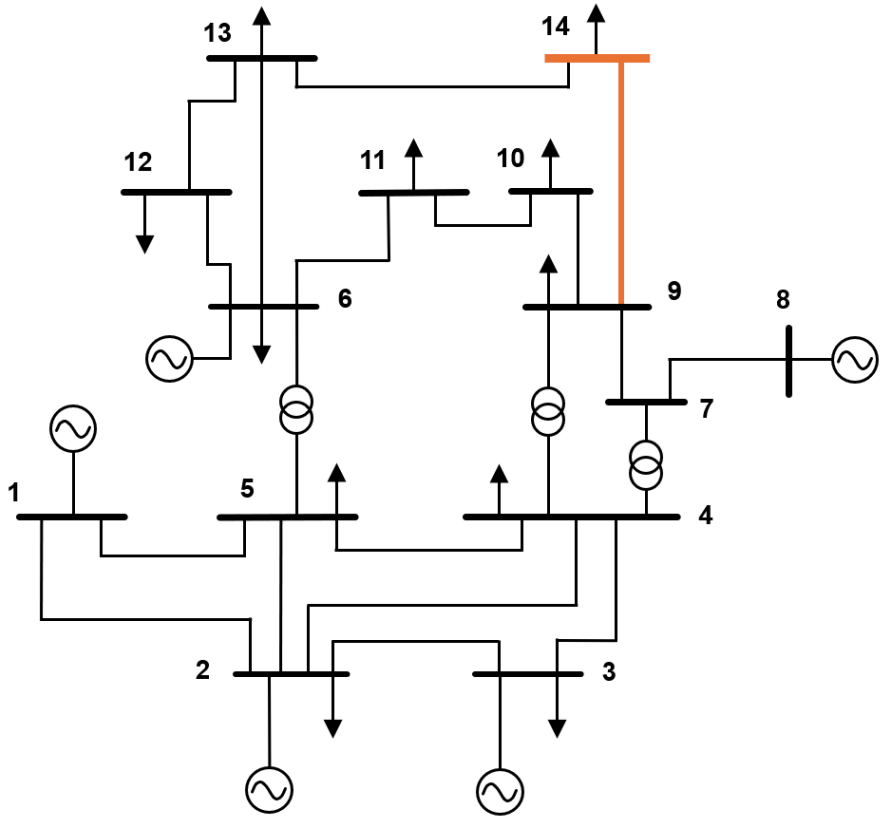

Figure 5.13: Topology of the IEEE 14-Bus System for Contingency Analysis.

N-1 contingency simulations are conducted for all transmission lines in the system. During these simulations, key performance indicators including system voltage deviations and the voltage reductions at each bus, are systematically recorded. The simulation results indicate that the disconnection of branch 17, identified as causing the most severe voltage violation, leads to a significant voltage drop at bus 14 (highlighted in orange in the figure). Key data during the contingency simulation are summarized as follows and can be presented in the Table 5.10.

From Bus	To Bus	Branch No.	Objective Value	Violation Node	Voltage (p.u.)
1	2	1	0.2583		
1	5	2	0.2951		
2	3	3	0.3484		
2	4	4	0.2891		
2	5	5	0.2807		
3	4	6	0.2491		
4	5	7	0.2855		
4	7	8	0.2506		
4	9	9	0.3021		
5	6	10	111.6648	14	0.9289
6	11	11	0.3157		
6	12	12	0.3197		
6	13	13	108.9195	13	0.9292
7	8	14	0.3005		
7	9	15	22.2316	14	0.9378
9	10	16	0.1697		
9	14	17	238.1162	14	0.9162
10	11	18	0.2801		
12	13	19	0.2442		
13	14	20	0.2901		

Table 5.10: N-1 Contingency Results for Critical Branches in IEEE 14-bus case

Based on the simulation results, bus 14 is identified as a critical bus, and the corresponding branch 17 is identified as a critical line. Analysis indicates that this bus and line have the greatest impact on system voltage stability and reactive power distribution, making them the most vulnerable components under N-1 contingencies.

5.5.2. Local Connection Selection of Shunt Element Devices

To enhance voltage stability, a shunt device, such as a controllable shunt capacitor, can be installed at the critical bus. When conventional voltage regulation resources reach their limits, the shunt element can inject or absorb reactive power to support the bus voltage. In optimization studies, the discrete switching operation of shunt devices is modeled using a Binary Switching Variable z, representing whether the device is switched ON or OFF at a given bus. This approach enables the algorithm to automatically determine the optimal locations and statuses for reactive power compensation in the network.

The specific simulation and optimization results are summarized in Table 5.11,which illustrates the bus voltage levels under different network layouts.

Bus No.	Voltage under N-1	Voltage after Shunt Installation	Final Optimized Voltage
1	1.0608	1.0336	1.0130
2	1.0495	1.0259	1.0000
3	1.0000	0.9880	0.9965
4	1.0000	0.9892	1.0016
5	1.0068	1.0000	1.0000
6	1.0600	1.0229	1.0115
7	1.0000	1.0000	1.0000
8	1.0090	1.0000	1.0000
9	0.9746	0.9929	1.0000
10	0.9723	0.9847	0.9990
11	1.0064	0.9983	1.0000
12	1.0222	1.0000	0.9970
13	1.0020	0.9923	0.9963
14	0.9162	1.0000	1.0044

Table 5.11: Bus Voltages under N-1 Contingency and Voltage Support after System Optimization with Shunt Elements

NOTE: Voltage under N-1: represents bus voltage under the N-1 contingency.
Voltage after Shunt Installation: represents bus voltage after installing a shunt capacitor at the most severe voltage violation node (bus 14).
Final Optimized Voltage: bus voltage after further system-wide optimization, where the algorithm automatically determines the optimal status and placement of existing and additional shunt devices to bring voltages closer to target values.

Simulation results show that after installing the shunt device at bus 14, the voltage at this critical bus remains within acceptable limits even under branch 17 disconnection, significantly reducing voltage deviations and improving overall system stability.
In practical power system operation, optimizing the placement and control of shunt devices is crucial for maintaining bus voltages within acceptable limits and enhancing overall system stability. The optimization strategy can be summarized as follows:

- **Overvoltage Handling:** For buses where voltage exceeds the upper limit, shunt reactors or other reactive power absorbing devices are connected to absorb excess reactive power and bring voltage down within safe limits.
- **Undervoltage Handling:** For buses where voltage falls below the lower limit, shunt capacitors are used to inject reactive power and support voltage recovery.

- **Shunt Device Assessment:** The algorithm automatically evaluates the existing shunt device layout to determine which buses can be restored by adjusting current devices and which require the installation of new shunt devices.
- **Optimization Algorithm:** The optimization algorithm uses voltage deviation minimization as the objective function. It automatically adjusts existing device parameters or recommends additional shunt installations to ensure all bus voltages remain within acceptable limits, even under N-1 contingencies.

5.6. Case Study 3: Comprehensive Evaluation of Voltage Regulation Strategies in Complex Power Systems

This case study is based on a power system model consisting of 60 buses. The system includes 23 generators, 31 transformers (8 of which are equipped with on-load tap changers), 22 loads, and 12 shunt compensation devices. The network structure is relatively complex and realistically reflects the characteristics of an actual power grid, making it suitable for a comprehensive evaluation of various voltage regulation strategies under diverse operating conditions.

Among the 31 transformers, 8 are equipped with On-Load Tap Changers (OLTCs), all of which can regulate voltage through tap changing. Additionally, The system consists of two sets of parallel transformer branches, specifically between buses 8–36 and 9–37, where tap-staggering techniques are implemented to improve voltage regulation performance. The system also contains 12 shunt compensation devices, which can be managed using a previously developed automatic shunt device assessment algorithm. This algorithm automatically evaluates the existing shunt device layout to optimize reactive power support and improve voltage stability.

According to the procedure introduced in the previous Section 5.5.1, by intensifying system contingencies, critical lines that have a significant impact on voltage stability can be identified. When the line between bus 34 and bus 15 is disconnected, the voltages at several buses exceed their permissible limits. Subsequently, by applying the voltage regulation methods proposed in Chapter 1, the bus voltages can be restored to their normal ranges. Among these regulation strategies, techniques such as tap staggering and the connection of shunt elements further improve the overall voltage profile, bringing it closer to the reference voltage level and thereby enhancing the system's voltage stability and operational quality.

The following table summarizes the voltage variations during the regulation process, highlighting the specific effects of each voltage control strategy, as detailed in Table 5.12.

Table 5.12: Bus Voltages under Different Voltage Regulation Strategies After N-1 Contingency

Bus	N-1	Regulation	With Tap Staggering	With Shunt Devices
1	1.0000	1.0000	1.0000	1.0000
2	1.0000	1.0000	1.0000	1.0000
3	1.0038	1.0000	1.0000	1.0000
4	1.0019	1.0347	1.0306	1.0090
5	0.9400	0.9649	0.9637	0.9954
6	1.0000	1.0000	0.9994	0.9996
7	0.9647	0.9844	0.9820	1.0000
8	1.0026	1.0035	0.9970	1.0000
9	1.0000	1.0011	1.0000	1.0000
10	1.0529	1.0083	1.0163	1.0417
11	0.9576	1.0000	1.0000	1.0000
12	0.9762	1.0061	1.0060	0.9992
13	1.0000	1.0000	1.0000	1.0003
14	0.9782	1.0059	1.0014	1.0011
15	0.9827	1.0160	1.0146	1.0179
16	0.9690	1.0006	1.0000	1.0023
17	0.9650	0.9961	0.9961	0.9968
18	0.9973	1.0000	1.0005	1.0000
19	0.9900	1.0002	1.0000	1.0026
20	0.9400	1.0036	1.0012	1.0012
21	0.9690	1.0121	1.0113	1.0119
22	0.9624	1.0000	1.0000	1.0000
23	0.9400	1.0026	1.0025	1.0004
24	1.0108	1.0004	1.0004	1.0004
25	0.9692	1.0000	1.0000	1.0000
26	0.9400	1.0000	1.0000	1.0000
27	1.0059	1.0093	1.0080	1.0122
28	0.9447	1.0000	1.0000	1.0115
29	1.0078	1.0196	1.0160	1.0172
30	0.9400	1.0000	1.0000	1.0000
31	0.9788	1.0046	1.0000	1.0000
32	0.9432	1.0000	1.0000	1.0000
33	0.9432	1.0000	1.0000	1.0000

Continued on next page

Table 5.12 – continued from previous page

Bus	N-1	Regulation	With Tap Staggering	With Shunt Devices
34	0.9400	0.9653	0.9656	0.9699
35	1.0798	1.0306	1.0270	1.0282
36	0.9754	1.0058	1.0039	1.0098
37	0.9779	1.0107	1.0097	1.0175
38	0.9507	1.0000	1.0000	1.0000
39	1.0000	1.0000	1.0000	1.0000
40	1.0000	1.0000	1.0000	1.0000
41	0.9400	0.9649	0.9690	0.9906
42	0.9400	1.0000	1.0000	1.0000
43	1.0537	1.0000	1.0000	1.0000
44	1.0000	1.0000	1.0000	1.0000
45	0.9400	1.0000	0.9858	0.9738
46	0.9421	0.9684	0.9689	1.0000
47	0.9708	1.0000	1.0000	1.0000
48	0.9400	0.9630	0.9617	0.9725
49	0.9400	0.9602	0.9555	0.9555
50	0.9400	0.9685	0.9745	0.9657
51	1.0000	1.0000	1.0000	1.0000
52	1.0000	0.9963	0.9984	0.9948
53	1.0431	1.0000	1.0000	1.0000
54	1.0559	1.0000	1.0000	1.0000
55	1.0000	1.0000	1.0000	1.0000
56	0.9890	1.0000	1.0000	1.0000
57	1.0000	1.0000	1.0000	1.0000
58	1.0000	1.0000	1.0000	1.0000
59	1.0000	1.0000	1.0000	1.0000
60	1.0153	0.9964	0.9965	1.0000
Objective	199.5644	0.4451	0.4418	0.3713

NOTE:
N-1: represents bus voltage under the N-1 contingency.
Regulation: Voltage regulation implemented by tap changers or reactive power support from generator resources (Q_g).
With Tap Staggering: Voltages regulation with tap staggered settings in parallel transformers.
With Shunt Devices: Voltages after installing shunt compensation devices for further voltage support.

Based on the analysis of the above table, the following conclusions can be drawn:

- Voltage regulation methods, such as tap changers or reactive power resources from generators (Q_g) significantly reduce system voltage deviations. The objective function value decreases to 0.4451, indicating effective restoration and stabilization of bus voltages.
- The introduction of tap staggering techniques further optimizes the voltage regulation scheme, reducing the objective function value to 0.4418. This suggests that staggered tap adjustments produce a more uniform voltage profile, mitigating voltage fluctuations at local buses and improving overall voltage regulation performance and system stability.
- The application of shunt devices as voltage regulation means yields the most significant improvement, with the objective function value decreasing to 0.3713. This demonstrates that shunt devices have a strong capability to enhance bus voltage stability and more effectively alleviate voltage anomalies caused by line disconnections, thereby substantially improving the system's disturbance resilience.

Based on the above analysis, further optimization of the voltage regulation scheme can be pursued. It is observed that buses 34 and 35 remain system weak points, as the previous regulation methods could not significantly improve voltage profile to the reference values. Therefore, additional shunt devices can be installed at buses exhibiting large voltage deviations to enhance voltage regulation and system performance.
The final optimization scheme obtained through this approach, as detailed in the previous Section 5.5.2, and the final optimized scheme achieves a significantly reduced objective function value of 0.2217. As illustrated in the Figure 5.14, the final optimized scheme demonstrates improved voltage profiles and reduced deviations compared to the previous regulation methods, as shown in the following comparison.

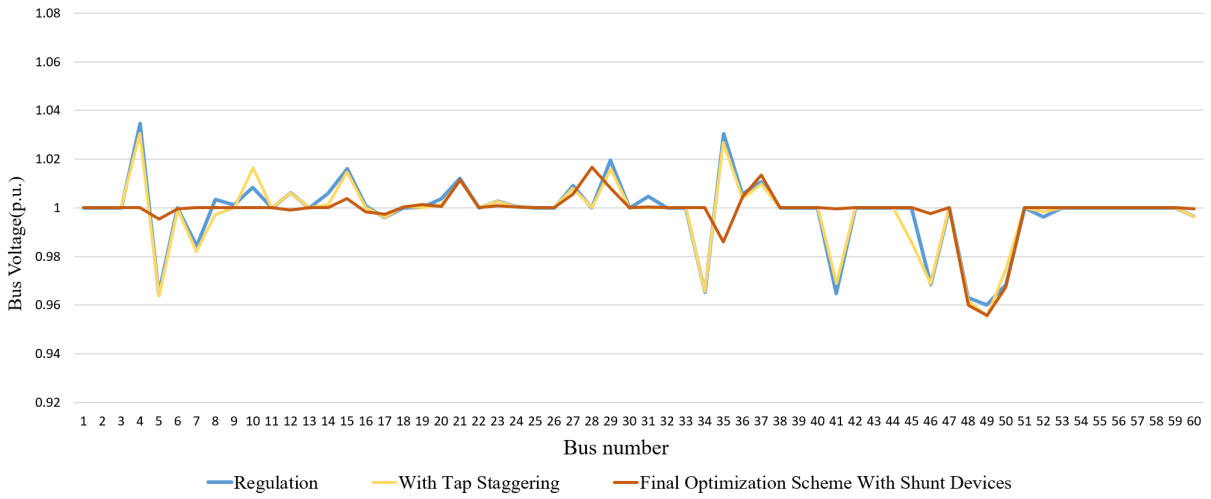

Figure 5.14: Comparison of Bus Voltage Profiles under Different Voltage Regulation Schemes

As illustrated in the above figure, the effects of the previously implemented voltage regulation schemes are clearly evident. All regulation methods contributed to voltage improvement to some extent, though their effectiveness varies significantly. The tap staggering technique primarily achieves minor voltage reduction within localized areas, with limited overall impact due to the presence of other reactive power supports in the system.

In contrast, the application of shunt devices demonstrates a more pronounced voltage regulation effect, effectively increasing bus voltages in affected regions, substantially mitigating voltage deviations, and enhancing overall voltage stability.

6 | DLPF-MILP Model Performance

The main objective of this chapter is to validate the feasibility and accuracy of solutions obtained from the DLPF-MILP Model in realistic AC power systems.
Specifically, this chapter evaluates the performance of the proposed model from two perspectives:

1. **Model Accuracy** — the consistency between the results obtained from the linearized model and those derived ACPF calculations.
2. **Computational Efficiency** — the performance of the model in terms of convergence speed and scalability.

Specifically, the optimization results from all previous simulation cases are applied to AC power flow calculations.

6.1. Purpose and Need for Linearized Model Validation

Through comparing the bus voltages predicted by the linearized model with the actual results obtained from AC power flow calculations, the accuracy and applicability of the linearized model can be systematically assessed. This verification process helps ensure that the linear assumptions do not introduce significant errors under practical operating conditions, thereby guaranteeing the engineering feasibility of the proposed optimization scheme. In this process, the operational plans or voltage control strategies obtained from the optimization algorithm are directly applied to the AC power flow calculations for validation, thereby examining the performance of the linearized model under actual power system operating conditions.

Based on this approach, the evaluation focuses on the following aspects:

- **Feasibility**: Verify whether the optimization schemes obtained from the DLPF-

MILP optimization can produce convergent solutions in a full AC system.

- **Accuracy**: Analyze the deviations between the DLPF-MILP model's predicted bus voltages and power flow quantities and those obtained from ACPF results.

6.2. Key Evaluation Metrics of the Linearized Optimization Model

This subsection introduces a set of key evaluation metrics designed to quantify the accuracy and feasibility of the linearized optimization model. By comparing the bus voltages obtained from the linearized optimization with the actual voltages calculated through ACPF, the performance and reliability of the model can be systematically assessed.

Absolute voltage and angle error: This metric quantifies the difference between the predicted and actual bus voltages:

$$V_{i,\text{err}} = |V_{i,\text{opt}} - V_{i,\text{AC}}| \tag{6.1}$$

where:

- $V_{i,\text{AC}}$: actual voltage at bus i from AC power flow calculations.
- V_i^{opt}: predicted voltage at bus i from the optimization model.
- $V_{i,\text{err}}$: absolute voltage error at bus i.

$$\theta_{i,\text{err}} = |\theta_{i,\text{opt}} - \theta_i^{\text{AC}}| \tag{6.2}$$

where:

- θ_i^{AC}: actual voltage angle at bus i from AC power flow calculations.
- $\theta_{i,\text{opt}}$: predicted voltage angle at bus i from the optimization model.
- $\theta_{i,\text{err}}$: absolute voltage angle error at bus i.

Mean Absolute Error (MAE): This metric represents the average absolute deviation of the predicted voltages from the actual voltages across all buses:

$$\mathrm{MAE}_V = \frac{1}{N}\sum_{i=1}^{N} |V_{i,\mathrm{opt}} - V_{i,\mathrm{AC}}| \tag{6.3}$$

$$\mathrm{MAE}_\theta = \frac{1}{N}\sum_{i=1}^{N} |\theta_{i,\mathrm{opt}} - \theta_{i,\mathrm{AC}}| \tag{6.4}$$

where:

- N: total number of buses in the system.

Relative voltage error: This metric evaluates the deviation of the predicted voltage relative to the actual voltage:

$$V_{i,\mathrm{err}}^{\mathrm{rel}} = \frac{|V_{i,\mathrm{opt}} - V_{i,\mathrm{AC}}|}{V_{i,\mathrm{AC}}} = \frac{|V_{i,\mathrm{err}}|}{V_{i,\mathrm{AC}}} \tag{6.5}$$

where:

- $V_{i,\mathrm{err}}^{\mathrm{rel}}$: relative voltage error at bus i.

$$\theta_{i,\mathrm{err}}^{\mathrm{rel}} = \frac{|\theta_{i,\mathrm{opt}} - \theta_{i_{\mathrm{AC}}}|}{|\theta_{i_{\mathrm{AC}}}|} = \frac{|\theta_{i,\mathrm{err}}|}{|\theta_{i_{\mathrm{AC}}}|} \tag{6.6}$$

where:

- $\theta_{i,\mathrm{err}}^{\mathrm{rel}}$: relative voltage angle error at bus i.

Mean Relative Absolute Error (MRAE): This metric represents the average relative absolute deviation of the predicted voltages from the actual voltages across all buses:

$$\mathrm{MRAE}_V = \frac{1}{N}\sum_{i=1}^{N} \frac{|V_{i,\mathrm{opt}} - V_{i,\mathrm{AC}}|}{|V_{i,\mathrm{AC}}|} \tag{6.7}$$

$$\mathrm{MRAE}_\theta = \frac{1}{N}\sum_{i=1}^{N} \frac{|\theta_{i,\mathrm{opt}} - \theta_{i,\mathrm{AC}}|}{|\theta_{i,\mathrm{AC}}|} \tag{6.8}$$

where:

- N: total number of buses in the system.

Prediction accuracy (Accuracy): The overall accuracy of the optimization model can be quantified using the mean relative error of all buses, expressed as a percentage:

$$\text{Accuracy}_V = \left(1 - \frac{1}{N}\sum_{i=1}^{N} V_{i,\text{err}}^{\text{rel}}\right) \times 100\% \tag{6.9}$$

$$\text{Accuracy}_\theta = \left(1 - \frac{1}{N}\sum_{i=1}^{N} \theta_{i,\text{err}}^{\text{rel}}\right) \times 100\% \tag{6.10}$$

where:

- Accuracy: the overall prediction accuracy of the optimization model. Higher values indicate that the predicted voltages more closely match the results obtained from AC power flow calculations.

6.3. Accuracy Evaluation Across Case Studies 1 to 3

To comprehensively evaluate the performance of the proposed DLPF-MILP model, the prediction accuracy was examined across multiple simulation cases with varying load levels and contingency scenarios.

6.3.1. Model Accuracy Analysis in Case Study 1

The error analysis of the model is shown in the Table 6.1 and Table 6.2.
In the application of Tap Staggering strategy, the accuracy of the DLPF-MILP model is evaluated by comparing bus voltage magnitudes and phase angles against ACPF results under different tap ratio conditions.

- **Voltage Magnitude Error:** The MAE values under all conditions are very small, ranging from approximately 0.001 to 0.002 p.u., and the relative errors are also very low. This indicates that the model's predictions are very close to the actual ACPF results. These small and stable errors demonstrate that the model maintains high accuracy in voltage magnitude calculation when Tap Staggering is applied.
- Voltage Phase Angle Error: The mean absolute errors of voltage phase angles are all less than 1 degree, which is within a reasonable range for engineering applications. Although the phase angle errors are higher than those for voltage magnitude, the model still demonstrates good estimation capability for phase angles. Moreover, the errors show no significant variation within the range of tap ratio disturbances,

indicating model robustness.

Therefore, when applying Tap Staggering for voltage regulation, the DLPF-MILP model achieves small errors in both bus voltage magnitude and phase angle, meeting practical operational analysis requirements and demonstrating good engineering applicability.

BUS	**Tap ratio** $t = 1$		**Tap ratio** $t \pm \Delta k$ **(5%)**		**Tap ratio** $t \pm \Delta k$ **(10%)**	
	$V_{i,\mathbf{err}}$	$V_{i,\mathbf{err}}^{\mathbf{rel}}$	$V_{i,\mathbf{err}}$	$V_{i,\mathbf{err}}^{\mathbf{rel}}$	$V_{i,\mathbf{err}}$	$V_{i,\mathbf{err}}^{\mathbf{rel}}$
1	0.0000	0.0000	0.0000	0.0000	0.0000	0.0000
2	0.0054	0.0057	0.0038	0.0040	0.0002	0.0003
3	0.0012	0.0013	0.0000	0.0000	0.0000	0.0000
4	0.0002	0.0002	0.0025	0.0026	0.0113	0.0118
5	0.0004	0.0004	0.0056	0.0058	0.0149	0.0155
6	0.0019	0.0018	0.0138	0.0131	0.0260	0.0254
7	0.0007	0.0007	0.0112	0.0113	0.0245	0.0254
8	0.0007	0.0007	0.0112	0.0113	0.0245	0.0254
9	0.0010	0.0010	0.0161	0.0158	0.0104	0.0104
10	0.0013	0.0012	0.0111	0.0106	0.0123	0.0123
11	0.0016	0.0015	0.0011	0.0010	0.0064	0.0062
12	0.0019	0.0017	0.0119	0.0110	0.0131	0.0126
13	0.0017	0.0016	0.0097	0.0091	0.0196	0.0189
14	0.0015	0.0014	0.0051	0.0049	0.0033	0.0032
MAE_V	0.0004		0.0015		0.0025	
MRAE_V		0.0013		0.0071		0.0119
Accuracy_V		99.86%		99.28%		98.80%

Table 6.1: Model Accuracy Analysis of Bus Voltage Magnitudes(p.u.) between DLPF-MILP and ACPF in Tap Staggering.

BUS	Tap ratio $t = 1$		Tap ratio $t \pm \Delta k$ (5%)		Tap ratio $t \pm \Delta k$ (10%)	
	$\theta_{i,\mathbf{err}}$	$\theta^{\mathbf{rel}}_{i,\mathbf{err}}$	$\theta_{i,\mathbf{err}}$	$\theta^{\mathbf{rel}}_{i,\mathbf{err}}$	$\theta_{i,\mathbf{err}}$	$\theta^{\mathbf{rel}}_{i,\mathbf{err}}$
1	0.0000	–	0.0000	–	0.0000	–
2	0.3214	0.2771	0.2861	0.2535	0.2128	0.2010
3	0.5238	0.1582	0.4946	0.1499	0.5029	0.1513
4	0.5779	0.1191	0.5275	0.1103	0.3633	0.0790
5	0.5298	0.1226	0.4757	0.1116	0.3220	0.0785
6	0.5286	0.0709	0.7422	0.1000	0.9045	0.1233
7	0.6148	0.1103	0.5305	0.0962	0.3447	0.0644
8	0.6148	0.1103	0.5305	0.0962	0.3447	0.0644
9	0.6146	0.0995	0.5049	0.0824	0.3144	0.0524
10	0.5799	0.0831	0.5239	0.0755	0.4000	0.0586
11	0.5219	0.0678	0.5966	0.0778	0.6148	0.0812
12	0.3995	0.0450	0.6464	0.0729	0.8572	0.0974
13	0.4304	0.0503	0.6189	0.0726	0.7713	0.0911
14	0.4566	0.0538	0.4960	0.0586	0.4966	0.0592
MAE_θ	0.4795		0.4981		0.4606	
MRAE_θ		0.0976		0.0969		0.0858
Accuracy_θ		90.23%		90.30%		91.42%

Table 6.2: Model Accuracy Analysis of Bus Voltage Phase Angles (degrees) between DLPF-MILP and ACPF in Tap Staggering.

6.3.2. Model Accuracy Analysis in Case Study 2

Table 6.3 shows the accuracy analysis between the DLPF-MILP model and the ACPF method under normal operating conditions without any faults in 14-bus system.
After a contingency event occurs, voltage regulation control is implemented to mitigate voltage deviations and maintain system stability. The resulting optimized voltage regulation scheme is then validated by applying it back to the full AC power flow model. The results are summarized in Table 6.4.

Bus	$V_{i,\mathbf{err}}$	$\theta_{i,\mathbf{err}}$	$V_{i,\mathbf{err}}^{\mathbf{rel}}$	$\theta_{i,\mathbf{err}}^{\mathbf{rel}}$
1	0.0000	0.0000	0.0000	0.0000
2	0.0000	0.2413	0.0000	0.0485
3	0.0000	0.4890	0.0000	0.0385
4	0.0061	0.5552	0.0060	0.0542
5	0.0074	0.5317	0.0073	0.0605
6	0.0000	0.5785	0.0000	0.0371
7	0.0025	0.7372	0.0023	0.0464
8	0.0000	0.7372	0.0000	0.0464
9	0.0024	0.8428	0.0023	0.0497
10	0.0017	0.8326	0.0016	0.0490
11	0.0008	0.7313	0.0008	0.0445
12	0.0003	0.6987	0.0003	0.0424
13	0.0002	0.7240	0.0002	0.0436
14	0.0008	0.8832	0.0008	0.0496
MAE	0.0015	0.6130		
MRAE			0.0015	0.0435
Accuracy			99.85%	95.64%

Table 6.3: Model Accuracy Analysis of Bus Magnitudes(p.u.) and Phase Angles (degrees) between DLPF-MILP and ACPF under Normal Conditions in 14-bus system.

Bus	$V_{i,\mathbf{err}}$	$\theta_{i,\mathbf{err}}$	$V_{i,\mathbf{err}}^{\mathbf{rel}}$	$\theta_{i,\mathbf{err}}^{\mathbf{rel}}$
1	0.0000	0.0000	0.0000	0.0000
2	0.0000	0.0000	0.3434	0.1978
3	0.0000	0.0000	0.6573	0.0669
4	0.0098	0.0099	0.4989	0.0695
5	0.0086	0.0087	0.5022	0.1009
6	0.0000	0.0000	1.7452	0.1377
7	0.0244	0.0250	0.5162	0.0910
8	0.0000	0.0000	0.2067	0.0129
9	0.0277	0.0222	0.0073	0.0425
10	0.0265	0.0241	1.1198	0.2982
11	0.0167	0.0169	1.5040	0.1776
12	0.0050	0.0051	1.7649	0.1134
13	0.0084	0.0085	1.7397	0.1023
14	0.0183	0.0186	1.9426	0.0783
MAE	0.0097	0.8952		
MRAE			0.0099	0.1062
Accuracy			99.00%	89.36%

Table 6.4: Model Accuracy Analysis of Bus Voltage Magnitudes (p.u.) and Phase Angles (degrees) between DLPF-MILP and ACPF under N-1 Contingency for the Final Optimized Scheme in the 14-Bus System.

In normal operating conditions, the DLPF-MILP model exhibits small errors in voltage magnitude and phase angle compared to the ACPF model, with mean absolute errors (MAE) of 0.0015 p.u. and 0.06130 degrees, and accuracies of 99.85% and 93.03%, respectively. This indicates that the model achieves high prediction accuracy under normal conditions.

After an N-1 contingency, the model accuracy was further validated using the optimized voltage regulation scheme. The results show that the voltage magnitude error remains small, with an MAE of only 0.009 p.u., while the phase angle error increases but still stays within 1 degree. Although the errors have increased slightly, the overall prediction accuracy remains high, demonstrating that the method effectively maintains good accuracy and system stability under contingency and subsequent regulation scenarios.

In summary, the proposed DLPF-MILP model closely approximates the ACPF results

under different operating conditions and possesses strong practical application value.

6.3.3. Model Accuracy Analysis in Case Study 3

In this case study, the model accuracy analysis was conducted following the previously described procedures. To ensure system stability and performance optimization, all the aforementioned voltage regulation measures were comprehensively applied. The Table **??** presents a comparison of voltage magnitude and phase angle errors at each bus, clearly reflecting the model's effectiveness under practical operating conditions.

Table 6.5: Model Accuracy Analysis of Bus Voltage Magnitudes (p.u.) and Phase Angles (degrees) between DLPF-MILP and ACPF in 60-bus System

Bus	$V_{i,\mathbf{err}}$	$\theta_{i,\mathbf{err}}$	$V_{i,\mathbf{err}}^{\mathbf{rel}}$	$\theta_{i,\mathbf{err}}^{\mathbf{rel}}$
1	0.0131	1.5395	0.0133	0.4466
2	0.0087	1.5763	0.0088	0.4594
3	0.0053	1.5833	0.0053	0.3165
4	0.0144	1.5040	0.0144	0.2610
5	0.0083	1.4098	0.0084	0.0743
6	0.0048	1.3018	0.0048	0.1690
7	0.0078	1.3660	0.0079	0.0831
8	0.0121	1.2721	0.0122	0.0918
9	0.0052	1.3611	0.0052	0.0804
10	0.0085	1.4711	0.0082	0.1048
11	0.0038	1.4816	0.0038	0.0989
12	0.0149	1.4355	0.0152	0.1413
13	0.0080	1.3644	0.0081	0.0872
14	0.0143	1.5718	0.0145	0.1194
15	0.0117	1.3690	0.0116	0.1351
16	0.0134	0.9152	0.0136	0.1002
17	0.0114	0.6688	0.0116	0.0925
18	0.0086	0.4612	0.0087	0.0960
19	0.0059	1.4164	0.0059	0.0732
20	0.0146	1.7325	0.0148	0.0887
21	0.0080	1.7329	0.0079	0.0781
22	0.0040	1.7587	0.0040	0.0738
23	0.0132	1.5682	0.0134	0.4001
24	0.0038	1.6035	0.0038	0.3592
25	0.0072	1.6648	0.0072	0.2749
26	0.0150	0.4643	0.0152	0.0836

Continued on next page

Table 6.5 – *Continued from previous page*

Bus	$V_{i,\mathbf{err}}$	$\theta_{i,\mathbf{err}}$	$V^{\mathbf{rel}}_{i,\mathbf{err}}$	$\theta^{\mathbf{rel}}_{i,\mathbf{err}}$
27	0.0129	1.0114	0.0129	0.0890
28	0.0205	1.5994	0.0207	0.3048
29	0.0140	1.4308	0.0139	0.1146
30	0.0010	0.0828	0.0010	0.0045
31	0.0142	1.5459	0.0144	0.1178
32	0.0114	1.5764	0.0115	0.0930
33	0.0114	1.5764	0.0115	0.0930
34	0.0092	1.2983	0.0095	0.1466
35	0.0141	1.4300	0.0139	0.1142
36	0.0155	1.2494	0.0156	0.0963
37	0.0153	1.3500	0.0153	0.0824
38	0.0000	0.4242	0.0000	0.0773
39	0.0000	1.5702	0.0000	0.2135
40	0.0000	0.3968	0.0000	0.0608
41	0.0000	1.6636	0.0000	0.2781
42	0.0000	1.6031	0.0000	0.2684
43	0.0000	1.2848	0.0000	0.2746
44	0.0000	1.3459	0.0000	0.0964
45	0.0000	1.4800	0.0000	0.0991
46	0.0000	0.4649	0.0000	0.0831
47	0.0000	0.4325	0.0000	0.0724
48	0.0000	1.0093	0.0000	0.0894
49	0.0000	1.5421	0.0000	0.1181
50	0.0000	1.5718	0.0000	0.1194
51	0.0000	1.3693	0.0000	0.1359
52	0.0000	0.0000	0.0000	0.0000
53	0.0000	0.4606	0.0000	0.0974
54	0.0000	1.4162	0.0000	0.0734
55	0.0000	1.4162	0.0000	0.0734
56	0.0000	1.7332	0.0000	0.0784
57	0.0000	1.7531	0.0000	0.0781
58	0.0000	1.7584	0.0000	0.0740
59	0.0000	1.3527	0.0000	0.0898
60	0.0000	1.3270	0.0000	0.0664
MAE	0.0064	1.2142		
MARE			0.0065	0.1377
Accuracy			99.35%	86.23%

Based on the results shown in the table, the proposed DLPF-MILP model demonstrates high accuracy in predicting bus voltage magnitudes and phase angles compared to the benchmark ACPF model. The average error in voltage magnitude remains low at 0.006 p.u., with an accuracy exceeding 99%, indicating strong consistency between the two models. Although the phase angle error is slightly larger, the average relative error is 0.1377 degrees and remains low, which is fully acceptable in practical system operations.

Overall, the DLPF-MILP model can reliably approximate power flow solutions under typical operating conditions while incorporating various voltage regulation measures. Despite some errors introduced by linearization approximations and other factors, the model maintains high predictive accuracy, demonstrating strong practical value and significant potential for wider application.

6.4. Computational Efficiency of the DLPF-MILP Model in Voltage Optimization Problems

Besides accuracy, the computational efficiency of the proposed DLPF-MILP model is also a critical factor for its practical application. Especially in large-scale power systems, the ability to quickly obtain results is essential for real-time decision-making and system voltage optimization control. Compared to the traditional ACPF model, which requires iterative solving and has relatively long computation times, the DLPF-MILP model significantly reduces computational complexity and greatly improves calculation speed through linearization and mixed-integer linear programming techniques.

Table 6.6 presents the execution times of the DLPF-MILP model for voltage optimization problems in power systems of different scales (in seconds).

Test Case	$t^{DLPF-MILP}$
IEEE 60nordic-bus	0.01
IEEE 118-bus	0.02
IEEE 300-bus	0.04
IEEE 533mt-bus	0.03
Pegase 1354-bus	0.23
Pegase 2869-bus	1.45

Table 6.6: Execution Time of DLPF-MILP Model on Large-scale Networks.

Simulation results indicate that the proposed model exhibits excellent computational efficiency. With the support of the linearized modeling framework, the solution speed and stability are greatly improved. For systems with up to approximately 1,000 buses, the total computation time is typically below 0.5 seconds. For larger networks of around one thousand buses, the solution is usually obtained within 0.5 to 2 seconds, fully verifying the efficiency and practicality of the proposed linearized optimization model.

7 | Conclusion

This thesis proposes a Decoupled Linear Power Flow—Mixed Integer Linear Programming (DLPF-MILP) model for large-scale power systems, aimed at voltage optimization and power flow analysis. The model linearizes the nonlinear characteristics of the Alternating Current Power Flow (ACPF) equations and combines them with mixed integer linear programming methods, achieving a good balance between computational accuracy and solution efficiency. By decoupling the active and reactive power modeling and using linear approximations for voltage control variables, the model significantly improves computational speed while maintaining high accuracy, providing a feasible approach for real-time or near-real-time system regulation and optimization.

For model accuracy validation, case studies under various operating conditions—including normal and N-1 contingency scenarios—were conducted. The results show that the DLPF-MILP model aligns closely with the benchmark ACPF results: the average error in bus voltage magnitude is less than 0.01 p.u., and the average phase angle error is less than 1°. This indicates that the errors introduced by the linearization approximation are minimal and controllable, without affecting the overall system characteristic representation. Furthermore, after incorporating various voltage regulation measures, the model still maintains high accuracy and stability, demonstrating strong robustness and engineering applicability.

In terms of computational performance, the DLPF-MILP model exhibits significant efficiency advantages. Compared to the traditional nonlinear ACPF model, which requires repeated iterations and updates of the Jacobian matrix, the DLPF model reduces computational complexity and memory usage through the combination of linearization and optimization frameworks, achieving an order of magnitude reduction in computation time. In large-scale grid scenarios, the model can rapidly complete voltage optimization calculations, showing strong potential for research and engineering expansion.

It should be noted that although linearization significantly improves computational efficiency, when the system admittance matrix is extremely large or the network topology is highly complex, linearization errors may accumulate at certain nodes, potentially affecting the boundary solutions of the power flow. Therefore, future research should focus on

further refining the linearization approach to enhance the overall accuracy and applicability of the model while maintaining computational efficiency.

In summary, the proposed DLPF-MILP model performs excellently in accuracy, efficiency, and adaptability, providing a highly efficient, stable, and scalable solution for power flow calculation and voltage optimization in large-scale power systems. It holds important theoretical significance and engineering application value.

Bibliography

[1] U.S. Department of Energy. Blackout 2003: Blackout Final Implementation Report, 2025. URL https://www.energy.gov/search?keywords=Blackout+2003%3A+Blackout+Final+Implementation+Report&page=0.

[2] Central Electricity Regulatory Commission (CERC), India. Search – CERC, 2025. URL https://www.cercind.gov.in/search.html.

[3] A. Berizzi. The italian 2003 blackout. In *IEEE Power Engineering Society General Meeting, 2004.*, pages 1673–1679 Vol.2, 2004. doi: 10.1109/PES.2004.1373159.

[4] European Commission. Energy roadmap 2050. https://ec.europa.eu/energy/en/topics/energy-strategy-and-energy-union/2050-energy-strategy, 2011. Accessed: 2025-09-05.

[5] Florin Capitanescu. Evaluating reactive power reserves scarcity during the energy transition toward 100 *Electric Power Systems Research*, 190:106672, 2021. ISSN 0378-7796. doi: https://doi.org/10.1016/j.epsr.2020.106672. URL https://www.sciencedirect.com/science/article/pii/S0378779620304752.

[6] Peter D. Lund. *Advances in energy systems : the large-scale renewable energy integration challenge*. THEi Wiley ebooks. Wiley, Hoboken, New Jersey, first edition edition, 2019. ISBN 9781119508328.

[7] Stephen Frank, Ingrida Steponavice, and Steffen Rebennack. Optimal power flow: a bibliographic survey i: Formulations and deterministic methods. *Energy systems (Berlin. Periodical)*, 3(3):221–258, 2012. ISSN 1868-3967.

[8] Gerald B Shebl, Allen J Wood, Gerald B Sheblé, and Bruce F Wollenberg. *Power Generation, Operation, and Control*. John Wiley & Sons, Incorporated, United States, 2013. ISBN 9780471790556.

[9] M.S. Osman, M.A. Abo-Sinna, and A.A. Mousa. A solution to the optimal power flow using genetic algorithm. *Applied Mathematics and Computation*, 155(2):391–405,

2004. ISSN 0096-3003. doi: https://doi.org/10.1016/S0096-3003(03)00785-9. URL https://www.sciencedirect.com/science/article/pii/S0096300303007859.

[10] M.A. Abido. Optimal power flow using particle swarm optimization. *International Journal of Electrical Power & Energy Systems*, 24(7):563–571, 2002. ISSN 0142-0615. doi: https://doi.org/10.1016/S0142-0615(01)00067-9. URL https://www.sciencedirect.com/science/article/pii/S0142061501000679.

[11] Xiaoqing Bai, Hua Wei, Katsuki Fujisawa, and Yong Wang. Semidefinite programming for optimal power flow problems. *International Journal of Electrical Power & Energy Systems*, 30(6):383–392, 2008. ISSN 0142-0615. doi: https://doi.org/10.1016/j.ijepes.2007.12.003. URL https://www.sciencedirect.com/science/article/pii/S0142061507001378.

[12] Simón Sepúlveda-García, Oscar Danilo Montoya, and Alejandro Garcés. A second-order conic approximation to solving the optimal power flow problem in bipolar dc networks while considering a high penetration of distributed energy resources. *International Journal of Electrical Power & Energy Systems*, 155:109516, 2024. ISSN 0142-0615. doi: https://doi.org/10.1016/j.ijepes.2023.109516. URL https://www.sciencedirect.com/science/article/pii/S0142061523005732.

[13] Tillmann Mühlpfordt, Xinliang Dai, Alexander Engelmann, and Veit Hagenmeyer. Distributed power flow and distributed optimization—formulation, solution, and open source implementation. *Sustainable Energy, Grids and Networks*, 26:100471, 2021. ISSN 2352-4677. doi: https://doi.org/10.1016/j.segan.2021.100471. URL https://www.sciencedirect.com/science/article/pii/S2352467721000424.

[14] Amin Abedi, Ludovic Gaudard, and Franco Romerio. Power flow-based approaches to assess vulnerability, reliability, and contingency of the power systems: The benefits and limitations. *Reliability Engineering & System Safety*, 201:106961, 2020. ISSN 0951-8320. doi: https://doi.org/10.1016/j.ress.2020.106961. URL https://www.sciencedirect.com/science/article/pii/S0951832019304454.

[15] P. Kundur, J. Paserba, V. Ajjarapu, G. Andersson, A. Bose, C. Canizares, N. Hatziargyriou, D. Hill, A. Stankovic, C. Taylor, T. Van Cutsem, and V. Vittal. Definition and classification of power system stability ieee/cigre joint task force on stability terms and definitions. *IEEE Transactions on Power Systems*, 19(3):1387–1401, 2004. doi: 10.1109/TPWRS.2004.825981.

[16] J. Dixon, L. Moran, J. Rodriguez, and R. Domke. Reactive power compensation

technologies: State-of-the-art review. *Proceedings of the IEEE*, 93(12):2144–2164, 2005. doi: 10.1109/JPROC.2005.859937.

[17] Luca Buono, Daniele Difino, Francesco Palone, Simone Sacco, Roberto Spezie, Gabriele Tresso, and Andrea Valant. Tap staggering operation of autotransformers. In *2023 AEIT International Annual Conference (AEIT)*, pages 1–6, 2023. doi: 10.23919/AEIT60520.2023.10330319.

[18] Linwei Chen, Haiyu Li, Victoria Turnham, and Simon Brooke. Distribution network supports for reactive power management in transmission systems. In *IEEE PES Innovative Smart Grid Technologies, Europe*, pages 1–6, 2014. doi: 10.1109/ISGTEurope.2014.7028922.

[19] Hakan Kasap, Mikail Purlu, Belgin Emre Turkay, and Reza Ganjavi. Tap staggering analysis and effects on the adaptive protection system in networks with renewable energy sources. *IEEE Access*, 11:138623–138637, 2023. doi: 10.1109/ACCESS.2023.3339782.

[20] Hanmin Lim, Jongmin Jo, and Kwan-Ho Chun. Optimal on-load tap changer tap control method for voltage compliance rate improvement in distribution systems, based on field measurement data. *Energies*, 18(2), 2025. ISSN 1996-1073. doi: 10.3390/en18020439. URL `https://www.mdpi.com/1996-1073/18/2/439`.

[21] Samuel N. Okhuegbe, Adedasola A. Ademola, and Yilu Liu. Newton-raphson ac power flow convergence based on deep learning initialization and homotopy continuation. *IEEE Transactions on Industry Applications*, 61(2):2037–2046, 2025. doi: 10.1109/TIA.2024.3514992.

[22] Florian Dörfler and Francesco Bullo. Novel insights into lossless ac and dc power flow. In *2013 IEEE Power & Energy Society General Meeting*, pages 1–5, 2013. doi: 10.1109/PESMG.2013.6672260.

[23] Brian Stott, Jorge Jardim, and Ongun Alsac. Dc power flow revisited. *IEEE Transactions on Power Systems*, 24(3):1290–1300, 2009. doi: 10.1109/TPWRS.2009.2021235.

[24] K. Purchala, L. Meeus, D. Van Dommelen, and R. Belmans. Usefulness of dc power flow for active power flow analysis. In *IEEE Power Engineering Society General Meeting, 2005*, pages 454–459 Vol. 1, 2005. doi: 10.1109/PES.2005.1489581.

[25] Jingwei Yang, Ning Zhang, Chongqing Kang, and Qing Xia. A state-independent linear power flow model with accurate estimation of voltage magnitude. *IEEE Transactions on Power Systems*, 32(5):3607–3617, 2017. doi: 10.1109/TPWRS.2016.2638923.

[26] Seyed Masoud Fatemi, Sajjad Abedi, G. B. Gharehpetian, Seyed Hossein Hosseinian, and Mehrdad Abedi. Introducing a novel dc power flow method with reactive power considerations. *IEEE Transactions on Power Systems*, 30(6):3012–3023, 2015. doi: 10.1109/TPWRS.2014.2368572.

[27] John J. Grainger and William D. Stevenson. *Power System Analysis*. McGraw-Hill, 1994.

[28] Benalia M'hamdi, Madjid Teguar, and Benaissa Tahar. Optimal dg unit placement and sizing in radial distribution network for power loss minimization and voltage stability enhancement. *Periodica polytechnica. Electrical engineering and computer science*, 64(2):157–169, 2020. ISSN 2064-5260.

[29] M. Shukla and A. Sekar. Study of the effect of x/r ratio of lines on voltage stability. In *Proceedings of the 35th Southeastern Symposium on System Theory, 2003.*, pages 93–97, 2003. doi: 10.1109/SSST.2003.1194537.

[30] GAMS Development Corporation. `GAMS` – general algebraic modeling system, 2025. URL `https://www.gams.com/`.

[31] Ahmed Babiker, Sulaiman S. Ahmad, Ijaz Ahmed, Muhammad Khalid, Mohammad A. Abido, and Fahad Saleh Al-Ismail. Optimal power flow: A review of state-of-the-art techniques and future perspectives. *IEEE Access*, 13:60012–60039, 2025. doi: 10.1109/ACCESS.2025.3556168.

[32] Mohammad Asghari, Amir M Fathollahi-Fard, SMJ Mirzapour Al-E-Hashem, and Maxim A Dulebenets. Transformation and linearization techniques in optimization: A state-of-the-art survey. *Mathematics*, 10(2):283, 2022.

[33] Zhifang Yang, Haiwang Zhong, Qing Xia, Anjan Bose, and Chongqing Kang. Optimal power flow based on successive linear approximation of power flow equations. *IET Generation, Transmission & Distribution*, 10(14):3654–3662, 2016.

[34] Zhifang Yang, Haiwang Zhong, Anjan Bose, Tongxin Zheng, Qing Xia, and Chongqing Kang. A linearized opf model with reactive power and voltage magnitude: A pathway to improve the mw-only dc opf. *IEEE Transactions on Power Systems*, 33(2):1734–1745, 2018. doi: 10.1109/TPWRS.2017.2718551.

[35] R.B. Prada, B.H.T. Seelig, J.O.R. dos Santos, L.A.S. Pilotto, and A. Bianco. Modelling on-load tap changer voltage control and limits for network loading and voltage control effectiveness assessment. In *2003 IEEE Bologna Power Tech Conference Proceedings,*, volume 4, pages 6 pp. Vol.4–, 2003. doi: 10.1109/PTC.2003.1304797.

[36] Tao Ding, Rui Bo, Zhaohong Bie, and Xifan Wang. Optimal selection of phase shifting transformer adjustment in optimal power flow. *IEEE Transactions on Power Systems*, 32(3):2464–2465, 2017. doi: 10.1109/TPWRS.2016.2600098.

[37] Mohammad H Hajiesmaili, Desmond Cai, and Enrique Mallada. Understanding the inefficiency of security-constrained economic dispatch. In *2017 IEEE 56th Annual Conference on Decision and Control (CDC)*, pages 2035–2040. IEEE, 2017.

[38] Linwei Chen, Hai Yu Li, Steve Cox, and Kieran Bailey. Ancillary service for transmission systems by tap stagger operation in distribution networks. *IEEE Transactions on Power Delivery*, 31(4):1701–1709, 2016. doi: 10.1109/TPWRD.2015.2504599.

A | Appendix A

The IEEE 14-bus test system is adopted as the study case for tap staggering. The original system data are from Case 14bus. The modified data are provided in Tables A1–A3.

Bus Data Table

BUS_I	TYPE	PD	QD	GS	BS	VM	VA	VMAX	VMIN
1	3	0	0	0	0	1.06	0	1.06	0.94
2	2	10	6	0	0	1.045	-4.98	1.06	0.94
3	2	40	6	0	0	1.01	-12.72	1.06	0.94
4	1	20	6	0	0	1.019	-10.33	1.06	0.94
5	1	7.6	6	0	0	1.02	-8.78	1.06	0.94
6	1	11.2	0	0	0	1.07	-14.22	1.06	0.94
7	1	0	0	0	0	1.062	-13.37	1.06	0.94
8	1	0	0	0	0	1.09	-13.36	1.06	0.94
9	1	14.75	0	0	16	1.056	-14.94	1.06	0.94
10	1	4.5	0	0	16	1.051	-15.1	1.06	0.94
11	1	1.75	0	0	16	1.057	-14.79	1.06	0.94
12	1	3.05	0	0	16	1.055	-15.07	1.06	0.94
13	1	6.75	0	0	16	1.05	-15.16	1.06	0.94
14	1	7.45	0	0	16	1.036	-16.04	1.06	0.94

Table A.1: Bus data for power system analysis.

Generator Data Table

GEN_BUS	PG	QG	QMAX	QMIN	VG	MBASE	GEN_STATUS	PMAX	PMIN
1	40	-16.9	45	-45	0.94	100	1	332.4	0
2	50	42.4	30	-30	0.94	100	1	140	0
3	30	23.4	15	-15	0.94	100	1	100	0
6	0	0	24	-6	1.07	100	0	100	0
8	0	0	24	-6	1.09	100	0	100	0

Table A.2: Generator data for power system analysis.

Branch Data Table

F_BUS	T_BUS	BR_R	BR_X	BR_B	TAP	SHIFT	BR_STATUS	ANGMIN	ANGMAX
1	2	0.01938	0.05917	0.0528	0	0	1	-360	360
1	5	0.05403	0.22304	0.0492	0	0	1	-360	360
2	3	0.04699	0.19797	0.0438	0	0	1	-360	360
2	4	0.05811	0.17632	0.034	0	0	1	-360	360
2	5	0.05695	0.17388	0.0346	0	0	1	-360	360
3	4	0.06701	0.17103	0.0128	0	0	1	-360	360
4	5	0.01335	0.04211	0	0	0	1	-360	360
7	4	0	0.25	0	1	0	1	-360	360
7	4	0	0.25	0	1	0	1	-360	360
9	4	0	0.25	0	1	0	1	-360	360
9	4	0	0.25	0	1	0	1	-360	360
6	5	0	0.5	0	1	0	1	-360	360
6	5	0	0.5	0	1	0	1	-360	360
6	11	0.09498	0.1989	0	0	0	1	-360	360
6	12	0.12291	0.25581	0	0	0	1	-360	360
6	13	0.06615	0.13027	0	0	0	1	-360	360
7	8	0	0.17615	0	0	0	1	-360	360
7	9	0	0.11001	0	0	0	1	-360	360
9	10	0.03181	0.0845	0	0	0	1	-360	360
9	14	0.12711	0.27038	0	0	0	1	-360	360
10	11	0.08205	0.19207	0	0	0	1	-360	360
12	13	0.22092	0.19988	0	0	0	1	-360	360
13	14	0.17093	0.34802	0	0	0	1	-360	360

Table A.3: Branch data for power system analysis.

List of Figures

List of Tables

List of Symbols

Variable	Description	SI unit
$\boldsymbol{i}$	bus index	—
$\boldsymbol{P}_i$	active power injection at bus i	MW (or p.u.)
$\boldsymbol{Q}_i$	reactive power injection at bus i	MVAr (or p.u.)
$\boldsymbol{V}_i$	voltage magnitude at bus i	p.u.
$\boldsymbol{V}_j$	voltage magnitude at bus j	p.u.
$\boldsymbol{\theta}_{ij}$	voltage angle difference between buses i and j	degrees (or radians)
$\boldsymbol{G}_{ij}$	conductance (real part of admittance matrix)	p.u.
$\boldsymbol{B}_{ij}$	susceptance (imaginary part of admittance matrix)	p.u.
$\boldsymbol{y}_{ij}$	Admittance of the branch directly connecting bus i and bus j	p.u.
$\boldsymbol{y}_{ii}$	Shunt admittance at bus i	p.u.
$\boldsymbol{g}_{ij}$	Conductance of the branch between buses i and j	p.u.
$\boldsymbol{b}_{ij}$	Susceptance of the branch between buses i and j	p.u.
$\boldsymbol{G}'_{ij}$	Real part of the bus admittance matrix $\mathbf{Y}'_{\text{bus}}$ without shunt elements	p.u.
$\boldsymbol{B}'_{ij}$	Imaginary part of the bus admittance matrix $\mathbf{Y}'_{\text{bus}}$ without shunt elements	p.u.
$\boldsymbol{P}_{ij}$	Active power flow from bus i to bus j	p.u.
$\boldsymbol{Q}_{ij}$	Reactive power flow from bus i to bus j	p.u.
$\boldsymbol{P}^A_{ij}$	Linear approximation of active power flow between buses i and j	p.u.
$\boldsymbol{Q}^A_{ij}$	Linear approximation of reactive power flow between buses i and j	p.u.

Variable	Description	SI unit
$\boldsymbol{\theta}_{\mathcal{R}}$	Subvector of voltage angles at reference (slack) buses	degrees (or radians)
$\boldsymbol{\theta}_{\mathcal{S}}$	Subvector of voltage angles at PV buses	degrees (or radians)
$\boldsymbol{\theta}_{\mathcal{L}}$	Subvector of voltage angles at PQ buses	degrees (or radians)
$\boldsymbol{V}_{\mathcal{R}}$	Subvector of voltage magnitudes at reference (slack) buses	p.u.
$\boldsymbol{V}_{\mathcal{S}}$	Subvector of voltage magnitudes at PV buses	p.u.
$\boldsymbol{V}_{\mathcal{L}}$	Subvector of voltage magnitudes at PQ buses	p.u.
$\mathcal{B}$	Set of buses	—
$\mathcal{L}$	Set of branches (lines and transformers)	—
$\mathcal{G}$	Set of buses with conventional generation	—
$\mathcal{K}$	Set of all single-component outage scenarios	—
$\mathbf{V}_i^{\text{ref}}$	Reference or target voltage magnitude at bus i	p.u.
$\boldsymbol{S}_{ij,\max}$	Thermal rating (apparent power capacity) of branch (i, j)	MVA
$\boldsymbol{\alpha}_i$	Auxiliary variable for linearizing the absolute value function	—
$\boldsymbol{P}_{Tp}$	active power at port p	p.u.
$\boldsymbol{Q}_{Tp}$	reactive power at port p	p.u.
$\boldsymbol{P}_{Tq}$	active power at port q	p.u.
$\boldsymbol{Q}_{Tq}$	reactive power at port q	p.u.
$\boldsymbol{V}_{Tp}$	voltage magnitude at port p	p.u.
$\boldsymbol{V}_{Tq}$	voltage magnitude at port q	p.u.
$\boldsymbol{\delta}_{Tp}$	voltage phase angle at port p	degrees (or radians)
$\boldsymbol{\delta}_{Tq}$	voltage phase angle at port q	degrees (or radians)
$\boldsymbol{t}$	voltage tap ratio between the two ports	-
$\boldsymbol{\theta}_s$	transformer phase shift angle	degrees (or radians)
$\boldsymbol{Q}_{sh,i}$	shunt reactive power injection at bus i	var
$\boldsymbol{B}_i$	shunt susceptance of the reactive power compensation device at bus i	p.u.

Variable	Description	SI unit
$\boldsymbol{\mathcal{B}}_{sh}$	set of buses equipped with shunt compensation devices	—
$\boldsymbol{z_i}$	binary variable indicating whether a shunt device is ON/OFF	—
$\boldsymbol{w}_i$	auxiliary variable introduced to linearize the product $z_i V_i$	—
$\boldsymbol{T}_1, \boldsymbol{T}_2$	parallel transformers involved in the Tap Staggering operation	—
$\boldsymbol{t}_a, \boldsymbol{t}_b$	adjusted tap positions of $\boldsymbol{T}_1$ and $\boldsymbol{T}_2$, respectively	—
$\boldsymbol{t}_{a,0}, \boldsymbol{t}_{b,0}$	initial tap positions of $\boldsymbol{T}_1$ and $\boldsymbol{T}_2$	—
$\Delta\boldsymbol{t}_a, \Delta\boldsymbol{t}_b$	tap changes relative to the initial positions	—
$\boldsymbol{V}_i^k$	bus voltage magnitude at bus i under the k-th fault scenario	p.u.
$\boldsymbol{S}_{ij}^{A,k}$	branch power flow from bus i to j under the k-th fault scenario	MVA

Acknowledgements

First and foremost, I would like to sincerely thank everyone who has offered me unconditional love and support throughout my master's studies.
I am especially grateful to my family, whose understanding, patience, and encouragement have given me the courage to move forward fearlessly and the freedom to make my own choices.
I would like to express my heartfelt thanks to my supervisor, Professor Valentin Ilea, and my co-supervisor, Riccardo Nebuloni, for their invaluable academic guidance and patient mentorship.
I am also deeply thankful to my dear friends Naz and Lin. Without you, I cannot imagine what my life in Milan would have been like. Your companionship and support have made my time truly unforgettable.
Finally, thank you to everyone who has always loved and supported this ever-free and bright version of me.